Fakultät für Elektrotechnik und Informationstechnik
Technische Universität München

Motion-Blur in Scientific Images

Area-Based Registration of Blur, a Temporal Image Formation Model, and Computation of Readout Smear Corrections

Stefan R. Tabel

Vollständiger Abdruck der von der Fakultät für Elektrotechnik und Informationstechnik der Technischen Universität München zur Erlangung des akademischen Grades eines

Doktor-Ingenieurs (Dr.-Ing.)

genehmigten Dissertation.

Vorsitzender:
Prof. Dr.-Ing. Eckehard Steinbach

Prüfende der Dissertation:
1. apl. Prof. Dr.-Ing. Walter Stechele
2. Hon.-Prof. Dr. Dr. h.c. Sami K. Solanki

Die Dissertation wurde am 27.02.2019 bei der Technischen Universität München eingereicht und durch die Fakultät für Elektrotechnik und Informationstechnik am 17.06.2019 angenommen.

Für meine Eltern und meinen Sifu.

Danksagung

Diese Arbeit ist nur durch die Unterstützung zahlreicher Personen ermöglicht worden. Es ist mir ein persönliches Anliegen, die Wichtigsten zu nennen und ihre Beiträge zu würdigen.

Mein erster Dank gilt Prof. Stechele, der nicht nur als Erstprüfer sondern vor allem als Betreuer zu dieser Arbeit beigetragen hat. Ich möchte mich für das entgegengebrachte Vertrauen bedanken, das zur Aufnahme der Betreuung geführt hat. Vor allem aber bedanke ich mich für die stetige und exzellente Beratung, die ich über die Jahre erfahren habe, welche mir aber gleichzeitig allen Freiraum ließ, den ich für meine Forschung benötigte.

Weiter möchte ich mich bei Prof. Solanki für die Zweitkorrektur bedanken. Ich freue mich besonders über sein Interesse an meinen Forschungsergebnissen und die stetige Unterstützung die ich durch sein Team erfahren habe.

Grundlage dieser Arbeit war ein Vertrag am Halbleiterlabor der Max Planck Gesellschaft. Ich möchte mich bei Dr. Jelena Ninkovic für die Anstellung und den Vorschlag zur Doktorarbeit bedanken. Ich bedanke mich darüber hinaus insbesondere für die fachliche, kollegiale und finanzielle Unterstützung, welche ich über die Jahre erfahren habe, aber auch für den wissenschaftlichen Freiraum bei meiner Arbeit, der die Ergebnisse erst möglich gemacht hat.

Ebenso wichtig war die Hilfe von Prof. Bethke, ohne dessen Unterstützung diese Arbeit nicht zu Ende gekommen wäre. Ich bedanke mich dafür, dass er im entscheidenden Moment die Fortführung meiner Arbeit unterstützt hat und intern die Finanzierung des Versuchsaufbaus absicherte.

Mein Betreuer und Mentor Dr. Johannes Treis hat mich über mehrere Jahre intensiv unterstützt und mir in Kleinarbeit das Tagesgeschäft der Wissenschaft beigebracht. Wir haben wöchentlich jeden Fortschritt zusammengefasst und aufgearbeitet. Er ist die einzige Person, die nicht nur alle guten sondern auch alle schlechten Ideen kennt. Sein Interesse und Feedback stecken in jedem Gedanken dieser Arbeit. Durch seine Fragen habe ich am meisten gelernt, und seine Antworten haben jedes Problem gelöst. Für diese herausragende Arbeit möchte ich mich herzlich bedanken.

Einen sehr hohen Beitrag zu den Ergebnissen dieser Arbeit hat mein Student Korbinian Weikl geleistet. Er implementierte nicht nur den Hardware-Beschleuniger im Rahmen seiner Masterarbeit, sondern generierte darüber hinaus wissenschaftliche Ideen zu diesem Thema. Er hat alle Erwartungen an seine Masterarbeit übertroffen und wird mir vor allem als Co-Autor, Miterfinder und Preisträger in Erinnerung bleiben. Ich bedanke mich für die hervorragende Leistung.

Besonderer Dank gebührt auch zahlreichen externen Unterstützern vom Max-Planck Institut für Sonnensystemforschung, dem Kiepenheuer-Institut für Sonnenphysik und

der Firma Thorlabs. Ich bedanke mich bei Dr. Alex Feller für stetiges Feedback und Arbeitsmaterial zum Thema Sunrise, sowie bei Dr. Thomas Berkefeld für die Hilfe im Bereich adaptiver Optiken. Ich bedanke mich bei Dr. Tino Riethmüller für die Generierung der Testbilder zu den Simulationen, und bei Dr. Michiel van Noort für die Rekonstruktion der Punkt-Spreiz-Funktionen aus den wissenschaftlichen Bildern und die zugehörige Analyse der Bildfehler. Ein besonderer Beitrag zu dieser Arbeit kam von der Firma Thorlabs. Die herausragende Beratung und Hilfe des Support and Sales Team hat den Entwurf des optischen Versuchsaufbaus ermöglicht.

Zuletzt möchte ich mich bei meinen Kollegen am Halbleiterlabor für die gemeinsame Zeit und die vielfältige Unterstützung bedanken. Diese Arbeit wäre ohne Hilfe in Bereichen wie IT oder Mechanik undenkbar. Besonders hervorzuheben ist die kontinuierliche Beratung im Chip-Design durch Dr. Andreas Wassatsch sowie stetiges Feedback im Bereich der Physik durch Dr. Alexander Baehr und Dr. Florian Schopper.

Zusammenfassung

Wissenschaftliche Daten werden oft als Bilder mittels opto-elektronischer Systeme gewonnen. Ein Beispiel hierfür ist das Sonnenteleskop Sunrise, welches in der Gondel eines Stratosphärenballons betrieben wird. Die enorme Vergrößerung solcher Instrumente machte die Auswirkungen von Mikrovibrationen zu einem dominierenden Problem der letzten Dekade. Die Bewältigung dieses Problems wird in der Literatur als Messung und mechanische Unterdrückung der Vibrationen diskutiert. Wir arbeiten mit einem alternativen Ansatz, wonach die degradierenden Auswirkungen von Mikrovibrationen auf wissenschaftliche Bilder als zu lösendes Problem definiert werden. Die Auswirkungen der Mikrovibrationen auf eine Subapertur werden als Bewegungsunschärfe identifiziert, welche temporär variabel ist. Wir vergleichen diese Bewegungsunschärfe mit Degradierungen aus dem Bildgebungsmodell, welche räumlich variabel und temporär eingefroren sind. Normalerweise wird aber nur die eingefrorene Bewegungsunschärfe mittels Methoden der Wellenfrontkorrektur korrigiert. Degradierende Unschärfe in wissenschaftlichen Bildern können als Ergebnis von Wellenfrontstörungen verstanden werden. Die Messung solcher Wellenfrontstörungen und die erste Instanz ihrer Korrekturen erfolgen mit adaptiven Optiken. Als zweite Instanz der Korrekturen werden post-facto Methoden zusammengefasst, die sich auf verschiedene Entfaltungsverfahren zur Wiederherstellung des Objekts aus Bildern, welche durch adaptive Optik vorkorrigiert wurden, beziehen. Daher schlagen wir vor, das Standardverfahren für die Wellenfrontmessung auf zeitliche Variationen im Unschärfekern zu erweitern, um auf eine Korrektur der durch Mikrovibration induzierten Bilddegradierung hinzuarbeiten. Zu diesem Zweck verwenden wir das Bildgebungsmodell, welches ein Bild mit bestimmten Eigenschaften definiert, die für alle Methoden zur Messung und Korrektur grundlegend sind. Dieses Bild namens Subapertur wird durch eine geringfügige, räumlich variierende Unschärfe definiert, welche eine translatorische Verschiebung induziert, aber eine zeitliche Veränderung dieser Unschärfe wird nicht berücksichtigt. Wir argumentieren, dass Vibrationen diese Unschärfe-Degradierung in der Subapertur temporär verändern würden, und wir identifizieren Methoden aus anderen Disziplinen als grundlegend für eine Erweiterung dieses Bildgebungsmodells. Weiterhin zeigen wir, dass die Standard-Messtechniken, also Korrelationsverfahren, meist gut auf der zeitlich degradierten Subapertur arbeiten, und dass sie Bildverschiebungen berechnen, die durch die Schwerpunkte der zeitlich variierenden Unschärfe-Kerne der Bilder definiert sind. Das Bildgebungsmodell legt nahe, dass diese Ergebnisse als kontinuierlicher Schwerpunkt einer zweidimensionalen kontinuierlichen Spur angesehen werden können, die das relevante Signal für jede Korrektur der Degradierung ist. Daher schlagen wir eine Ausdehnung des Bildgebungsmodells auf die zeitliche Achse vor, indem wir zeigen, wie die Spur rekonstruiert werden kann, und wir vergleichen unsere Ergebnisse mit dem bisherigen Bildgebungsmodell in der räumlichen

Dimension. Die Theorie wird mit einem optischen Versuchsaufbau verifiziert. Es wird gezeigt, dass Zeitreihen, die mit Kameras zeitlich abgetastet werden, in ihren Amplituden unterschätzt sind und die Rekonstruktion mit einem Rechteck-Filter erfordern. Wir verwenden diese Erkenntnisse, um Simulationen über die Genauigkeit der adaptiven Optik des Sunrise-Teleskops unter Vibration durchzuführen und Details zur Modellierung der damit verbundenen Degradierung zu untersuchen. Wir fahren mit einer Sensitivitätsanalyse zur Registrierung zeitlich unscharfer Bilder in adaptiven Optiken fort, welche nützlich ist, um deren praktische Aspekte und Voraussetzungen zu verstehen. Als nächstes betrachten wir Fehler auf nicht-gemeinsamen optischen Pfaden, welche Korrekturen der adaptiven Optik unwirksam machen. Daher simulieren wir die Messung der durch Mikrovibrationen induzierten translatorischen Fehler mit einer Hoch-Kadenz-Kamera, die auch für die wissenschaftliche Bildgebung verwendet wird, so dass die Degradierung der wissenschaftlichen Bilder zu den Spuren passt, die für die Korrektur verwendet werden. Wir testen die Korrektur durch blinde Entfaltungsalgorithmen, die normalerweise in der Astronomie, aber auch im Bewegungs-Entfalten verwendet werden. Die Kenntnis der Punktspreizfunktion führt zu höherer Konvergenz und erhöhter Robustheit im Entfaltungsprozess. Die Messung der Punktspreizfunktion ist unabhängig von der Korrektur und hat keinen Einfluss auf die Instrumentierung oder die Datenreduktion in der Observation, aber die Registrierung von Bewegungsunschärfe mit einer Hoch-Kadenz-Kamera kann problematisch sein, wenn entweder Überfaltung auftritt oder andere Bewegungsunschärfe in den Bildern vorhanden ist. Wir führen beispielhaft eine Hoch-Kadenz-Kamera für das Sonnenpolarimeter Fast Solar Polarimeter ein, welche auf dem Sensor-Typ eines framestore Charged-Coupled-Device beruht, und somit vom sogenannten Smear-Effekt betroffen ist, wenn die Kamera ohne Verschluss betrieben wird. Die Degradierung aufgrund des Smear-Effekts wurde in der Vergangenheit teilweise als Rauschen betrachtet und wird in wissenschaftlichen Experimenten normalerweise post-facto korrigiert. In dieser Arbeit wird der Smear-Effekt als Kern von Bewegungsunschärfe identifiziert, welcher keine Grenzfrequenz hat. Wir verwenden Matrix-Beschreibungen vorheriger Smear-Modelle, um schnelle Berechnungen mittels direkter Filterung im Fourierraum herzuleiten, ebenso wie parallele und approximierte Berechnungen. Die Algorithmen ermöglichen die Implementierung eines Hardware-Beschleunigers für Echtzeit-Korrektur von Smear-Effekten, welcher angefordert ist, um Fast Solar Polarimeter in einer verwackelten Umgebung wie auf Sunrise zu betreiben. Insgesamt eröffnen wir eine neue Perspektive auf zeitlich variante Unschärfe im Bildgebungsmodel, unter Betrachtung von Mikrovibrationen und dem Smear-Effekt. Abschließend diskutieren wir alle Neuheiten sowie die Auswirkungen dieser Arbeit auf verschiedene wissenschaftliche Disziplinen und veröffentlichen Ideen für zukünftige Forschung.

Abstract

Scientific data is often acquired in form of images via electro-optical systems. One example is the Sunrise solar telescope, which is operated in the gondola of a stratospheric balloon. The enormous magnification of such instruments has made the impact of micro-vibrations a major challenge in the last decade. Common strategies for overcoming the impact of micro-vibrations as discussed in literature are measurement and mechanical mitigation. We work with an alternative ansatz, in which the degrading impact of the vibration on the scientific images is defined as the problem to solve. The impact of micro-vibrations on a subaperture is identified as motion-blur, which is temporally variant. We compare this motion-blur to blur degradation in the image formation model, which is spatially variant and temporally frozen. But only the frozen blur is normally measured and corrected via methods for wavefront correction. Blur degradation in scientific images can be understood as results of wavefront distortion. The measurement and a first instance of correction of wavefront distortion are done with adaptive optics. A second instance of correction is subsumed as post-facto correction, and refers to different deconvolution techniques for restoration of the object from images pre-corrected by adaptive optics. Hence, we explicitly propose to extend the standard method for wavefront measurement to temporal variations in the blur kernel, in order to work towards a correction of micro-vibration induced image degradation. For this purpose, we utilize the image formation model, which defines an image with certain properties that are fundamental for all methods for measurement and correction. This image, called subaperture, is defined by a slight space-variant blurring which induces a translational shift, but a temporal variation of this blurring is not respected. We argue that vibration would temporally change this blur degradation in the subaperture, and we identify methods from other disciplines as fundamental for an extension of this image formation model. Furthermore, we show that the standard measurement techniques, which are correlation methods, mostly work well on the temporally degraded subaperture, and that they calculate image defined by the centers of gravity of the temporally variant blur kernels of the images. The image formation model suggests that these results can be seen as centers of gravity of a two-dimensional continuous trace, which is the signal of interest for each correction of the degradation. Hence, we propose an extension of the image formation model to the temporal domain by showing how the trace can be reconstructed, and we compare our findings to the actual image formation model in the spatial domain. The theory is verified on an optical test-setup. It is shown that time series acquired via temporally sampling cameras are underestimated in their amplitudes, and require the reconstruction with a boxcar-filter. We use this insight to perform simulations on the accuracy of the adaptive optics operation of the Sunrise telescope under vibration, and go into details of the modeling of related degradation. We continue with

a sensitivity analysis on temporally blurred image registration in adaptive optics, which is helpful to understand its practical aspects and its prerequisites. Next, we regard non-common path errors, which make adaptive optics corrections non-effective. Hence, we simulate the measurement of the micro-vibration induced translational errors with a high-cadence camera that is also used for scientific imaging, such that the degradation on the scientific images match to the traces that are used for correction. We test the correction via blind-deconvolution algorithms, which are normally used in astronomy, but also in motion-deblurring. The knowledge of the point-spread function leads to higher convergence and increased robustness in the deconvolution process. The measurement of the point-spread function is independent of the correction and has no impact on the instrumentation or the data reduction in the observation, but the registration of translational motion-blur with a high-cadence camera can be problematic, if either aliasing occurs or other motion-blur kernels are present in the images. We exemplarily introduce the camera Fast Solar Polarimeter, which is of the sensor type of framestore Charged-Coupled-Devices, and hence suffers from readout smear in case the sensor is operated without shutter. The readout smear degradation was partially regarded as noise in the past, and is normally post-facto corrected in scientific experiments. In this thesis, readout smear is identified as motion-blur kernel without cut-off frequencies. We utilize matrix descriptions of previous readout smear models, in order to derive the fast computation via direct filtering in the Fourier domain, as well as parallel and approximate computation. These algorithms enable the implementation of a hardware accelerator for online smear corrections, which is required for operating Fast Solar Polarimeter in a jittered environment as on Sunrise. All in all, we offer a new perspective on temporally variant blur in the image formation model, under consideration of micro-vibrations and readout smear. Finally, we discuss all findings and the impact of this work on several scientific disciplines, and disclose ideas concerning future research.

Contents

List of Figures

List of Tables

Acronyms

10GE	10 Gigabit Ethernet.
ADF	Absolute Difference Function.
ADF2	Absolute Difference Function Squared.
AO	Adaptive Optics.
arcsec	arcsecond.
ASIC	Application Specific Integrated Circuit.
CCD	Charged-Coupled-Device.
CFF	Covariance Funtion in the Fourier-domain.
CFI	Covariance Function in the Image-domain.
CoG	Center of Gravity.
CWS	Correlating Wavefront Sensor.
DWFS	Deconvolution from Wave-Front Sensing.
FFT	Fast Fourier Transform.
FPGA	Field Programmable Gate Array.
FSP	Fast Solar Polarimeter.
GB	Giga-Byte.
GPU	Graphic Processing Unit.
Hz	Hertz.
IMaX	Imaging Magnetograph Experiment.
IP	Intellectual Property.
ISLiD	Image Stabilization and Light Distribution.
LISS	Lockheed Intermediate Sun Sensor.
MB	Mega-Byte.
MPS	Max-Planck institute for Solar system research.
MTF	Modulation-Transfer-Function.
NCPE	Non-Common Path Errors.

PFI	Postfocus Instrumentation Platform.
PSD	Power Spectral Density.
PSF	Point-Spread-Function.
QDR II+ SRAM	Quad Data Rate II+ Static Random Access Memory.
RMS	Root-Mean-Square.
SDF	Squared Difference Function.
SNR	Signal to Noise Ratio.
SUFI	Sunrise Filter Imager.

1 Introduction

Micro-vibrations have become a dominating problem in both, autonomous telescopes and ground based ones with very large apertures. The first case is valid for the Sunrise telescope, and we use this example to study the impact of vibrations on the quality of scientific images. We further investigate the utilization of a high-cadence cameras, and refer as a second example to the camera FSP. In this chapter, we introduce both projects and also guide the reader directly towards an understanding of the impact of vibrations on cameras using these examples. Both projects are described in a simplifying perspective, such that only the information required for the problem formulation and the later solution is introduced. Section 1.1 focuses on the Sunrise mission as a start and directly targets the reference of such literature, which is relevant for understanding the micro-vibrations on its flights. Such understanding is related to the task of the telescope which is imaging with cameras, and hence the effect of the vibrations on several cameras is highlighted. The first of two types of such effects is described as impact on high-cadence cameras, which are installed in the telescope for control applications. It is shown that such high-cadence cameras simply measure translational shifts on the cameras which result from the vibrations. The second type of these effects is described as image degradation, which is occurring on slower cameras that are used for acquisition of scientific data, on which vibration causes a smearing of the images. This smearing can be seen as problem, because it hinders the utilization of the data for scientific analysis. Section 1.2 formulates this problem in a way directly related to the later proposed solution. It is not promising to declare the occurrence of the vibrations as the problem to solve. Instead, we set the focus on the occurence of related image degradation at the science cameras, and we give a coarse draft of the proposed strategy for correction. We identify the methods measuring the vibrations via fast cameras, and utilize the knowledge of the degradation as problem solution. In this context, Section 1.3 introduces the camera FSP while focusing on its property to use image accumulation. We coarsely describe why FSP measures at high cadence, but outputs images at low cadence, and highlight a few selected properties of the data reduction pipeline of this camera. Next, the basic idea of this study is described in Section 1.4. The high-cadence imaging of FSP might be utilized to measure the micro-vibrations, in order to correct the accumulated scientific image with the results of these measurements. This idea is further developed to an overall structure of this study. We localize the interesting disciplines in the field of technical astronomy and image processing, which have to be investigated for understanding the state-of-the-art and embedding the succeeding contributions.

1.1 The Sunrise solar observatory and its residual jitter

The Sunrise solar observatory consists of a one meter diameter telescope for solar observations, which is operated in the gondola of a stratospheric balloon in 37 kilometers altitude. Figure 1.1 shows two press photos illustrating the start of Sunrise 2 in 2013, and the route of the first science flight from 2009. Related articles [1, 2] offer a first

(a) Start of Sunrise 2 [1]

(b) Route of Sunrise 1 [2]

Figure 1.1: Press photos of the Sunrise missions in 2009 and 2013.

insight into the Sunrise missions. It can be seen in Figure 1.1a that the balloon is not completely filled at start, but it reaches more than 120 meter diameter in the stratosphere. The balloon is connected to the gondola, which carries the telescope itself in its center. The telescope can be identified from its aperture in the hexagonal cage with an obscuration in the center. Solar panels around the aperture point on the sun simultaneously with the telescope and ensure the energy supply. The visible box on the bottom of the telescopes carries electronics. The route of the flight (Figure 1.1b) is chosen in a way that the telescope focuses continuously on the sun for approximately one week. This is possible during midnight sun beyond the solar turning circle. The start of the telescope in ESRANGE near Kiruna, Sweden, further allows using stratospheric winds for carrying the telescope via Greenland towards North America. The flight is autonomous, and the data is recorded and landed with the balloon. The observation from a stratospheric balloon makes sense, as the imaging process in a telescope is limited by two factors. The first of these factors is the diameter of the telescopes entrance, called aperture. It will be later explained that the incoming light is diffracted at this aperture, such that the achievable resolution in terms of measurable spatial frequency is limited by the diameter of the aperture. Secondly, the atmosphere of the earth also disturbs the imaging process of telescopes. This phenomenon will be referred to as wavefront degradation, which is in ground based telescopes mainly caused via refraction between different layers of the atmosphere. Hence, the flight of Sunrise in the outermost layer avoids this wavefront degradation similarly as satellites do, since such telescopes do not photograph through refracting layers of the atmosphere. Both phenomenons are used to describe the advantages of Sunrise. The balloon is able to carry heavy payloads, which are used for a bigger aperture than on satellites. This bigger aperture allows for resolving smaller scales than

with satellites at similar conditions without wavefront degradation. For these reasons, Sunrise offers the best achievable view on small-scale structures of the solar atmosphere, because it is the biggest solar telescope in terms of aperture diameter in space. The achievement of spatial resolutions below 100 kilometers with Sunrise is further critical for the discussion in solar astronomy, because the observations of structures of this size are expected to answer the most important questions. Such questions refer to the energy transportation between the corona, the outer layer of the suns atmosphere, and the visible surface of the sun, called photosphere. The temperature gradient between both is significant with millions of degrees, and not explainable with previously observable, bigger structures. But this is the mechanism which also affects earth's systems and thus is discussed in scientific literature.

The concept of Sunrise was introduced to the scientific discussion with [3]. The scientific goals are embedded in the related discussions, and the technical requirements are named. Interesting is the highlighting of several pros within the mission concepts. It is possible to observe the UV spectrum of the light, which is normally blocked by earth's atmosphere. Also the duration of continuous observable time-scales is given with at least several hours or up to even larger scales. Such measurements are required to be performed with high temporal, high spatial, and high spectral resolution, where polarimetric capabilities are explicitly intended. Requirements for such measurements are set in order to allow for detecting weak polarization signals, which refer to a low Signal to Noise Ratio (SNR) and high polarimetric accuracy. The latter demands either fast polarimetric modulation, or a setup with a dual beam in which a polarizing beamsplitter is used to feed two slower cameras. Both conceivable techniques would cover quasi-simultaneous measurements of all polarization states in less than 10 seconds. These requirements lead to instrument concepts which affect both, the main telescope and its peripheral instruments for coarse pointing and image stabilization, as well as three conceivable scientific instruments of the classes spectograph-polarimeter, filtergraph, and magnetograph.

A later publication presents the final Sunrise observatory as was flown in 2009 [4]. Other solar balloon missions are referred to, as well as related scientific discussions, and the overall mission concept is described with its impact on the instrument layout. Relevant in the following context are parts of the Postfocus Instrumentation Platform (PFI), which is a piggy-back carrier on the telescope containing the light-measuring instruments. These instruments are either scientific ones, i.e. the cameras Imaging Magnetograph Experiment (IMaX) and Sunrise Filter Imager (SUFI), or the opto-mechanical system Image Stabilization and Light Distribution (ISLiD) and the Correlating Wavefront Sensor (CWS), which calculates optical corrections from the incoming light via cameras. The reference finally describes the performance of these instruments during the flights. A post-flight analysis of the image data has shown that the design of the CWS and the instrument optics are not limiting the performance of the telescope. Also the ISLiD worked reliable. But two kinds of limitations have been reported. This is on the one hand a loss of stability in the pointing of the telescope, which was caused by wind gusts hiding the telescope. On the other hand, a residual image smear partially

reduced the spatial resolution of the scientific cameras SUFI and IMaX. The pointing of the gondola was measured by a sensor called Lockheed Intermediate Sun Sensor (LISS), which simultaneously recorded both types of image motion during the flight.

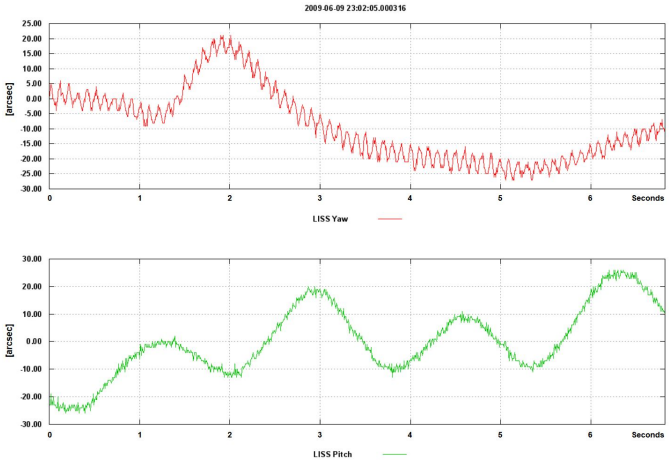

Figure 1.2: Representative image motion as measured with LISS during close-loop operation of the CWS [4].

Figure 1.2 from [4] shows the angular motion on two axes as recorded by the LISS, where the interesting part consists of the higher-frequent components. These higher-frequent components appear as 10 Hertz (Hz) signals in the Yaw-measurement, and are with more than 40 Hz also visible at Pitch. Both are assumed to be caused by bearing rumbles induced by electronic motors, where the assumption itself is described as speculative. A further suspect for contributing to the vibrations is named with shear-winds in the stratosphere.

Power Spectral Density (PSD) measurements of the vibrations have been taken with the CWS. These measurements are presented in [5], and are shown in Figure 1.3 on a logarithmic scale. A comparison with Figure 1.2 shows that the CWS has sampled

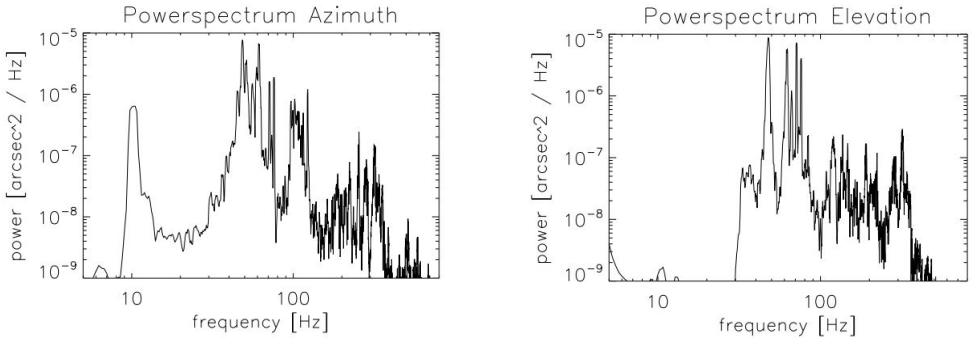

Figure 1.3: PSDs as measured with the CWS on Sunrise 2009 [5].

the jitter with similar peaks at 10 Hz and above 40 Hz. It also can be seen that the sampling frequency is much higher, and that coarse motions at single Hz rates from the LISS do not appear in the CWS measurements. The latter is due to the fact that the CWS is responsible for the fine alignment of the optical beam, and can be seen as second instance of correction.

LISS and CWS are sensors related to control operations, meaning their data is processed in order to set actuators. This is different at the scientific cameras IMaX and SUFI where the data is written back and used as input for scientific analysis, what further implies that the scientific data can be seen as net value of the overall mission. Its degradation is hence limiting the efficiency of the overall mission. The vibrations affect this data similarly as LISS and CWS, but they result in a smearing of the scientific data instead of a measurement of the jitter. The publication concerning SUFI [6] refers to the CWS [5] for a description of the jitter, but names reduced angular resolution as impact of the vibrations. The description of IMaX [7] goes one step further, and depicts the vibrations above 30 Hz as constant in time with an impact on image quality similar to an out-of-focus blur of one pixel Root-Mean-Square (RMS). The impact of this blurring was further investigated in [7] by applying shifts to consecutive photos of solar granulation, which resulted in a polarimetric sensitivity of one order of magnitude larger than required. This is a core statement for the problem formulation, since the occurrence of micro-vibration in scientific instruments hinders the use of its output data, which can be seen as net value of the mission. One further key statement can be found in [4], where it is stated that the impact of the vibration is different on both scientific cameras. More precisely, the angular resolution resulting from the vibrations is described as being different. This phenomenon is later introduced as Non-Common Path Errors (NCPE). The occurrence of NCPEs implies that measurements of the vibrations from one fast camera cannot be transferred to another camera, what is strongly determining the imaging strategy with a fast camera that uses image accumulation.

A focus on the vibrations is necessary for the problem formulation in this thesis, but it would be misleading to conclude from the occurrence of the jitter to the success of the flight. Instead, it was immediately clear that the mission brought the expected insight into named small scale structures, and had the foreseen impact on scientific discussions [8, 9]. Furthermore, the unreached imaging quality directly led to plans for the second flight, which was finally accomplished in 2013 in order to observe the sun during its active period [10]. The latter reference offers a final overview on the impact of Sunrise 2009 on the scientific discussion, and describes several changes in the hardware for the second flight. Interesting in the following context is that the problem with 10 Hz vibrations in the pointing was solved on Sunrise 2013, and that the measured, higher-frequent jitter at the CWS was reduced due to changes of the CWS itself. These changes will be partially discussed during this thesis, but it is necessary to introduce some fundamentals and to derive an understanding of the jitter. However, it can be seen that, at least, portions of the high-frequent vibrations of Sunrise 2009 are present on Sunrise 2013, which leads to a formulation of the problem in the next section.

1.2 Problem formulation and strategic approach

The last section offered a coarse overview on the Sunrise missions and highlighted the last remaining drawback, the occurrence of high-frequent micro-vibrations, as the problem to solve in an overall successful project. One could argue that a solution to the occurrence of the micro-vibrations would eliminate their impact on the scientific cameras, and thus enable perfect view during a third flight. Problematic in this regard is that the vibrations occur during a flight in the stratosphere. It would require at least one further start in order to measure the vibrations precisely enough to localize their sources. One would have to assume an immediate success of this venture, and further regard the occurrence of the vibrations as technical bug, so that the problem can be solved directly on ground without any testing. It was found during the studies related to this thesis that this option is not very promising due to several reasons. Firstly, it was attempted to measure the vibrations via accelerometers on the first flight, and this attempt was unsuccessful as the high-frequent ones contain less energy. Secondly, wind is named as one suspected contributor to the vibrations. It must be clear that its occurrence cannot be avoided, and that its contact surface will not be eliminated. Thirdly, Sunrise has accomplished two flights and a straight forward bug fix for the vibrations, which would allow for directly solving the problem in the next iteration, is not known. Finally, the angular resolution of the Sunrise telescope is extremely fine with fractions of an arcsecond (arcsec) per pixel on the camera. This magnification would resolve a paper sheet on 40 kilometers distance, what gives an idea of the scales of the vibrations. Hence, it is not very promising to declare the occurrence of the vibrations as the problem to solve.

The core statement for the problem formulation was cited already. The problem is that the data acquired with scientific instruments is affected by image degradation, such that it cannot be used for scientific analysis. This formulation satisfies the overall intend of the mission to acquire usable scientific data. Furthermore, it is based on a finding that was also described in the previous chapter: the vibrations have been measured already, in fact with the light measuring instruments on board. These are the scientific cameras, which have recorded vibrations in form of an image-degradation, and LISS and CWS which sampled the vibrations as time series. Finally and most importantly, this problem formulation is directly related to a strategic approach which is more promising.

The strategic approach for solving the problem depends on studying both the measurement of vibrations via imaging sensors and its degradation of scientific data in form of images. The difference between both cases also is hidden in the previous chapter. It is obvious that there is a dependence on the frequency of the cameras sampling, e.g. its framerate. This can be seen in Figures 1.2 and 1.3, where different bandwidths of the vibrations are sampled depending on different sampling-rates of the sensors. One further hint determining the strategy is found in the fact that LISS and CWS are astronomical instruments, which relates the discussion to be studied to the field of technical astronomy. Based on these ideas, a scientific camera is introduced in the next chapter, which

has a framerate of 400 images per second. This implies that the camera should be able to sample the vibrations in a certain band, similar to a sensor in control applications. Furthermore, the camera is designed for application in solar ground-based telescopes, such that it fulfills requirements for application in high-cadence spectro-polarimeters which were considered in the requirements on Sunrise [3].

1.3 The camera Fast Solar Polarimeter

The Semiconductor Laboratory of the Max Planck Society designs and manufactures imaging sensors for very advanced experiments in several fields of science. Such experiments can be found in high-energy physics, X-ray astronomy, or solar system research. One of our projects is the camera FSP, which is operated in the spectro-polarimeter with the same name. Both, the spectro-polarimeter and its camera are continuously developed and are categorized in different development phases. Furthermore, different test-setups have been implemented in several telescopes. Hence, it would be misleading to describe the overall development process. Instead, the complexity of this topic is reduced by referring with FSP to the current phase II implementation of the camera (Figure 1.4) from here on, while explicitly addressing a set of parameters and properties that are relevant in the later chapters.

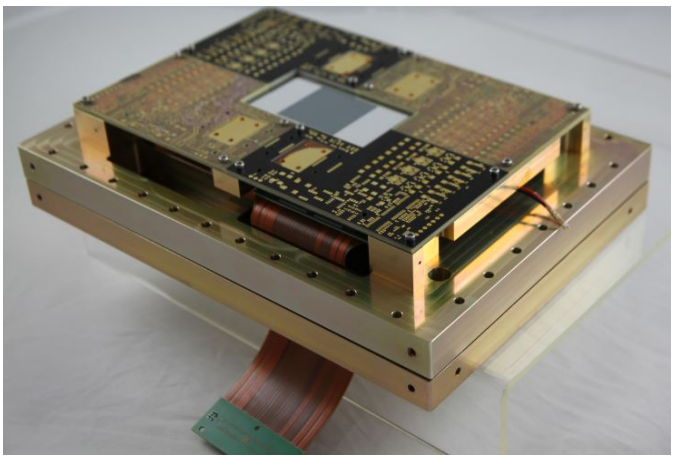

Figure 1.4: FSP phase II camera without housing.

The main aspect under which FSP is regarded in this study refers, next to the framerate, to its sensor type which is a so-called split framestore pn-Charged-Coupled-Device (CCD). This framestore CCD is operated without shutter in the spectro-polarimeter, such that a characteristic error called readout smear occurs in the images. As can be seen in Figure 1.4, the sensor consists of a squared region in its middle, which is the light-sensitive area that actually performs photography itself. The rest of the sensor is defined by two brighter regions on the borders of the chip, which are the name-giving

framestore arrays for readout. The image is split after exposure and each half of it is rapidly shifted into one of the framestore arrays afterwards. The sense of this operation is not of interest in this work, but the image degradation readout smear is caused by an ongoing illumination of the sensor during the procedure of shifting the image into framestore arrays. The correction of the resulting errors is known for several cases that will be introduced later, and was extended within the team around the spectro-polarimeter to polarimetric modulation [11]. The correction of this readout smear in polarimetric images is the topic around FSP in this studies, because there was a strict requirement to implement a certain case of this correction in a real-time processing machine, in order to make an application of the spectro-polarimeter acceptable for the owner of both projects.

Only one of the required properties of FSP does not depend on the camera, but on the spectrograph, which is said temporal modulation of polarimetric measurements. Temporal modulation is most simply explained on the website of FSP [12] as the principle of polarimetry. Polarization is described as a phase property of light, which cannot be measured directly. Hence, a so called modulator transforms the polarization information of the incoming light into intensity information, which can be measured with a synchronized camera. Since the polarization of light is described by sets of four different values, four different images have to be taken in order to characterize all polarization information in one scene. Furthermore, it is differentiated if two cameras are used in dual-beam setup, what implies that each of both cameras measures two polarization states in temporal multiplexing, or if a single camera is used in a single-beam setup to record all four measurements in temporal multiplexing. The relevant difference between both cases is the modulation frequency, which is the frequency with which a measurement of all four polarization states is performed. This frequency is twice as high for a dual-beam setup as for the single beam one. This thesis is partially based on the assumption of a single beam setup, implying that the camera is assumed to circularly capture four different scenes. For example, if the camera shoots a burst of photos in the spectro-polarimeter we would assume that the scene in image one is different to the scenes in images two, three, and four, but equal to the one in five and nine. Hence, we partially regard cameras that photograph on four interleaved channels.

Other relevant properties of FSP are normally derived from the requested polarimetric accuracy, as can be studied in case of FSP in [13, 14, 15, 16]. It is necessary to achieve a modulation frequency of at least 100 Hz in combination with very low readout noise, in order to satisfy requirements on the polarimetric accuracy, which allow for a further reduction of the data. The related study concerning FSP was done by Feller [17], where a 400 Hz framerate of FSPs phase II implementation in a single-beam setup was validated as the lower bound for the targeted polarimetric accuracy. However, the polarimetrical aspects are not covered in this thesis. We investigate the FSP camera under the aspect of motion-blur, and regard either the impact of micro-vibrations or readout-smear on the images. The property of FSP to photograph on interleaved channels will slightly affect our results, but is, unlike other points, not directly under investigation. Hence, FSP is regarded as a normal high-cadence camera with a variable scene condition, and

we explicitly do not cover case studies for polarimetric imaging with FSP on Sunrise. This is quite practical, because our results will show that FSP in its phase II implementation is not the solution for micro-vibrations on Sunrise. On the other hand, the final results will justify that vibration measurements should preferably be performed with a candidate for FSP phase III, which is not suffering from readout smear and allowing for higher framerates. Nevertheless, FSPs camera parameters are used if needed for simulation and will be introduced on-the-fly, although FSP and Sunrise are used as examples only and do not compromise the generality of the approach.

Finally, one property of FSPs data reduction is the utilization of image accumulation [11] in polarimetric measurements. All high-cadence images of the same channels are accumulated, in order to derive 4 single photos with higher SNR. This property would have to be ported with FSP to Sunrise for a simple reason: High-cadence imaging with 400 images per second would exceed the storage capacities on Sunrise [18].

1.4 Theses and structure of this work

The structure of this work is divided in two parts, which cover the measurement and the correction of micro-vibrations with methods from technical astronomy, and the optimized post-facto correction of readout smear. Both parts require a foregoing introduction of the state-of-the-art, which is given in each corresponding part itself and not in one dedicated chapter. The part concerning micro-vibrations is not only more extensive and contains more theses. It also is stronger related to the fundamental concepts of the image formation model and wavefront correction. Such concepts are further useful for understanding the second part, such that the overall structure of this thesis is simply explained. We introduce all relevant fundamentals in Chapter 2, and depict our theories related to micro-vibrations in Chapter 3. We present some intermediate simulations in Chapter 4, which are loosely related to Sunrise and FSP, but mainly used for the illustration of more practical aspects around the findings from the previous chapter. We switch to the second topic of readout smear in Chapter 5, where we focus on the computation of the correction and discuss its role as motion-blur afterwards. Finally, we offer in Chapter 6 a summary and a critical review of all statements, as well as a description of the expected impact on literature and an outlook on possible future research.

Chapter 2 introduces the required fundamentals in technical astronomy, and is partitioned in basics from the image formation model (Section 2.1) and wavefront correction (Section 2.2). The image formation model offers an abstract view on the electro-optical system, and explains how images are generated within these instruments. This results in the well-known standard formular in image processing, and introduces some prerequisites for the succeeding chapters. Furthermore, the wavefront is introduced in order to allow for an understanding of the following wavefront correction. Based on this, we coarsely explain the principle of Adaptive Optics (AO) operation and image deconvolution. These fundamentals in technical astronomy, however, are not only the fundamentals of this

work. Instead, they can be seen as the first thesis: We formulated the problem in a way that the impact of micro-vibrations on the image should be targeted, and not the mechanical occurrence of vibrations. Hence, we show why we focus on images with certain properties, and we state as a second thesis that the standard methods for wavefront measurement and correction should be utilized for correcting the images degraded by vibration. We use this chapter for decreasing complexity, as we argue that only this image with certain properties has to be investigated, and the basic methods that operate on it. We further highlight a restriction on this model, which is that the scene is assumed to be stable during exposure. And we state in a third thesis that this assumption is not necessarily true for micro-vibrations, such that the stable scene condition has to be relaxed. All in all, we demarcate our view on a single subaperture and special image registration methods. We expect that this is sufficient to handle micro-vibrations in electro-optical systems, because all introduced corrections rely on the knowledge of the error and operate on the single subaperture. Finally, we reformulate the described problem under knowledge of the subsumed fundamentals in Section 2.3.

Chapter 3 covers time series and their Modulation-Transfer-Function (MTF) in the image formation model, and contains the main theses of this work. We start with an introduction of the state-of-the-art in Section 3.1, where we state in the fourth thesis that the MTF resulting from vibration is nothing else than a motion-blur MTF. We criticize the handling of motion and vibration in the state-of-the-art via zero-phase kernels, highlight the temporal and arbitrary variance of both, and refer to better models in image processing. Our further focus is not on the description of the blurring, but the registration of motion-blurred images with area-based methods. Hence, we refer the state-of-the-art in area-based registration of blurred images, and identify one theory of choice for this purpose. We show that the image formation model is not respected in this theory of choice, and apply some intermediate critique in order to use the lesson learned for the introduction of more comprehensive theories. The first theory can be seen as thesis and a verified finding of this work, and is presented as area-based registration of arbitrary blur in Section 3.2. We show that area-based registration methods calculate shifts of images of the same object, which are defined by the Center of Gravity (CoG) of their blur kernels. Section 3.3 continues with the reconstruction of the motion trace, which has defined the blur kernels of the registered images in the image formation model. A boxcar-filter is identified as the relation between both, the motion trace and the CoGs of the blur kernels. The related reconstruction of the motion trace can be seen as further thesis and verified finding in this work. This is, because we verify both theories on a test setup in Section 3.4, and further show that the boxcar-filter is not only present when the position of the object is varied, but also when the intensity of the object varies. Hence, the theory on the reconstruction of time series is valid for at least two types of time series, which extends our last thesis. For this reason, we formulate our conjecture following in relation to the image formation model as a hypothesis in Section 3.5: The duty-cycle of a camera defines a sampling function, or an MTF, on all time series acquired with this camera.

Chapter 4 presents simulations related to the theories from the last chapter. We introduce some common fundamentals of all simulations in Section 4.1, which can be subsumed as image generation. We mainly highlight common problems related to this task, such that this section does not contain specific theses. Section 4.2 presents simulations on the accuracy of the Sunrise AO on the 2009 flight. A sensitivity analysis is used in order to illustrate boundary conditions for the registration of blur with heavily oversampling cameras, and we intermediately discuss some prerequisites on such registration. Section 4.3 investigates the registration of blur in case of high-cadence science cameras. We differentiate between Nyquist sampling and aliasing cameras, in order to illustrate the effect on the Point-Spread-Function (PSF) reconstruction. Similarly, we only show the resulting effect from utilizing the reconstructed PSFs as input in blind-deconvolution algorithms (Section 4.4), and conclude with an overview on our research related to micro-vibrations. Hence, we illustrate the practical application of our methods in operation points of the Sunrise telescope, while related theses have been presented explicitly in the previous chapter.

The second type of motion-blur in this work is handled in Chapter 5, where we investigate the computation of readout smear corrections. We start with a simple requirement that a hardware-accelerator is needed if FSP should become candidate for a third Sunrise flight. This requirement allows for an application of the standard design-flow, and hence we optimize the computation of post-facto readout smear corrections in Section 5.1. We describe four known algorithms in the state-of-the-art, and utilize them for the derivation of a fast convolution-based, parallel, and approximate version of the target algorithm. This derivation of optimized algorithms is mainly regarded as a verified finding and thesis of this work, and we claim a reduction of instruction and optimized parallelization while matching ground truth. The optimized algorithms are further used to implement the requested accelerator (Section 5.2), and we claim as final thesis that the requested hardware-accelerator can be implemented as described under the same functionality as ground truth. But we discuss in the end of this section that readout smear should be seen as motion-blur kernel, such that we think it is questionable if the input requirement for the hardware-accelerator is optimal.

In the end of this thesis, we discuss this work under several aspects in Chapter 6. We give a summarizing overview on all relevant statements (Section 6.1), while knowing that not all of these statements can be assumed to have impact on literature. For this reason, we critically review these statements in Section 6.2, in order to describe the main limitation of this work: It was not possible to apply our ideas to astronomical telescopes, AOs, or data reduction methods. Hence, this work contains some connecting theses that are not tested in real experiments, and thus remain unverified. In contrast, four thesis which we call hard findings are expected to resist a scientific discussion, and hence we derive a conceivable impact of these hard findings on related publications (Section 6.3). The first hard finding is the area-based registration of arbitrary blur, as presented in Section 3.2 and verified in Section 3.4, which has impact on the state-of-the-art concerning image registration and motion deblurring in the Sections 2.2 and 3.1. Secondly, the

verified sampling function on two types of time series (Section 3.4) has impact on fundamental textbooks from four related fields of science, which are wave-front correction, optics, Fourier optics, and MTFs as introduced in Chapter 2 and Chapter 3. Thirdly, some optimizations of readout smear algorithms in Section 5.1 are based on mathematical equivalence, such that they can be expected to resist discussions, and are hence claimed as hard findings. Finally, we state that a hardware-accelerator can be built with optimized amount of instructions compared to ground truth for an online correction of readout smear, as is shown in Section 5.2. This is the first architecture for post-facto readout smear correction, and therefore the impact consists of the initial description. However, not all thesis are verified in practical applications, such that we cannot derive impact from the connecting ones. For this reason, we use this bulk of theses for proposing possible future research in Section 6.4. Some ideas for their verification are presented, for example the application of our ideas to Sunrise, AOs, or high-cadence polarimetry, or the utilization of Deconvolution from Wave-Front Sensing (DWFS) against micro-vibrations.

Finally, we like to cite all publications which are related to this thesis. The hard findings on time series and the area-based registration of arbitrary blur (Chapter 3), as well as the application of both (Chapter 4) and all related theses, are published in [19]. A german patent is applied to the technical method for reconstruction of duty-cycle degraded time series acquired with cameras [20]. The optimization of algorithms for readout smear correction (Section 5.1) is published in the scientific literature in [21]. The related hardware-accelerator (Section 5.2) was presented on a scientific conference as well [22]. Both, the algorithms for readout smear corrections and the related hardware-accelerator (Chapter 5) are subjected to several patent applications [23, 24, 25].

2 Fundamentals in technical astronomy

One finding in the previous chapter is that AOs measure wavefront degradations when the optical path of the telescope is affected by micro-vibrations. The functionality of AOs, including the measurement of wavefront degradation, is discussed in the field of technical astronomy, although the main objective can be seen as the correction of wavefront degradation. Wavefront degradation is mostly caused by disturbing layers in the atmosphere of the earth, but vibrations may also degrade the wavefront of the incoming light in an optical instrument. The objective of correction has some critical implications, because a deeper understanding requires knowledge about the nature of light, its propagation in waves, and the final description of the optical systems. This knowledge contains a lot of basics and not all of them are relevant, because there are some abstraction layers in the so-called image formation model. Astronomical instruments are mainly camera based, such that the most important abstraction layer can be seen as the images of these cameras. Hence, we coarsely explain that the image formation model defines how images are generated in electro-optical instruments, and our main intend is to show why we focus on images with certain properties. The explanation is simply found in the telescope itself and is defined by its functionality. Hence, we present a simplified view which mainly allows for focusing on the detection of the wavefront degradation from these images, and vice versa for correcting these images from the degradation under knowledge of the degradation itself. In the following, we describe this in the reference to larger discussions, which are mostly referred to as textbooks in the next paragraphs. Thereby, we divide the structure in several sections. Section 2.1 illustrates some fundamentals of the image formation model. We introduce the wavefront and its degradation and describe a simplifying view on electro-optical instruments, which operate diffraction limited under utilization of detectors. This view results in the well known standard equation in image processing, such that we can simplify to an image processing task in which the resulting degradation might be recognized as blur. Section 2.2 leaves these fundamentals partially behind, in order to introduce some prerequisites on wavefront measurements and corrections. We mainly classify the problems and argue why we reduce this topic to image processing again. But we also identify some targeted algorithms, and introduce some concepts that cover relevant aspects from technical astronomy. In Section 2.3, we subsume the relevant properties of the investigated image and the methods which operate on it.

2.1 The image formation model

In image processing, a normal argumentation may start with the well known relation between image, object, blur and noise. This makes sense in case the abstract image

is considered, whose typical parameters may consist of color-information, several objects, or abstract information in the image. This is different in astronomy, where mostly gray-scale images containing a single object are acquired with high-end instruments that image through the atmosphere of the earth. There are at least two standard kernels describing the degradations resulting from instrument and atmosphere, such that wave-propagation, diffraction, and spatial sampling are normally concerned. Hence, we quickly refer to the fundamental steps in said image formation model, in order to argue for utilization of the standard image model in the following work.

The first basic concept introduced is the wavefront, as can be found in [26] and is illustrated in Figure 2.1. This figure shows a point source named PS radially emitting light, as is depicted with two reference rays. Each of these rays is a representation of the radial wave, which normally is described with a phase information ϕ. This phase information is constant on a spherical surface with constant radius in a certain point of time over all wave representing rays. Hence, a spherical segment of a light wave with constant phase information can be described as ideal wavefront.

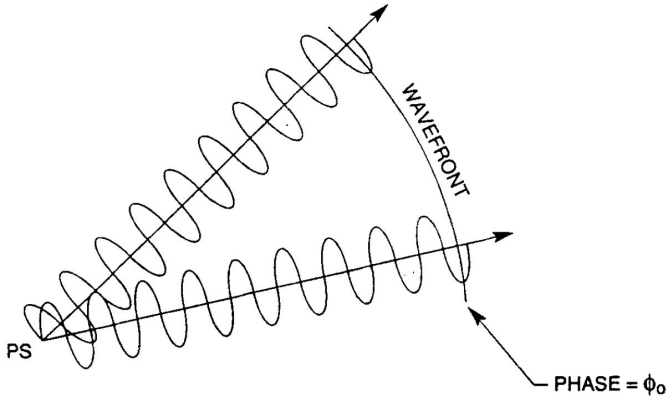

Figure 2.1: Ideal wavefront resulting from a point source [26].

Electromagnetic wave propagation can be seen as fundamental knowledge in electronic engineering, but this does not necessarily account for optics. We refer to the field of optics with the work of Hecht [27], and use this reference for the description of the planar wavefront as is shown in Figure 2.2. There, the point source is depicted as S, and also

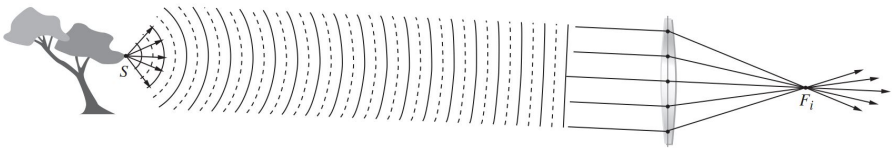

Figure 2.2: Planar wavefront resulting from a point source [27].

radially emitting light as in Figure 2.1. The spherical segment is drawn for very wide angles on the left, and rapidly decreasing ones to the right. The outer right wavefront

is drawn as planar, and the rays hiding the lens are ideally parallel. This is a standard assumption in optics, which is called the collimated beam. An infinite distant point source radially emitting light can illuminate an optical instrument with parallel rays, such that its aperture is hit by ideally planar wavefronts. This simplified model is a good approximation for telescopes, since the observed objects are very distant to the observer. The focusing of the lens on the other side is good model for an optical instrument as well. The light emitted from one point is focused in a particular focal point, such that an image can be photographed via a sensor.

An ideal optical black box is discussed in the field of Fourier optics [28], where it normally describes the relation between an object and an image. Both are related by an optical system, which is called the optical black box if its inner setup can be reduced to a transfer function. The optical black box from [28] is shown in Figure 2.3, and is further characterized with several properties. The black box connects arrays of point sources

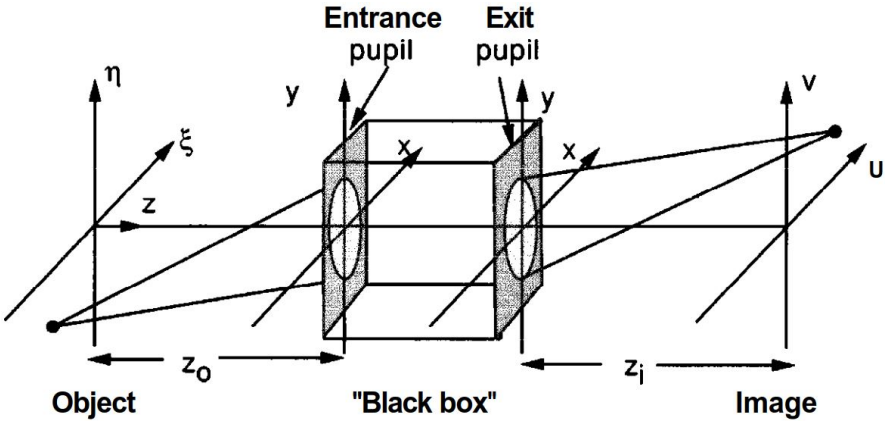

Figure 2.3: Optical black box [28].

in the object plane (η, ξ) to arrays of focusing points in the image plane (v, u), where focal lengths (z_o, z_i) typically specify the magnification. The optical black box further consists of the planes of entrance and exit pupil. It is stated that the mathematical description of object and image can be related via transfer functions, which characterize the diffraction at the pupil of the aperture.

Of special importance in this context is the diffraction pattern of a circular aperture, which is known as Airy disk. The Airy disk is derived in [28] as well. But we refer to [27] again, since preferable illustrations are given as is shown in Figure 2.4. This figure depicts the generation of the Airy disk via Fraunhofer diffraction on a circular aperture (Figure 2.4a), and the definition of the Rayleigh criterion (Figure 2.4b). Following [27], a diffraction pattern called Airy disk is generated in the image plane, when a circular aperture is hit by the ideally planar wavefront of a point source in the object plane. The circular aperture causes Fraunhofer diffraction, such that the function describing the intensity distribution of the pattern in the image plane can be seen as two-dimensional

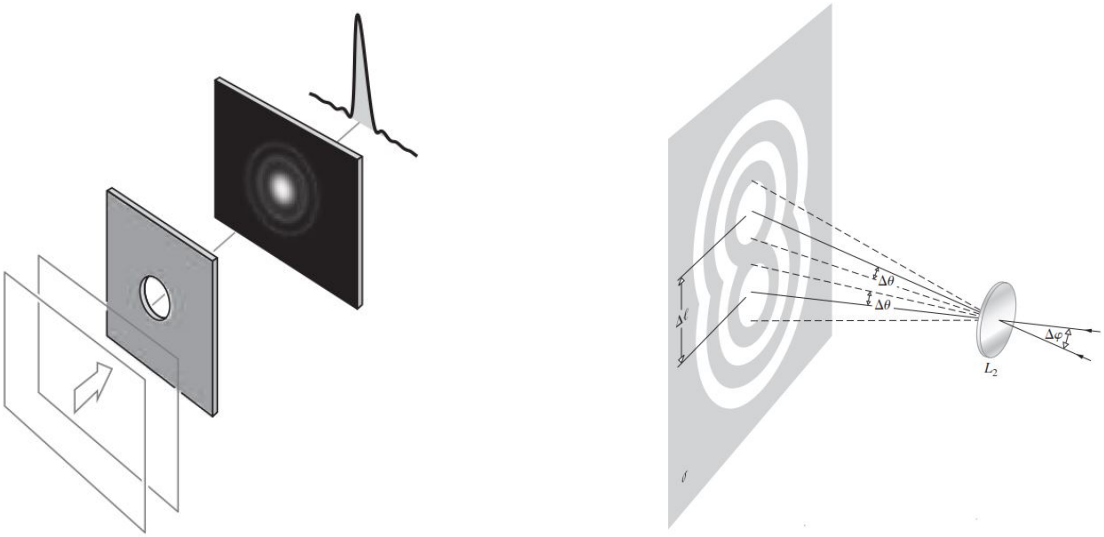

(a) Fraunhofer diffraction on a circular aperture results in Airy pattern.

(b) Rayleigh criterion.

Figure 2.4: Fraunhofer diffraction and Rayleigh criterion [27].

transfer function between the point source and the pattern itself. Hence, each point source in the object plane illuminates the image plane with the Airy pattern, such that image and object are related by the transfer function Airy disk. It can be seen that this pattern is rotationally symmetrical, such that its phase zero. A cut through its profile shows that the disk has several side lobes with related minimums. The first minimum from its center is used for the definition of the Rayleigh criterion, as is illustrated in Figure 2.4b. Two point sources are arranged on the object plane in front of a circular aperture, such that two Airy disks can be seen on the image plane. The Rayleigh criterion defines both Airy patterns as separable, if the maximum of one Airy disk is located at the position of the radially most inner minimum of the second Airy disk [27]. Hence, the distance between two Airy patterns is used to define a maximally resolvable spatial frequency of ideal optical systems with circular apertures. Smaller structures, or accordingly higher frequencies, are not resolvable with the optical instrument. In radial coordinates, the minimal resolvable angle of such instruments is given by the Rayleigh criterion. It depends on the apertures diameter D and the wavelength of the light λ, and is given in [27] in relation to Figure 2.4b:

$$(\Delta\phi)_{min} = \Delta\Phi = 1.22\lambda/D \tag{2.1}$$

The Airy disk often is referred to as MTF, where MTF names the absolute values of an optical transfer function. Both are defined in the Fourier space. In contrast, the PSF is defined in intensity space and its transform is the optical transfer function. The phase of the optical transfer function is called phase transfer function. But we use the term MTF to name PSFs, whose transforms have a phase equal to zero. However, MTFs in

the normal meaning and in its application to optical and electro-optical instruments are covered in [29]. We coarsely refer to this reference for a deeper understanding of MTFs, for example in terms of contrast damping, or the reconstruction of the true signals from their damped equivalents. In addition, we focus on one further transfer function, which is explained in [29] with the introduction of the electro-optical instrument. For this purpose, a rectangular detector array is installed in the image plane of the instrument as is shown in Figure 2.5.

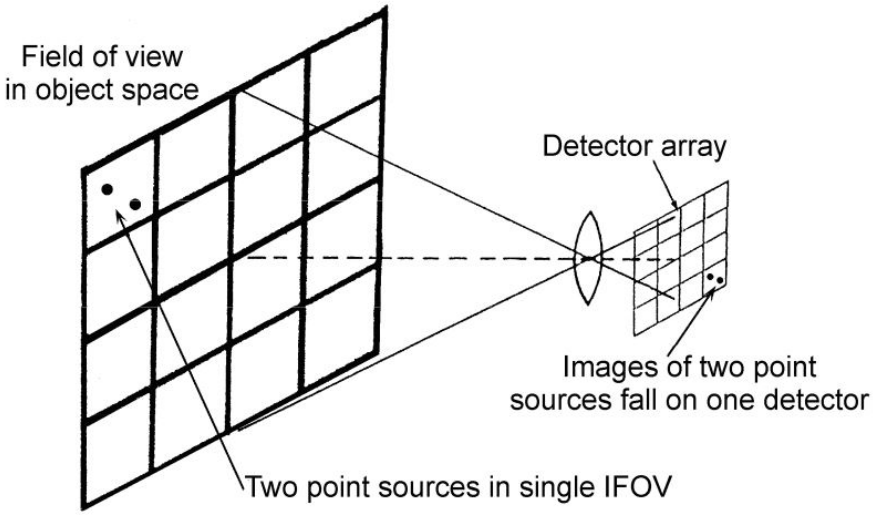

Figure 2.5: Detector array in the image plane [29].

Figure 2.5 from [29] shows a detector array installed in the image plane of an ideal optical instrument. The projection of this array onto the object plane consists of several instantaneous fields of view (IFOV in the figure). It can be seen that two point sources fall into one instance of these. The point sources are not separable in terms of detector-wise sampling of the sensor, since each detector integrates the intensity-generated charge within the two-dimensional borders of that detector. Normally, the size of the detector is adjusted in a way that the Rayleigh criterion defines the spatial sampling of it, since the sampled signal also is band-limited by the aperture of the optical instruments. An electro-optical instrument is called sampling critically, if the cut-off frequencies defined by both the detector and the Rayleigh criterion match.

This section has coarsely guided the reader through what is called image formation in electro-optical instruments. This process is very fundamental on the one hand, as it relates the object o to the image i via the PSF p (which can be an MTF if its phase is zero). The relation to the ubiquitous standard equation in image processing becomes obvious, at least when the noise n is further respected:

$$i = o * p + n \tag{2.2}$$

On the other hand, the referred books show that this model can easily cover hundreds of

pages, but still stating nothing more than fundamentals. But these fundamentals serve as a suitable introduction in several ways. Firstly, the non-specialist reader might be able to find the connection to image processing, which is normally based on the image model in equation (2.2). Secondly, the following introduction of the AOs requires some coarse understanding of fundamentals like the wavefront. Finally and most importantly, one main result of this thesis is that this image formation model might be extended to temporally variant processes, in which the sensor shoots consecutive photos of a variable object. This idea is closely related to the detector footprint MTF, which is further described in [29]. The spatial extend of the detectors results in an MTF, which is invertible and correctable under the assumption of a Nyquist-correctly sampled, band-limited signal. We utilize the same description in the one-dimensional case in order to describe a similar effect of the exposure time on time series measured from several images. However, we only like to state that the fundamentals and the contribution of this thesis will split at this point, but we intermediately return to [29] for a description of the state-of-the-art on vibrations in image formation.

2.2 Fundamentals in wavefront correction

Incoming wavefronts normally pass the atmosphere of the earth before they hit the aperture of a ground-based telescope. The atmosphere consists of several turbulent layers which refract the passing light, such that the ideally planar wavefront becomes distorted. This means that the phase of the wavefront is randomly delayed over its spatial extent, and the wavefront itself is no longer planar. The measurement of these distortions can be found in AOs, as well as the correction via deformable mirrors.

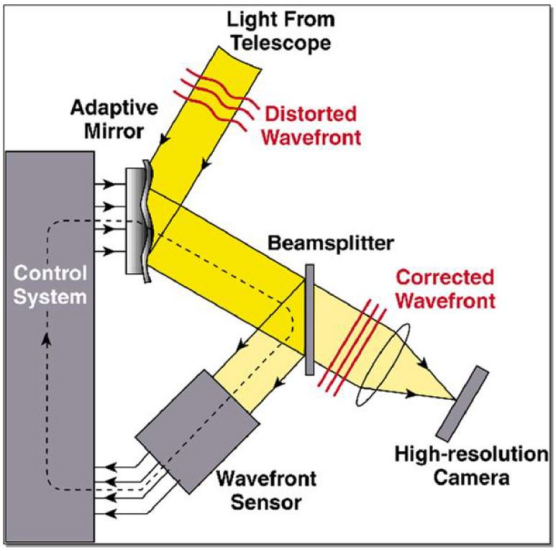

Figure 2.6: Working principle of ground based AOs [30].

Figure 2.6 from [30] illustrates the working principle of ground based AOs. We coarsely follow the argumentation given by this reference. It can be seen that the incoming wavefronts are distorted. This is caused by the atmosphere of the earth, where different temperatures define several refractive layers that randomly delay the phase in each area of the wavefront. It is shown that the distortion is not homogeneous in space, and the gradient of the wavefronts is different on different positions of the continuous wavefront. These distorted wavefronts are reflected by a deformable mirror, which has adopted a form that corrects the surface of the wavefront to a planar one again. This corrected wavefront is focused on the image plane of the high-resolution camera, which captures the scientific net-data. The same wavefront is reflected via an optical beamsplitter towards the wavefront sensor. This sensor is connected via a control loop to the deformable mirror. Like every control loop, those in AOs also require low latencies and depend on residual errors. This implies that the correction never is perfect, but only the remaining error of the correction is dynamically minimized. The sensing of the wavefront differs between night-time astronomy, where point like stars are normally available for the estimation of the PSF, and day-time astronomy, where the investigated sun appears as extended object. Hence, we explicitly introduce some concepts of day-time, or extended scene, technical astronomy. The most actual and compact reference in this field is given with [30]. It covers not only the relevant articles, but also refers the interested reader to previous and more detailed textbooks in the same field. Hence, we recommend it for deeper investigations.

It is further argued in [30] that the standard wavefront sensor is of Shack-Hartmann type. The feedforward part of control loop operation of this type of wavefront sensors is implemented in what is called CWS, and is illustrated in Figure 2.7. The overall

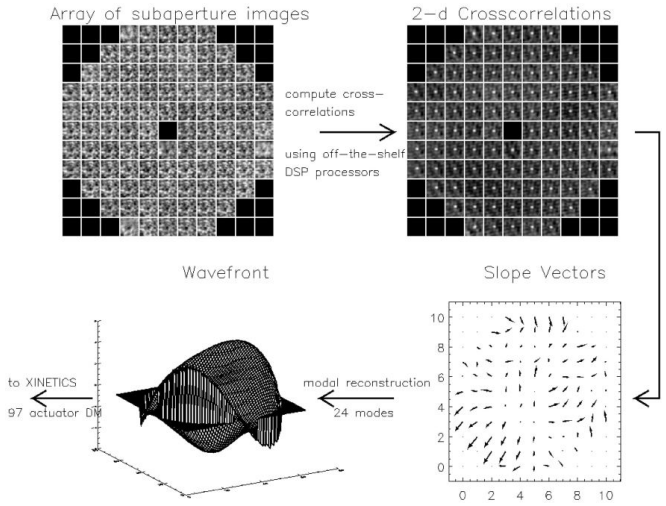

Figure 2.7: Forward control loop in extended scene AOs [30].

field-of-view, i.e. the aperture of the optical instrument, is divided into an array of subapertures. Each subaperture corresponds to a so called coherence length, which means

that the inhomogeneity of the gradient of the wavefront of this part of the field of view does not exceed a certain maximum, i.e. there only is a defined and limited incoherence in each subaperture. Further important is that all subapertures show the same image content. This is accomplished with a dedicated optical setup in front of the camera of the wavefront sensor. This optical setup allows for correlating each subaperture to a single one chosen to be the reference. A correlation algorithm determines the translational shifts of the subapertures against each other's. The slope of these vectors as a function of time is used for recovering the relative, local wavefront gradients, which again are used for computing the wavefront and setting the mirror. Each subaperture contains slight incoherence but a relatively homogeneous average shift, and an aperture may consist of several subapertures whose shifts are individually corrected for. We only have to regard a single subaperture, and may describe incoherence with several parallel electro-optical systems, i.e. subapertures. It can be further denoted that the mathematical method operating on these subapertures is correlation.

We further focus on reference [30] in order to show that there is spatial and temporal dependence on statistics of the atmosphere during the layout of AOs. So called Kolmogorow statistics are used in order to define the Fried-parameter, which gives the diameter of the subaperture in which a certain deviation of the wavefront gradient is not exceeded. Hence, the Fried-parameter determines the amount of subapertures in a particular aperture under constant atmospheric conditions. Furthermore, there is a dependency of the framerate in the AOs control loop on Kolmogorow statistics via the Greenwood frequency. Finally, there is a resulting condition being known as hypothesis of frozen flow, which can be assumed to be valid in ground-based telescopes [31]. This hypothesis indicates that the phase distortion of the wavefront, called phase-screen, is temporally constant during each exposure, but moves with a certain wind-speed over the telescope. Hence, one can say that atmospherical statistics are layouting parameters for AOs, as they set requirements on subaperture-sizes, framerates, and temporal variations of the blur kernels. In this context, we emphasize our thesis that these atmospherical statistics are not necessarily valid for micro-vibrations. For example, we cannot imagine that the phase screen of an arbitrary vibration necessarily freezes during exposure and moves with a constant wind-speed. Hence, we try to relax the requirements on these layouting parameters in AOs in the further context of this work, as we try to register images with temporally arbitrary blur.

Here, it must be stated that is not intended to give a complete introduction into wavefront sensing, which would exceed the scope of this thesis by far. It is intended to guide the reader towards the location in the telescope where the error resulting from the micro-vibrations is measured. We found this location in the CWS of the AO, where subapertures define images that are correlated in order to determine the relative shift between each other. It is not necessary to understand how the subapertures are generated in the optical beam, or how the correction is exactly performed. Instead, we like to highlight that the measurement is performed on series of spatially band-limited images of certain size and framerate, which are correlated to arbitrary reference images. The

wavefront degradation, and the resulting blur in the subapertures, are more or less coherent. This implies that the related average phase error can be calculated and corrected based on the results of these correlations. The results of these correlations are relative, which means they are not related to an absolute origin, but to a reference image. Our initial motivation was to understand the methods which have either measured the vibrations, or are commonly used for correcting the scientific images. The measurement methods are identified as image registration methods from the CWS and introduced next. Meanwhile, the regarded abstraction layer of the image also was derived, as well as the correction via deformable mirrors in AOs.

The methods for correlating images in extended scene AOs are given in [32] and shown in Table 2.1. These methods are the Absolute Difference Function (ADF), the Abso-

Table 2.1: Registration algorithms from extended scene AOs [32]

acronym	correlation surface
ADF	$c_{j,k} = \sum_{x,y} \left\lvert a(x,y) - r(x+j,y+k) \right\rvert$
ADF2	$c_{j,k} = \left(\sum_{x,y} \left\lvert a(x,y) - r(x+j,y+k) \right\rvert \right)^2$
SDF	$c_{j,k} = \sum_{x,y} \big(a(x,y) - r(x+j,y+k) \big)^2$
CFI	$c_{j,k} = -\sum_{x,y} \bar{a}(x,y) \circ \bar{r}(x+j,y+k)$
CFF	$c_{j,k} = -\mathcal{F}^{-1}\Big(\mathcal{F}'\big(h \circ \bar{a}(x,y)\big) \circ \mathcal{F}\big(h \circ \bar{r}(x,y)\big) \Big)(j,k)$

lute Difference Function Squared (ADF2), the Squared Difference Function (SDF), the Covariance Function in the Image-domain (CFI), and the Covariance Funtion in the Fourier-domain (CFF). All methods operate on two images, where r is the reference image that is typically constant for image series of a certain duration, and a is the actual image from the series whose shift is determined in relation to the reference. Both images are assumed to show a constant scene, and having different translational offsets which are described with a vector in coordinates of the images. All methods output the correlation surface c with the variables (j,k). The minimum of c gives the integer shift between both images a and r via its coordinates (j,k). The bar operator $(\bar{a},\bar{r})$ identifies images from which a bi-linear least-squares-fit is subtracted, h is the hamming window, $\circ$ the element-wise multiplication, $'$ the complex conjugate, $\mathcal{F}$ the Fourier transform, and $\mathcal{F}^{-1}$ its inverse. It can be found that several classes can be built from these methods. Methods using the element-wise multiplication are referred to as covariance-based methods in [32], where all others are difference-based. Furthermore, only the CFF method is Fourier-based, implying that the computation is faster than those of all other space-based methods. Space-based methods shift the reference-image, which is smaller than the actual image, over the actual image, where the indices (j,k) define even this shift.

The half of the difference-size of the images a and r is often called search area, and defines the maximally detectable shift for difference-based methods. The CFF method receives images of the same size as input and its search area is half the image size, but it operates on the assumption of repetitive signal content such that the hamming window is needed to overcome limitations due to edge effects.

In addition to that, the subpixel-interpolation of registration results is needed, where different methods are evaluated not only in [32], but also in [33]. We follow the latter reference. The minimum (j_0, k_0) of c gives the images shift-distance with integer accuracy only, but the curve of c can be interpolated based on the adjacent pixel positions. $c(j_0 - 1, k_0)$ and $c(j_0 + 1, k_0)$ are needed in order to refine the separable result along the j-dimension for example. However, variations of these interpolations have been neglected in this thesis, and we only work with the parabola fit as defined with equation (2.3) from [33]:

$$j_{refined} = j_0 + \frac{c(j_0 - 1, k_0) - c(j_0 + 1, k_0)}{2[c(j_0 - 1, k_0) + c(j_0 + 1, k_0) - 2c(j_0, k_0)]} \tag{2.3}$$

The same subpixel refinement is possible on the separable k-axis, which is quite uninteresting to show again. Instead, we continue illustrating the subpixel error-curves resulting from inaccuracies of the interpolation. We show results from [33] in Figure 2.8. Figure 2.8a illustrates the well-known error-curves in subpixel image registration in case

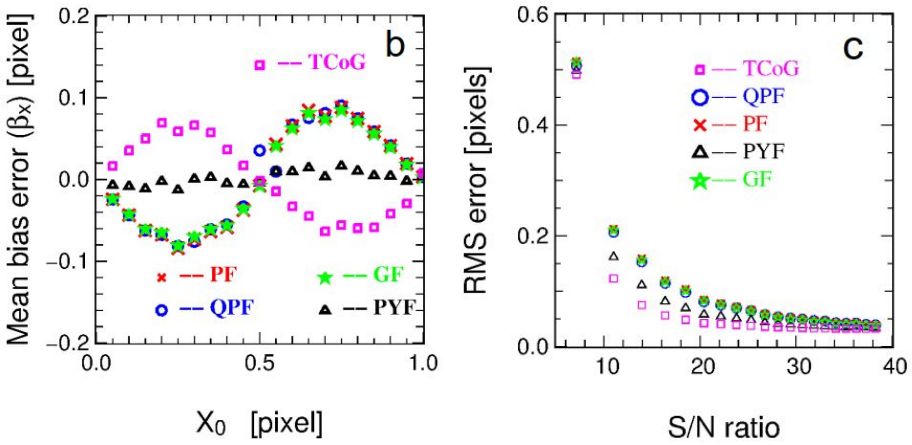

(a) Supixel error-curves **(b)** Convergenz for high SNRs

Figure 2.8: Bias and random errors in subpixel image registration [33].

of different subpixel interpolators, where PF stands for the parabola fit in the figure. The horizontal axis shows the fractional part of the shifts between both images r and a, and the vertical one shows the resulting error, which is called bias since it only depends on the calculation method and the calculated fractional shift. Figure 2.8b shows the RMS error in pixel depending on the SNR of the images. It is interesting to find that there is a convergence at high errors of these methods for very low SNRs. The later

context of this thesis is about such cases, where a random component of the error is dominating the measurements. Hence, subpixel error-curves are not clearly visible and adaptation to different interpolation methods doesn't change the results significantly. This seems to be valid in extended scene AOs as well. For example, the Sunrise AO was layouted with Michau's estimator, which does not concern the interpolation method but the SNR instead [5]. But the error-curves are later important, because we argue with their occurrence in similar measurements.

Indeed, the quite simple method of image correlation covers the measurement of wavefront degradation in most extended scene telescopes. Its application in AOs also has introduced the first of two standard methods of wavefront correction, in which deformable mirrors in the AOs correct for main parts of the wavefront degradation in real-time. This correction is explained in detail in [30], but we like to refer to [30] again because the AO correction is described as imperfect and several of its errors are distinguished. For example, the spatial averaging over wavefronts in subapertures causes spatial errors, or temporal variations during the control loop cycle of the AO similarly cause temporal errors. Furthermore, it was already stated that there has to be a residual error since the AO consists of an electronic controller. Such errors have to be corrected for in a second instance, if the scientific images are used in a further data processing.

The common second instance for correction of these finer errors is called post-facto processing, and [30] differentiates between short exposure imaging and long exposure imaging. Short exposure imaging requires several images of the same object for the reconstruction of this object, i.e. the long exposure image is divided into a burst of high-cadence images. Long exposure imaging utilizes image deconvolution algorithms for object reconstruction, which requires that the PSF is well known [30]. This point is critical for understanding our thesis that DWFS should be used against vibrations, because it formulates a hard requirement on the imaging on Sunrise. The topic of post-facto reconstruction would exceed the scope of this work by far again. Hence, we simplify by applying the requirement of image accumulation and coarsely discuss three cases. Firstly, we cannot assume to have capacity for storing several images per photographed object, and therefore short exposure imaging cannot be applied. We like to emphasize that this case is simply not investigated, and we think it would be promising to study this case if sufficient memory is available. Secondly, we found that pure AO correction is by definition insufficient, since the correction is imperfect. It was also found during the Sunrise flights themselves that AO correction does not solve the micro-vibration problem. Hence, only the third possibility within wavefront correction is investigated, which is the long exposure case. This long exposure case mainly is in [30] referred to with [34], where the work-flow is illustrated with Figure 2.9.

Figure 2.9 from [34] illustrates the calculation of the long-exposure PSF from three inputs, which are residual errors in the AO, the actuator commands to the deformable mirrors, and the transfer-function of the telescope. We only like to show that there is a known flow to determine the PSF of the resulting long-exposure image, and we refer

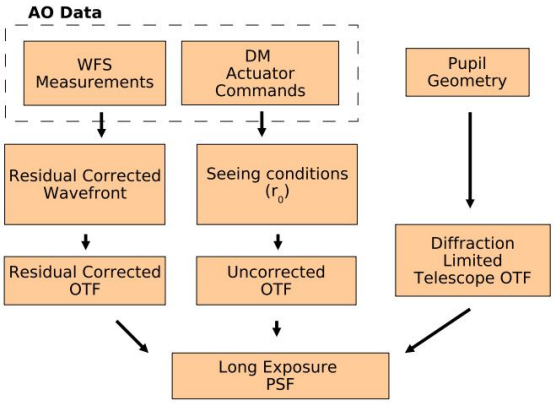

Figure 2.9: PSF reconstruction from AO telemetry data [34].

to [10] for an understanding of other PSF measurements on Sunrise. A phase-diversity setup was used in order to measure the transfer function of the telescope as a PSF. The calculated PSF was used in a modified Wiener filter for recovering the objects from the images. An introduction into phase-diversity and the modified Wiener filtering methods is given with [35]. However, we have to state again that we do not go into the topic of deconvolution. We only intend to state that there are methods to deconvolve the image sufficiently if all PSFs are known, and it obvious in the previous context that they fail if the additional PSF from the jitter is present. Hence, we argue that the jitter should be measured and further expressed as PSF, so that post-facto reconstruction methods might be expected to work on images degraded by micro-vibrations. We think that the standard methods from technical astronomy seem to be the most suitable methods for application, since they can be assumed to be the most validated and most acceptable ones in the wider range of all conceivable methods. This is also the basic idea of this work, just to measure the resulting PSF of micro-vibrations, in order to input it into deconvolution algorithms, which are known to recover the object once the overall PSF is known. We will refer to this idea as DWFS, which is the name of this method in night-time astronomy [36]. In this context, we cite a very good overview of DWFS, where the normal measurement process and the utilization of the Wiener filter are shown [37]. Furthermore, the advantages of this method are explicitly named, which are increased robustness and a higher rate of convergence in the deconvolution process. We denote that the fundamental requirement for this method is the synchronization of all cameras, such that measurements from the AO temporally match the degradation at the scientific cameras. Finally, we like to cite [38], because we want to highlight the relation of the PSFs in the short exposure case to the one in the long exposure case. The PSF in the long exposure case is the normalized sum of all PSFs in the short exposure case.

The bigger the diameter of a telescope becomes the higher is the achievable angular resolution of the telescope due to the Rayleigh criterion, but a higher resolution also implies a higher magnification of micro-vibrations with the scene. Hence, micro-

vibrations have become the dominating problem in telescopes with very large apertures. An overview on micro-vibrations in larger telescopes can be found in [39]. Following this reference, it can be seen that vibrations commonly occur in telescopes, and that their sources are diverse and not easy to determine. Common strategies for the handling of vibrations rely on their measurement and mitigation. Such measurements are partially performed with dedicated AOs, and partially with special accelerometers. The mitigation is the preferred solution for the occurrence of vibrations, which is often incomplete since certain sources like wind cannot be overcome. However, three things are interesting in the further context. Firstly, there is no analysis on the measurement accuracy of micro-vibrations in AOs. We think it would be interesting to evaluate if AOs, which are layouted based on Kolmogorow statistics, measure vibrations correctly. Secondly, certain filters are implemented in the control loops of AOs in order to overcome so called NCPEs. Finally, the standard methods of post-facto image processing and the correction with AOs are not utilized to solve the impact of vibrations on images. The first and the latter point are directly related to the focus of this work. Hence, we evaluate the measurement accuracy later on the example of Sunrise and work on wavefront based correction approaches. Besides this, it is necessary to introduce NCPEs.

NCPEs are explained in [30] as fundamental error-type of AOs, but we illustrate the underlying principle with a sketch in Figure 2.10. In the figure, the incoming light

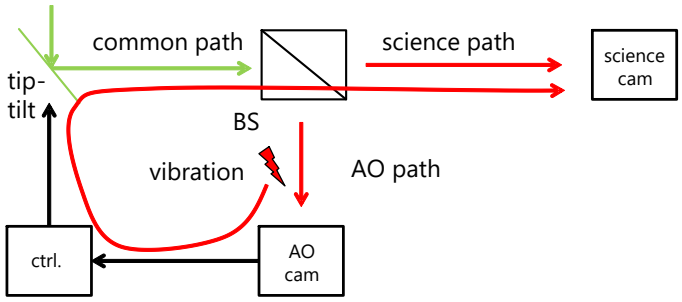

Figure 2.10: Illustration of common and non-common paths. Forwarding of vibration from the non-common path at the AO to the science camera.

is reflected by a tip-tilt mirror. A tip-tilt mirror is a steerable one like a deformable mirror, but it is solid and tipping and tilting is possible for correction of translational image motions. The reflected light is split by a beamsplitter, called BS in this figure, to both the scientific camera and the AO one. This splitting separates two optical paths from the incoming beam. The latter is the common-path and shown in green on the left of the beamsplitter. If vibrations occur on this path, they are assumed to affect both cameras equally. Two paths are marked in red in order to highlight that they are non-common, which means that an optical degradation occurring on these paths is not affecting all cameras. This implies two things. NCPEs between beamsplitter and sci-

ence camera cannot be measured and corrected via AOs. Even more critical are NCPEs on the second path between beamsplitter and AO. Such errors, named vibration in the figure, are certainly not degrading the scientific image. But they are detected by the AO, and forwarded due to correction by the tip-tilt mirror to the common path, such that they also appear at the science camera. This forwarding problem with NCPE is partially solved with filters in the control loop of AOs. The related vibration can be filtered if its frequency is known and constant, in order to avoid its forwarding. A good example for such a strategy can be found in [40]. It might be interesting to find that certain descriptors of the jitter match to the Sunrise mission. But we like to emphasize that the occurrence of NCPEs hinders the application of standard DWFS to Sunrise and most ground-based telescopes, because degradation on the science images and AO measurements do not necessarily match. This explains our focus on the FSP camera, which might be able to sample the vibrations without NCPEs. In addition, this reference illustrates that the mitigation of micro-vibrations is a time-consuming and iterative process, and thus not very suitable for application on autonomous missions.

2.3 Problem formulation and image model

All previously introduced fundamentals on the Sunrise mission and technical astronomy allow for a refined problem formulation. A residual tip-tilt error was measured in the control loop of the AO of Sunrise. The source of the vibrations is unknown, and the vibrations affect the instruments as NCPEs. Internal investigations [18] at the Max-Planck institute for Solar system research (MPS) have confirmed that PSFs from different cameras do not match, such that the assumption of NCPEs is valid. Furthermore, the errors at the science cameras consist of translational motions only, such that the whole aperture can be modeled with a single subaperture. Contributions like rotations of images or incoherence have been excluded. Hence, it should be investigated if the impact of vibrations could be corrected with the utilization of a high-cadence imager like FSP in order to overcome NCPEs. In the meantime, it has been shown that the measurement of translational image motion is possible on short exposure images. We identified the measurement techniques as image correlation methods for extended scenes, as well as the standard correction procedures, which are AO based ones and post-facto methods. Hence, the strategy is to measure the impact of translational vibrations on short exposure images, and to utilize these results for calculating the resulting PSF of the accumulated long exposed image. In addition, we found a need for evaluating the performance of vibration detection via correlation. Unfortunately, we have limited capacities for investigation of the standard correction methods. Hence, this thesis goes deeply into the measurement of vibrations on subapertures, such that we set a special focus on the fundamental image model. We found that the wavefront gradient is measured via correlation on images that are translated. These images are affected by at least the telescopes MTF. Ground-based telescopes would additionally suffer from residual incoherence, which is known to be averaged out in the correlation process [32]. It is

not present on Sunrise as a space-based mission, such that we investigate registration of temporally blurred images which are degraded with an Airy disk in addition. Instead of spatial incoherence, we focus on the temporal variation of blur, because we cannot assume that vibrations follow statistics of the atmosphere. This model, consisting of single subaperture, can be easily extended to several ones, because incoherence is modeled with several channels of such translated images, which is valid not only in AO control but also in image post-facto processing. The concept of an electro-optical system only consisting of a single subaperture, closely related to this image model, can be found in correlation trackers which are predecessors of AOs. We give an example with [41], where a feasibility study on the first correlation tracker is performed. Hence, the AO model used in this thesis is defined by a tip-tilt system as is drawn in Figure 2.10. All in all, we work on a standard image model with a telescope MTF and a PSF resulting from mechanical vibrations. Noise is handled as zero-mean Gaussian noise and not really in the focus of this work. We assume a single subaperture, which is not limited in size, since the Fried parameter is infinite on Sunrise. Residual incoherence is neglected, because it is not present on Sunrise, and further known to average out in standard correlation methods. We expect that all results based on this model can be transferred to cases that cover incoherence via utilization of several subapertures. Finally, we think that all methods for wavefront correction will profit from the knowledge of the degradation.

3 Time series and their MTF in the image formation model

The last chapter has introduced some fundamentals on both the image formation model and technical astronomy. We have shown why we focus on the subaperture with certain properties, and we argued for a measurement of vibrations as translational image motion on exactly this subaperture. This motion shall be expressed as additional PSF, which might be used as input for the deconvolution of images in the long exposure case. The standard methods of area-based image registration in extended scene telescopes are cited. These methods are applied in most solar telescopes, and they successfully measure the wavefront gradients which are resulting from atmospheric turbulence. But it cannot be assumed that this is an adequate technique to measure image shifts induced by vibration, because vibrations do not necessarily follow Kolmogorow statistics. The methods for the description of the impact of vibrations on images are excluded from the previously introduced fundamentals, and separately discussed as state-of-the-art in Section 3.1 of this chapter. We start with quotation of methods for the handling of motion and vibration in the image formation model, and we criticize these models under several aspects. Hence, we focus on other discussions that are found in image processing and offer more comprehensive motion-blur models. Next, we show that blur is commonly neglected in image registration, or mostly seen as degradation if it is taken into account. We highlight one exception where the role of blur is interpreted differently, in the sense that blurring is causing the shift of the image instead of hindering its detection. We then use this assumption for porting registration algorithms from extended scene AOs to the registration of arbitrary blur (Section 3.2). In this adaption, the registration algorithms calculate the CoG distance between blur kernels. The view of the image formation model suggests that registration results can be seen as CoG of the signal of interest. Hence, we utilize the well-known boxcar-filter in Section 3.3 for calculating back to even this signal from its known CoGs. As these findings are some of the main theses of this work, we offer a hardware verification on an optical test-setup that implements a correlation tracker (Section 3.4). It is shown that the boxcar-filter is not only present on registration results from image sequences, but also has to be considered when temporal variations of intensities are investigated. Hence, we introduce the more abstract concept of time series, which are degraded by the exposure time of the imaging camera. In Section 3.5, we argue that this filter can be seen as a temporal version of the same filter, which is known from the spatial image formation model. We offer a short comparison and extend the previous model. All in all, this chapter embeds the main findings of this thesis, the area-based registration of blur and the reconstruction of time series acquired with cameras, in the scientific context of both the state-of-the-art and more comprehensive

theories.

3.1 State-of-the-art

The focus in the previous chapter was on the image formation model, in which the discrete image is related to the object via transfer functions. Reference [29] only describes the impact of MTFs in this relation, which are understood in this work as PSFs with phase information that is equal to zero. We previously followed the argumentation of this reference up to the introduction of the electro-optical system, and return to its succeeding description of motion- and vibration-MTFs.

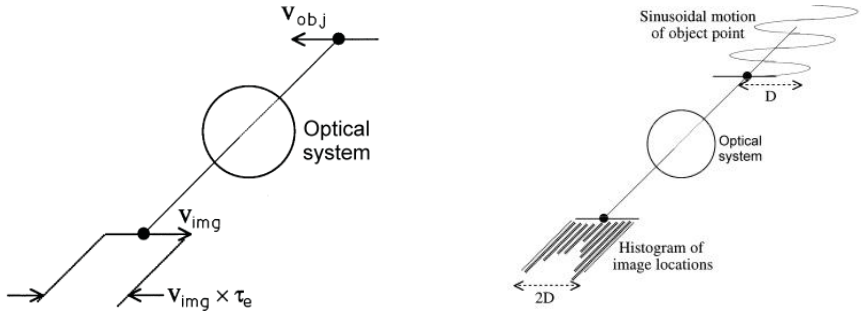

(a) Motion-MTF **(b)** Vibration-MTF

Figure 3.1: Motion- and vibration-MTF [29].

Figure 3.1 shows how motion (Figure 3.1a) and vibration (Figure 3.1b) are handled in [29]. It can be seen that both cases model the optical black box between object plane and image plane, where the object is an ideal point source. Figure 3.1a shows an object lineary moving with a velocity v_{obj}. Hence, its projection on the image plane during exposure time τ_0 describes a line of the length $v_{img} \times \tau_0$. The velocities are thereby different due to the magnification of the black box. The resulting MTF is represented by the projected line. If the line is discretely sampled to the sensor grid, similarly as the discrete image, the resulting MTF would fulfill the standard equation in processing, i.e. it would relate image and object as a transfer function. Interesting is how the description as MTF is enforced. The motion of the object is assumed to fulfill symmetry to a vertical axis of the coordinate system of the optical black box, and hence to the sensor centered in the optical beam. A spatial signal with this symmetry has zero-phase information, which is clear if one recalls that a signal can be written as Fourier series. The harmonics in this series are cosines, which are symmetrical to said axis when their phase is zero. Hence, the description as MTF is enforced by requiring symmetry to the ordinate. Vibrations are handled very similar in [29], as can be seen in Figure 3.1b. The ideal point source is vibrating on a single frequency, such that the projection of this

point describes a line in a single dimension of the sensor. The probability of the point source to stay in one instantaneous field of view, i.e. in the projection of a detector onto the object plane, is sketched in the histogram on the pixel grid of the sensor. Hence, the resulting MTF is represented by this histogram. One can find that the same conditions as before are used to enforce a zero phase for a description as MTF. We like to criticize several aspects in this approach. Firstly, we cannot find why the motion of the point source is synchronized to the sensor, such that the phase information of the motion is suppressed. Secondly, we think it is an avoidable constraint to handle one-dimensional motions only. Thirdly, we think it should be possible to extend this model to vibration compositions that consist of more than a single frequency. Finally, and this is a thesis in this work, there is obviously no difference in both the descriptions of motion and vibration. This means, the effect of translational vibrations is modeled in the same way as the effect of translational motion. A temporally variant, ideal point source is drawing its trace in both cases on the sensor grid, such that its interpolated projection describes the MTF. Furthermore, one can imagine that each motion consists of a frequency composition, and therefore a differentiation seems questionable. From this we conclude that one could extend this MTF model to a two-dimensional one, which, in addition, handles phase information and several frequencies. It is only necessary to remove the symmetry and velocity constraints for the motion, and to allow for two-dimensional sensor grids. Such a more complex model for the description of motion-blur is given in [42]. We like to refer the interested reader to this reference for deeper investigations of this topic, especially since this description also is based on the image formation model. In the following, we regard two-dimensional, arbitrary motion-blur PSFs in order to explain the impact of translational vibrations on electro-optical systems. But we like to focus on the application of image registration to motion-blurred images, and not the understanding of the blur itself.

Our focus is on the registration of images with methods from technical extended scene astronomy, where the images are degraded by arbitrary translational motion-blur. This is due to the facts that there are strict requirements on the PSF measurement for the long exposure photography, and that we found standard methods for the measurement of blur information. The state-of-the-art concerning image registration and blur in images is quite overwhelming, and it is not constructive to summarize the discussions. On the other hand, our verified findings allow to derive impact on three ones, which are image registration, blur-invariances, and hybrid imaging from motion deblurring. Hence, we intermediately introduce the discussions on image registration and blur-invariances, before we continue with the relevant information from hybrid imaging.

Due to possible impact on literature, a point of interest concerns an overview of a huge amount of conceivable methods for image registration, and we give a reference on [43] for an adequate survey on this topic. In this reference, correlation methods are classified as area-based methods, because image areas are matched in order to determine the shift between images. These area-based methods are further distinguished from feature-based methods, which operate on features in the images, for example edges or

points. Feature-based methods are not relevant in solar astronomy, because the solar surface does mostly not contain features. Area-based methods are further categorized in correlation-like methods and Fourier-based ones. It can be noticed that these area-based methods from image processing are different to the ones used in astronomy. It is further notable that the registration of blurred images is rarely handled, with an exception in a discussion that covers blur-invariant feature descriptors. These are methods which define features in images that can be registered when images are blurred. Such feature-based methods are not relevant for the achievement of our goals, but it becomes clear that blur is seen as a degradation which hinders the registration of images, and that it is intended to register the images despite the presence of blur. This is in contradiction to our theses.

More precisley, reference [44] is highly relevant, because the paradigm of blur-invariant feature descriptors spilled over to area-based methods with this reference. We show the test results from [44] in Figure 3.2, in which the phase-correlation PC and the blur-invariant phase correlation BIPC are tested. The actual image is shifted and in addition

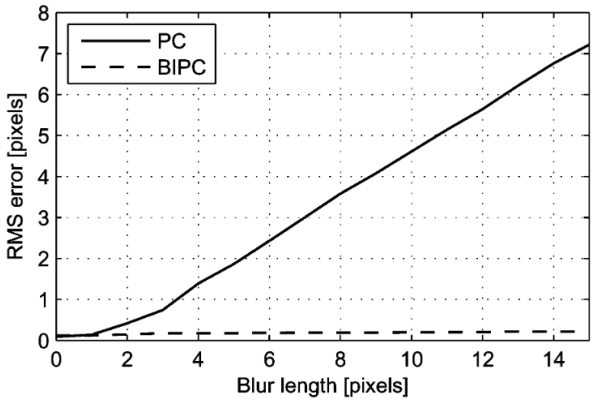

Figure 3.2: Test results of the blur-invariant phase correlation [44].

blurred as if by linear motion. The BIPC method calculates the shift correctly, such that there is no influence of the blur kernel on the registration results, but the PC method suffers from a linear trend in dependence of the spatial extent of the linear motion-blur kernel. We cannot interpret these results, because there is no public available source code that shows how the blur is applied. But it should be emphasized that [44] is one of the most relevant contributions for area-based registration of blurred images, which is obviously limited by symmetry constraints on the blur kernel, and tries to register a shift despite the presence of blur. We criticize both the symmetry constraints on the blur, as well as the missing definition of shift and blur, and do not follow up on related approaches. But we think it is interesting to see that invariances to blurring are possible, because this will raise the question what is registered and what not, e.g. there is no definition of the shift in the reference.

Blur is rarely discussed in relation to area-based image registration. Instead, the core statement on the registration of blurred images was found in the relation to the motion-deblurring problem. This problem refers to the reconstruction of the object from a motion-blurred image via deconvolution. A good overview of these discussions can be obtained from [45]. A more detailed analysis of [45] shows that the configuration of a telescope, consisting of fast and slow cameras, naturally supports hybrid imaging for motion-deblurring. This technique has indeed the same concept as DWFS in technical astronomy, with the interesting difference that motion-blur is explicitly targeted. The content of the related chapter in [45] was originally published by the same authors in [46]. This work was quickly accepted and republished in a journal [47]. We like to name the coarse steps in which the contribution normally is partitioned. At first, there is a trade-off between the spatial resolution and the framerate in a single camera. Given a constant throughput in readout, a camera might either be used with small images at higher framerate, or vice versa with low-cadence at large images. Secondly, there are several options for the implementation of hybrid camera systems, all of which rely on the concept of synchronized cameras, where one is fast and the other slow. Both cameras can be implemented in the same optical beam in a mounted camera system, a beamsplitter can be used in the same way as in telescopes, or both cameras can be implemented on the same sensor. In all cases, the fast camera is sampling the trace of the motion, and a PSF is calculated from these samples for the deconvolution of the synchronized high-resolution image. It is interesting that the latter case seems to be more stable against NCPEs, since the non-common paths are practically eliminated. However, we like to show details of the third part, where the trace reconstruction is performed. This motion computation is based on the optical flow method, which is not very interesting for this work because it is no standard method from technical astronomy. But we think that the core statement on the registration of blurred images is given in this reference, which is the motion centroid assumption. We use reference [45] for direct quotation:

> Note that the secondary detector, which has a short but non-zero integration time, may also experience some motion blur [...]. We therefore assume that the computed motion displacement between two (slightly) motion-blurred frames is determined by the centroids of the corresponding blur functions. We refer to this as the *motion centroid assumption*.

This motion centroid assumption offers a complete different view on the registration of blurred images. The blur in registered images is not seen as degradation, which hinders the registration. Instead, it defines the shift of an image as the CoG of its blur kernel, which can be detected once the condition of a constant object in several images is fulfilled. For example, it can be intuitively understood that a Fourier-shift can be seen as blur kernel consisting of a shifted Dirac-impulse. Hence, the only difference between a shift and blur might be seen in some metric over the extent of the blur kernel. This is basically the relevant information from the state-of-the-art, and from here onwards this work and the image processing discussion will part. But we show in the following how the authors of [46, 47] proceed, in order to prepare the argumentation for our different

approach.

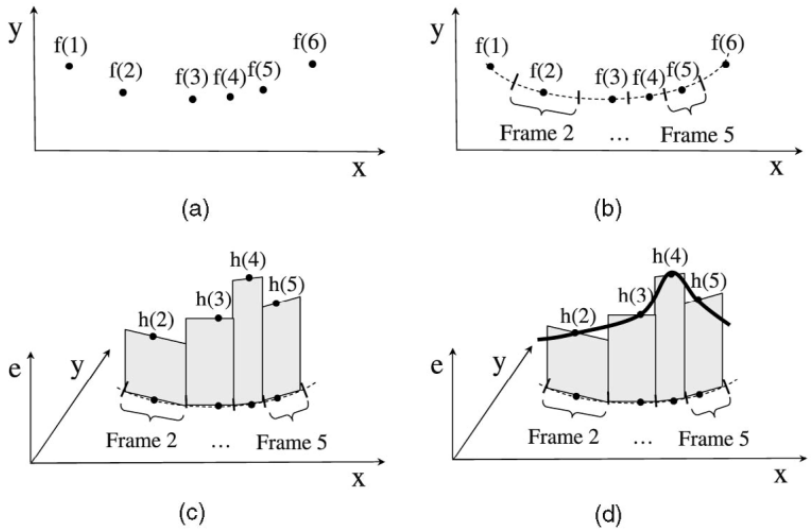

Figure 3.3: Trace reconstruction in hybrid imaging [47].

Figure 3.3 from [47] illustrates the reconstruction of the motion-blur PSF for the long exposure image, which is based on samples of the synchronized short exposure camera in the hybrid imaging system. These samples are shown in part a) of the figure. It is both obvious and important that these samples are defined by the two-dimensional coordinates of the sensor-grid (x, y), and that these samples contain indices which are related to the temporal indexing of the images in the sequence. It can be seen in part b) that a trace is interpolated from these samples. Both parts c) and d) illustrate a kind of constraining of the energy in all short exposure images, so that the acceleration of the camera can be modeled.

The argumentation related to Figure 3.3 in the reference might be seen with certain scepticism for two reasons. It is not in detail explained on the one hand. On the other hand, the proceeding in the reference is not conform to the image formation model. The image formation model has shown that the relative motion between image and object causes motion-blur. If a Dirac-impulse is located in the origin of the object plane, the interpolated trace of this Dirac onto the grid of the sensor is the PSF. Hence, a translational motion might be interpreted as temporally variable coordinate in the two dimensions of the sensor grid. Therefore, we confirm the illustration of the trace. But we do not agree to the interpolation of the trace from the samples, as the samples are always elements of the trace. The trace is given, and a CoG of a curved subtrace can be located next to this subtrace. Furthermore, the trace is a two-dimensional, natural

signal and the vibration has a band-limited power-spectrum. Hence, we can assume that it consists of a finite Fourier-series, which is infinitely often differentiable. This would imply that we do not have to model acceleration and other properties resulting from its derivations, because this information is already included. Thus, the PSF should be nothing more than the projection of the Dirac on the grid of the sensor, in order to match the image formation model as good as possible. Hence, the energy constraining of the subtraces in Figure 3.3 seems unnecessary. Despite the critique, we like to suggest that the motion centroid assumption should be further discussed, and ported to both the image correlation methods from extended scene astronomy and the image formation model. In this context, we register temporally band-limited variations of the coordinates of a point source in relation to the sensor in the next sections, which are infinitely often differentiable, such that the acceleration information is naturally modeled with the trace. Hence, the CoG of a subtrace is not necessarily element of this subtrace, as well.

3.2 Area-based registration of arbitrary blur

The foregoing analysis of the state-of-the-art has shown that the motion centroid assumption is the theory of choice to register blurred images, or, more precisely, the CoGs of the blur kernels in the images of constant extended scenes. For this purpose, we like to anticipate portions of our simulations, in order to illustrate the underlying principle of the registration. Then, we derive the registration of blur for methods from extended scene astronomy, and discuss it intermediately.

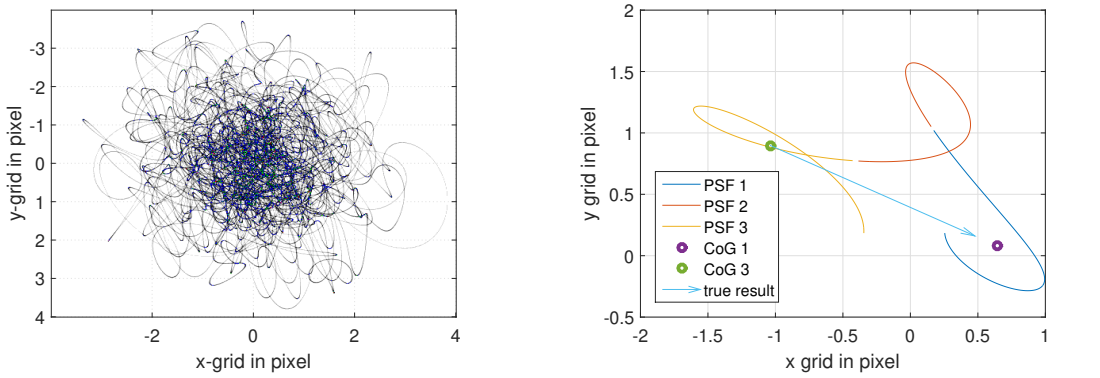

(a) Motion trace in long exposure image.

(b) Subtraces in short exposure images with registration result.

Figure 3.4: Motion traces in a hybrid imaging setup and principle of the registration.

Figure 3.4 illustrates our fundamental assumptions on the hybrid imaging, as discussed in the previous section. Both figures show continuous, band-limited traces of a relative motion between image and object, which would be drawn by an ideal point source on the pixel grid of the sensor. The coordinates of the pixel-grid are sketched in both figures.

It can be seen that the trace in Figure 3.4a extends over larger area and consists of more curves, because the trace has been simulated for an exposure time of the long exposure case. Hence, this trace would define a blur kernel on a slow camera in a hybrid imaging setup. A part of the same trace for a small fraction of the total exposure time is shown in Figure 3.4b, where this case represents photography with the fast camera in the hybrid imaging setup. This shorter part of the trace of the fast camera again is divided into three parts of equal time, where each of these three parts represents an exposure of one frame of the faster camera. Hence, three subtraces are related to three images, where each subtrace defines a PSF for one short exposed image once it is interpolated to the pixel grid of the sensor. This means, we neglect the interpolation of continuous traces to discrete PSFs, and arbitrarily exchange both as they are continuous and discrete representations of the same signals. PSF 1 in Figure 3.4b names the subtrace of the reference image r. The actual image a in the corresponding correlation term is defined by PSF 3, accordingly, and PSF 2 should illustrate that the overall trace is continuous. Two CoGs, corresponding to PSF 1 and PSF 3, are drawn in Figure 3.4b. They define both the shift between the images 1 and 3 due to the motion centroid assumption, and the expected true result of the related correlation with the images 1 and 3 vice versa. The traces are quasi-continuous due to discrete computer-calculations, but they stem from a continuous Fourier series which was equidistantly sampled in time. Hence, all of these samples have the same weight, and the probability to stay and the acceleration are implicitly present in contrast to the hybrid imaging. The latter can be seen in Figure 3.4a only, where weightings of the trace are slightly notable. These weightings result from an interpolation to a pixel grid that is far over-resolved in relation to the real cameras pixel grid. The interpolation of the trace to a PSF is a different topic, and handled later in this work. Relevant in the direct context is that the CoGs are not necessarily elements of the trace between camera and object, such that we cannot expect to derive samples of the trace to be measured directly. But before we handle this topic, we like to show why the registration methods from technical astronomy register the distance between the CoGs of the blur kernels.

We therefore introduce our theory on the area-based registration of arbitrary blur, which is based on a method from astronomy, called object cancellation. Object cancellation was firstly described in [48], and used to estimate the Fried parameter from a time series of photographs of an object through turbulent atmosphere. Here, however, we use [49] to reference the underlying principle. A burst of photographs of the same object is transformed into the Fourier domain. Amplitudes from single images of the burst are divided by averages of amplitudes of all images of the burst, in order to calculate metrics of the amplitudes of the PSFs. We only concern the idea to remove the object from mathematical equations, containing different images of the constant object, in order to find dependencies between their blu -kernels. We give an example how the registration of blur can be understood via object-cancellation, and use the ADF method for explanation:

$$c_{j,k} = \sum_{x,y} \left| a(x,y) - r(x+j, y+k) \right| \tag{3.1}$$

We recall that a and r are images of the same object o, which is coherently degraded by different blur kernels, whereby a blur kernel might consist of several transfer functions. Hence, we can express each image as an individual blur kernel b_a or b_r, which is convolved with the common object o. We also recall the understanding of a discrete blur kernel, in which the image resulting from a convolution with the blur kernel can be seen as sum over weighted and integer shifted copies of the object. Hence, we try to separate the object from those expressions in the blur kernels, which define this weighting and shifting.

$$c_{j,k} = \sum_{x,y} \Big| \sum_{v,w} b_a(v,w) o(x+v, y+w) - \sum_{v,w} b_r(v,w) o(x+v+j, y+w+k) \Big| \tag{3.2}$$

In equation (3.2), the images are written as products of the blur kernels and the object, where the products are scalar-matrix multiplications. The sum over (v,w) is denoted with each blur kernel, as its indices count the kernels rows and columns. Each entry of the blur kernel would shift the object by the indices (v,w) of this entry, and apply a scalar weighting to the object which is given with the entry $b(v,w)$ itself. The application of the scalar-matrix multiplication is possible only, because the related term is located in the sum over all (x,y). Hence, the regarded entry of $c(j,k)$ is a scalar and not a matrix, and the convolution can be simplified. The indices (v,w) have the same value range as (x,y). But the order in which they count is irrelevant due to the sums. We like to remove the object from the correlation term. Hence, we regard the absolute operator and find that positivity of o allows for moving it out of the correlation term, if edge effects in the sampling of the object with Dirac sampling functions are neglected:

$$c_{j,k} = \sum_{x,y} o(x,y) \Big| \sum_{v,w} b_a(v,w) \delta(v,w) - \sum_{v,w} b_r(v,w) \delta(v+j, w+k) \Big| \tag{3.3}$$

Equation (3.3) shows the object removed from the correlation term. It only depends on the indices (x,y). The sum over the object is a scalar, which only would magnify the correlation surface c, but neither change its form nor the registration result. Hence, this term can be neglected. The Diracs remaining from the object express the sampling, i.e. the expected integer based shifting function. The entries $b(v,w)$ do similarly represent the weighting of each integer shift. We denote that blur kernels are energy preserving, such that the sum over each kernel is equal to one. Hence, we can simply divide each term by the sum over a blur kernel:

$$c_{j,k} \propto \left| \frac{\sum_{v,w} b_a(v,w) \delta(v,w)}{\sum_{v,w} b_a(v,w)} - \frac{\sum_{v,w} b_r(v,w) \delta(v+j, w+k)}{\sum_{v,w} b_r(v,w)} \right| \tag{3.4}$$

Equation (3.4) already illustrates our finding that the ADF method calculates the distance between the CoGs of the blur kernels of the inferred images. We find two fractions related to the inferred blur kernels in the equation, where both are definitions of CoG-calculations that consist of the expected weighting and shifting metrics. We further

denote that the term related to the reference image is depending on the indices (j, k), such that it is shifted similarly to the reference image in a normal correlation. Finally, we can denote both terms as CoG of a blur kernel:

$$c_{j,k} \propto \left| CoG(b_a(v, w)) - CoG(b_r(v + j, w + k)) \right| \tag{3.5}$$

All in all, we find in equation (3.5) that the ADF method is formally independent of constant objects, and can be assumed to calculate the distance between the CoGs of the blur kernels of the inferred images.

We give a short conclusion on our registration model. The area-based registration of blur can be modeled on coherent regions via object cancellation. The basis for this idea is the motion centroid assumption. The cancellation can be similarly applied to all other space-based correlation functions from extended scene astronomy. The CFF method can be modeled with the Fourier shift theorem. The modeling is straight-forward for all difference-based methods. Covariance-based methods rely on an element-wise multiplication in the correlation, but the principle is the same until noise is taken into account. Additional noise can be put into a separate correlation term at difference-based methods. Normally, correlated images are dark- and flat-field corrected (compare [5] for example). Hence, the remaining noise is assumed to be zero-mean Gaussian distributed, such that it is normally interpreted as being uncorrelated. In contrast, covariance-based methods would correlate additional noise with image content, but it was not possible to interpret the resulting terms. However, we only like to explain our theory, which is based on the assumption that the common object plays a minor role in the registration compared to the blur. The blur defines several weighted shifts for each correlated image, such that the correlation calculates a result which performs averaging over all implicitly calculated integer shifts. This averaging takes the form of a CoG calculation, since blur kernels consist of weighting and shifting elements, and the energy-preservation implicitly accounts as normalization to one. Hence, we assume that the result of area-based correlation methods is the CoG distance of the blur kernels. One further implication of this model is that the shifts of images can be recognized as the CoGs of their blur kernels. Therefore, one can shift an image via convolution with a blur kernel, for example with a Fourier-shift. We have to highlight that we worked around the interpolation problem so far. This means, we registered the CoGs of blur kernels, but did not explain their relation to the motion traces. In order to connect both, we set the uncommon requirement on the interpolation of traces to blur kernels, which is that the CoGs of both the trace and the related blur kernel have to match. Based on this requirement, we work on the reconstruction of the motion trace in the next section.

3.3 Reconstruction of time series acquired with temporally Nyquist sampling cameras

The last section gave an argumentation why correlation methods calculate the CoG distance between blur kernels. We like to illustrate this principle on a higher level of abstraction, where we consider both the relative position between image and object and the registration results as time series. Translational motion-blur is variant with the time t, and the registration would calculate its results in units of the pixel grid (x, y). We already postulated that the vibration consists of two natural signals, which are continuous and at least twice differentiable. But we also request that these position signals are separable on both axes. This implies that we can consider two separate signals $x(t)$ and $y(t)$ as coordinates of the true trace. The fact, that these time series are the time-variant coordinates of the object in relation to the pixel grid, implies that the blur kernel is the interpolated projection of these coordinates onto the cameras sensor. We gave no statement on the type of the interpolation, but we requested that the CoGs of both, each trace and its interpolated blur kernel, should be equal. Hence, we can allow for a transition from the registration result that depends on the blur kernel, to the input trace which defines the relative motion between image and object.

A normal operation of a hybrid imaging process would result in a huge amount of short exposure images; in Sunrise, for example, several thousands are acquired during the integration of one long exposure image. The first short exposure image in such a burst normally is the reference image r, and all other images are registered in relation to this reference. This is simply caused by the real-time requirement in the AO. Alternatives are conceivable for a registration with FSP, but currently not of interest. As we postulate separability, we only describe the registration results on the x-axis, which take the form:

$$CoG[x(t), n \times t_s, \tau] - CoG[x(t), 0 \times t_s, \tau]. \tag{3.6}$$

Equation (3.6) is very similar to equation (3.5), but we name the relevant differences. Firstly, the result of the correlation was split due to separability in two independent results on both axes. Hence, we regard the term on the x-axis only, and assume that the y-axis is handled equally. Secondly, we regard a discrete times series ([...]), which is n times equidistantly sampled at the multiples of the sampling time t_s. Hence, the registration results are indexed with the time points $n \times t_s$, where the $0 \times t_s$ refers to the acquisition of the reference image. Thirdly, we denote the CoGs in dependence of the true trace $x(t)$, while knowing that the registration results depend on the blur kernel. Thus, we neglect interpolation to the pixel grid and apply the requirement that both CoGs have to match. Next, we have introduced the variable τ, which is the duty-cycle of the camera, i.e. the exposure time of the sensor per sampling time t_s. Finally, we neglect errors of the image registration, which have been introduced in the fundamentals.

If both time-series have a indexing n and a length N of several hundred to several

thousand samples, one can simplify equation (3.6):

$$\begin{aligned} & CoG[x(t), n \times t_s, \tau] - CoG[x(t), 0 \times t_s, \tau] \\ -mean\Big(& CoG[x(t), n \times t_s, \tau] - CoG[x(t), 0 \times t_s, \tau] \Big) \\ = & CoG[x(t), n \times t_s, \tau] \end{aligned} \tag{3.7}$$

Equation (3.7) subtracts the mean value of the time series of the CoGs of the trace from this time series itself. This is possible, because the signal $x(t)$ is zero-mean as it is a random jitter. It will become clear that the continuous CoG of a zero-mean signal is zero-mean is well, but we refer to this a bit later. Meanwhile, we suggest to regard the time series simply as CoGs of the input signal $x(t)$, which has no offset on each sample due to relative registration to the reference image.

Our interest is to recover the continuous time series $x(t)$, and its discrete CoGs are known. We use the fact that there is a well know relation between both, which is the boxcar-function in the signal domain that corresponds to the sinc-function in the Fourier domain. This is of course only valid if the sampling moment is adjusted in such a way as it is centered to the integration time. We express this via the exposure time $t_{exp} = \tau \times t_s$, which is active during $[n \times t_0 : n \times t_0 + t_{exp}]$. The correct time points of sampling can be defined at $t_s = n \times t_0 + \Delta$, so that $\Delta = t_{exp}/2$. The normal ansatz for the boxcar-filter is given with the existence of a Fourier series of the continuous signal, and can be seen as fundamental knowledge:

$$x(t) = \sum_k A_k cos(\omega_k t + \varphi_k) \tag{3.8}$$

Equation (3.8) shows the signal $x(t)$ as Fourier series, with frequency index k, amplitude A, frequency ω, and phase ϕ. The DC-component is zero, because the input signal $x(t)$ is zero-mean. We know the discrete CoGs of $x(t)$, and we search the signal $x(t)$. Hence, we assume that the sensor directly integrates over the time series $x(t)$ via symmetric integration boundaries:

$$CoG(x(t), t_s, \Delta) = \frac{1}{2\Delta} \int_{t_s-\Delta}^{t_s+\Delta} \sum_k A_k \cos(\omega_k t + \varphi_k)\, dt \tag{3.9}$$

The derivation of the sinc-function is normally done in two steps. Application of the sum rule in integration allows for regarding each single harmonic $x_k(t)$ separately, and the trigonometric addition formulas are used to simplify the resulting terms to:

$$CoG(x_k(t), t_s, \Delta) = \frac{sin(\omega_k \Delta)}{\omega_k \Delta} A_k cos(\omega_k t_s + \varphi_k) \tag{3.10}$$

Equation (3.10) gives the dependence of the continuous CoG of each frequency $x_k(t)$ from this harmonic itself. This relation is invertible for a discretely measured signal

$CoG[x(t), n \times t_s, \tau]$, if the true signal is at least Nyquist-correctly sampled. Hence, we require Nyquist-sampling of the spectra of motion from here on, and denote the resulting reconstruction of the discrete trace:

$$x[n \times t_s] = \mathcal{F}^{-1}\left(\mathcal{F}\left(CoG[x(t), n \times t_s, \tau]\right) \circ H(k)^{-1}\right),$$
$$\text{where } H(k) = \begin{cases} 1, & \text{if } k = 0 \\ \frac{sin(\frac{\pi k \tau}{N})}{\frac{\pi k \tau}{N}}, & \text{else} \end{cases} \tag{3.11}$$

Equation (3.11) calculates discrete samples $x[n \times t_s]$ of $x(t)$ from the measured, discrete time series $CoG[x(t), n \times t_s, \tau]$, which is defined as offset-corrected registration results from a sequence of images. Nyquist-sampling of $x(t)$ allows to reconstruct the discrete signal $x[n \times t_s]$. We utilize the discrete Fourier transform for application of the filter without convolution. It is denoted that the sinc function is continuous continuable at the origin with the value one. Hence, both the averaging process and the reconstruction do not affect the DC-component. This explains why it is possible to subtract the average in equation (3.7). Furthermore, it identifies this step as unnecessary for the reconstruction. But this subtraction of the mean can be used to correct for different offset on the four polarimetric channels of FSP.

3.4 Verfication of the theory

The last two sections have presented two main theses of this work: Correlation-like image registration calculates the CoG distance of the blur kernels of the images, and a boxcar-filter is advisable for the reconstruction of the relative position between object and image. The reconstruction of this time series further sets a requirement of Nyquist-correct sampling of the signal. In contrast, the registration of blur is independent of this requirement. In this section, we verify both theories from the last sections in one experiment. The idea is to measure the curve of the filter via registration of blurred images. This is done in a test setup, which implements a correlation tracker with a tip-tilt mirror, as is illustrated in Figure 3.5. The mirror is stimulated with a defined vibration consisting of a single frequency, while the filter is varied between acquisitions of several time series. In a second experiment, we perform a similar measurement on intensity-variations, which are induced by an LED controller.

Figure 3.5 shows a test setup that was built within the scope of this thesis. It was initially dedicated for different tests than the verification of the boxcar-filter, but the findings from the previous sections changed its role during its implementation. Hence, we come later to the initial purpose of this setup, and introduce here the required part only. A test pattern is backside illuminated with a controlled LED, which works in combination with a collimating objective in front of the tip-tilt mirror as projector. The resulting beam is reflected by a fast tip-tilt mirror and a second fixed mirror onto one

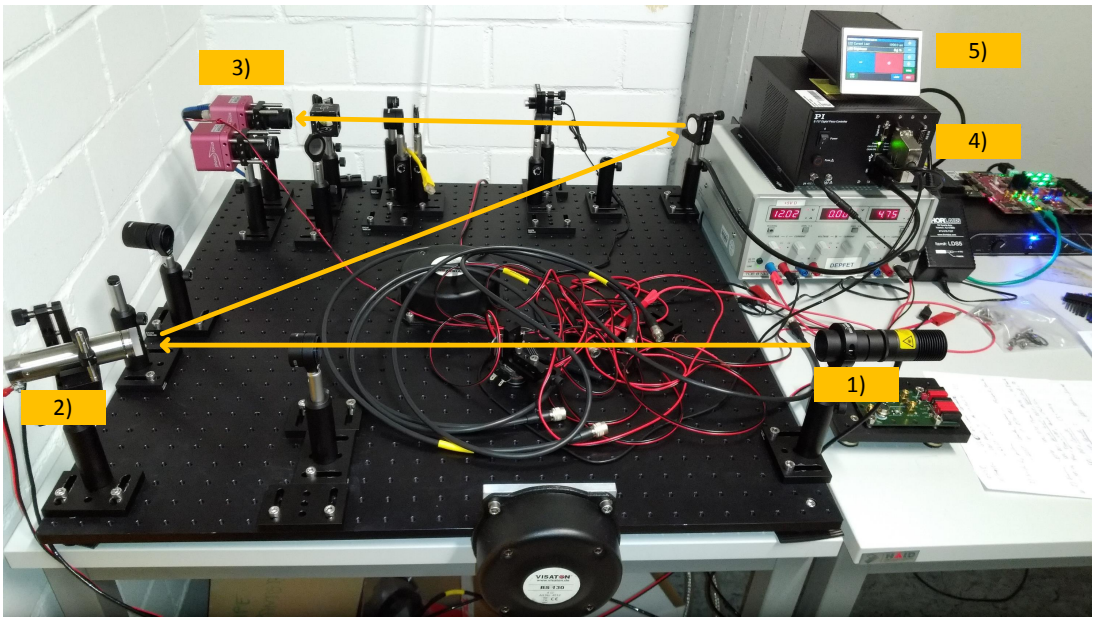

Figure 3.5: Correlation tracker setup at the final implementation stage. Relevant parts: 1) test pattern projector, 2) tip-tilt mirror (PI S-330), 3) cameras (Photonfocus MV1-D1024E-80-G2), 4) tip-tilt controller (PI E-727), 5) LED controller for backside illumination of the test pattern (Thorlabs DC2200 at 660nm). Optical axis is drawn in yellow arrows.

camera, which includes a focusing lens. The tip-tilt mirror is controlled from a workstation PC via the tip-tilt controller, so no control loop is activated.

For the first experiment, we stimulate the tip-tilt mirror with a frequency of 10 Hz on both axes, and adjust a framerate of the camera slightly above 20 Hz. This grants for the required Nyquist sampling of the resulting variation of the relative position between camera and object. Then, we vary the exposure time, which can be seen as the width of the boxcar-filter. We specify the width of the filter with Δ/t_s, such that we vary in the possible range of $[0 : 0.5]$. For each width of the filter, we photograph and register a time series of several seconds, and subtract the mean value of each single series like specified in equation (3.7). Next, we calculate the amplitudes in units of the pixel-grid from all time series acquired. In order to illustrate the curve of the filter, we normalize each amplitude to the maximum amplitude out of all calculated amplitudes. We further plot these normalized amplitudes against the specified input width of the filter. Then, we find the amplitudes coarsely drawing the curve of the filter. Results are illustrated in Figure 3.6. Furthermore, we plot the filter in Figure 3.6a. One can see that both measurements approximate its curve. We assume the inaccuracies in this plot to be caused by the inaccuracy of the image registration, which was introduced in the fundamentals. It can be seen that the absorbed energy increases with the width of the filter. Figures

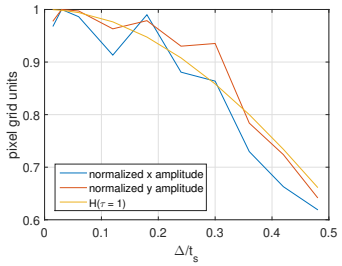

(a) Measured and calculated filters.

(b) $t_{exp} = 1250us$

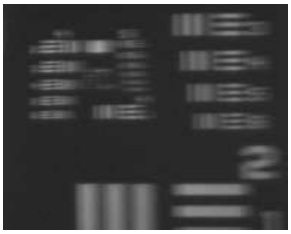

(c) $t_{exp} = 40000us$

Figure 3.6: Verification of the boxcar-filter on time series of temporally variable positions between image and object. The absorbed energy is found in the blur.

3.6b and 3.6c show images of time series of the minimal and maximal exposure times. It can be seen that the blur extents depend on τ as well. We come to the intermediate conclusion that our theses are validated, i.e. image registration methods from extended scene astronomy calculate the CoG distance of the blur kernels and the boxcar-filter is needed to calculate from these CoGs back to the trace. This further validates the Nyquist criterion for the sampling of the spectra of the jitter.

We see the previous experiment in a more general way, such that the relative position between object and image is not the only conceivable time series that is measurable with cameras. But we think it is a very fundamental one, which comes as the image can be seen as two-dimensional distribution of positions that are weighted with intensities. From this point of view, the second property which is directly measurable via cameras should be the intensity. Even more in general, one could assume that all conceivable time series measurable via cameras are based on the two variables of position and intensity. This view suggest the need for validating the boxcar-filter on time series of varying intensities, as is done in the next experiment.

In the second experiment, we place the LED directly in front of the camera and adjust a strong out-of-focus, which results in a flat illumination of the cameras sensor. We use the LED controller for varying the intensity on the camera. The variation of the intensity followed thereby a sine-wave, which covered nearly the complete bit-depth of the camera. The LED controller has a minimal adjustable frequency of 20 Hz for these intensity variations. Hence, we decided to use a higher framerate of 800 Hz at the camera for sampling the intensity variations. The higher framerate also enforces a smaller field of view, for which we used 15×15 pixel. The maximal frequency of intensity variations is limited by the cameras framerate, and thus set to 380 Hz, this time slightly below the Nyquist sampling. The boxcar-filter is not only depending on the filter width. It is also possible to hold the filter width constant, and to vary the sampled frequencies, in order to draw its curve. This does reconstruct the filters curve similarly, and we avoid

measuring a non-linearity of the camera with this procedure. Hence, we measure time series of varying intensities, where all time series have different frequencies between 20 and 380 Hz. The normalization is done equivalently to the last experiment. Results are shown in Figure 3.7 for a duty-cycle of $\tau = 0.8$.

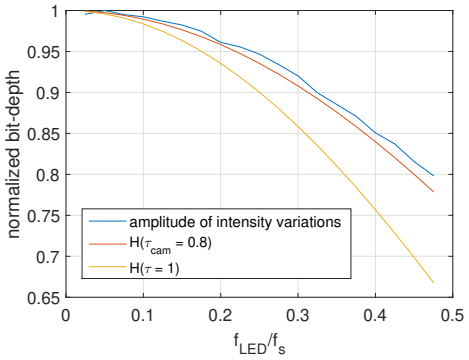

Figure 3.7: Filtering effect as measured on time series of varying intensities.

Figure 3.7 shows measurements on variations of the intensity. It can be seen that the error from the image registration is not present in this test. But the minimal adjustable frequency of 20 Hz of the LED controller enforced us to normalize to amplitudes below the theoretically achievable one, which explains the slight difference between measurement and reference. All in all, one can find a much better verification in this case. We refer with this case to equation (3.11), where only the discrete signal $x[n \times t_s]$ is reconstructed from the measurement. This is due to the fact that the inaccuracy of the image registration hinders the reconstruction of the continuous signal $x(t)$. We have not investigated the reconstruction of continuous brightness variations via up-sampling, but we think that this should be possible in theory.

3.5 Extension of the image formation model to the temporal domain

The last section presented two experiments. In both cases, we shot bursts of images and extracted underestimated time series of either a position information or an intensity information. We stated that we see both time series as the most fundamental ones which an image can have, since we see the image as two-dimensional intensity distribution. In this section, we formulate a conjecture following from the previous findings and its impact on an even higher abstraction layer: Each measurement of a time series via cameras seems to be affected by the exposure time, whose duty-cycle always acts like a filter on this time series. Even if we have not validated this statement on all possible time series, we have shown that there is no restrictive dependence on a single type of time series. Hence, we allow ourselves to formulate this more general view as hypothesis. In this hypothesis, the boxcar-filter is regarded under its property that

it is a pure MTF along the temporal domain, and it is compared to the same MTFs along the spatial coordinates, which are already described in the image formation model.

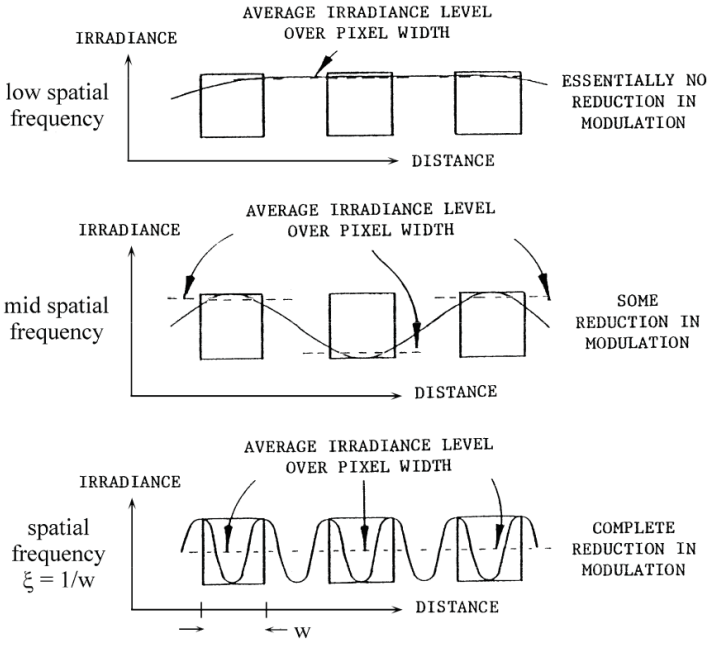

Figure 3.8: Detector footprint MTF [29].

Figure 2.5 from [29] placed the sensor in the focus of the optical black box, and was described with a short statement on the integration properties of its detectors. Indeed, reference [29] continuous with the so called detector footprint MTF, before it describes the MTFs resulting from motion and vibration, which were introduced in Section 3.1 with the state-of-the-art. We like to cite [29] again, in order to explain this intermediately described detector footprint MTF. Figure 3.8 from [29] shows that the spatial extent of each detector damps the spatial amplitudes of the image. The damping is thereby similar to the one on time series, except that this case is spatial and normally two-dimensional. The figure shows three cases of such spatial damping in one dimension. Firstly, a low spatial frequency in intensity is pretty constant over one detector, such that the averaging due to integration in each detector is very low. This means, the detected integrated charge is close to the true sample in the center of the detector. Secondly, for a mid-spatial frequency, some difference between the averaged, integrated charge and the true spatial amplitude can be seen. The third scenario, where the detectors extent equals the spatial period of the signal, leads to a complete reduction in modulation, such that there is no detectable spatial intensity variation with a detector of this particular size. This damping in amplitude is further described with a two-dimensional boxcar-function in the spatial domain, which corresponds to a sinc in the Fourier domain. One main

difference between our work and this illustration is that [29] handles sampling below the Nyquist criterion, which can be seen in the third case of Figure 3.8. But we like to point out the similarities: band-limited signals are sampled, independently of their content, with sampling functions that are no Dirac-impulses, either the detector extent in [29], or the exposure time in our results, and the application of the boxcar-filter for error-description and signal reconstruction. Hence, we presume that we have extended the image formation model to the temporal domain. The detector is not only integrating along the spatial dimensions of the sensor, but furthermore during exposure time. One might extend the model by assuming that the sensor is able to acquire a sequence of images, which introduces the framerate, the duty-cycle, and at least two conceivable time series into this model. Then, each sample of a time series is imperfectly extended along the investigated temporal dimension, what directly results in the well known MTF from the spatial case, and damps the amplitude of the time series. We also presume that other sampling functions might occur, for example unshuttered CCDs might have different temporal transfer functions, as is suggested later in case of readout smear. All in all, we presume that cameras have temporal sampling functions, which are degrading all temporal variations of properties of the object that are measured in sequences of images.

We like to give a short conclusion on this chapter. Initially, we found the image registration to be the method of choice for the calculation of those PSFs resulting from vibration, which are mandatory for image deconvolution in the long exposure case. But the application of image registration is limited to static scenes, in which image degradation stems from atmospheric turbulence. Hence, we tried to relax the related requirements. We argued that motion-blur is present, when micro-vibrations are registered. And we found the motion centroid assumption to be the theory of choice for the registration of this motion-blur. Thus, we ported the registration of blur to area-based image registration methods. It was not necessary to change the known standard methods. Instead, it was shown why these methods register the CoG-distance between the blur kernels. The application of the image formation model led to an understanding of both the dynamic shift in images and the underestimation of time series amplitude. The underestimation of time series amplitude acquired with cameras was shown to be a more general problem. The exposure time acts like a sampling function, or like an MTF, once the temporal domain is investigated. This was validated in a test-setup for the two most fundamental time series from cameras, and led to a proposal for the extension of the image formation model. All in all, we think we found a suitable, dynamic model for the handling of translational motion-blur induced from vibration. We embedded this explanation in the scientific context, be it technical astronomy, motion-deblurring, or the image formation model. Hence, we set our focus on the practical application of our theories, and simulate the registration of blur with the Sunrise AO and the FSP camera in the next chapter.

4 Simulations of micro-vibrations on Sunrise

The imaging on Sunrise can be categorized as long exposure case, which implies that the overall PSF has to be known if the object should be reconstructed via post-facto processing. The standard method for measuring this PSF is identified as image correlation from extended scene AOs, and reinterpreted as a registration of blur in the last chapter. Furthermore, an underestimation of the amplitudes in related time series is found, which can lead to a requirement for the application of a boxcar-filter that reconstructs this series. This chapter presents several simulations, which measure the performance of blurred image registration in operation points of the Sunrise telescope. Most fundamental in this context are some questions that already arise when the motion-blur is applied to the images. Examples are the generation of the signals $x(t)$ and $y(t)$, the interpolation of these traces to PSFs, and some boundary conditions like the telescope MTF, for example. These topics are discussed in Section 4.1, and we describe them as generation of images for computer simulations. Two different camera settings are distinguished. These are AO operations where the jitter is temporally oversampled (Section 4.2), and high-cadence scientific cameras with relatively long exposure times (Section 4.3). Our focus is thereby on the accuracy of the signal restoration, be it the registration results, the time series, or the PSFs. Hence, we start with a sensitivity analysis on the AO operation, which is useful for understanding the influences on the accuracy and for layouting future AOs that measure vibrations. Furthermore, we illustrate the effect of aliasing in case of registration with high-cadence science cameras, because the filter reconstruction is mandatory in such cases. Finally, we show deconvolution results related to all simulation runs in Section 4.4, and conclude our work on micro-vibrations.

4.1 Image generation

The fundamental question arising with the task of simulation is how to match reality. Our strategy might be seen as rigorous simplification, since our basic concept is the focus on the image formation model instead of the telescopes hardware. We simulate a smaller part of reality as might be conceivable, but we still have to highlight several prerequisites and common problems with the generation of computer-simulated images. This is of special importance, since the scientific net data is acquired as image, the subaperture is represented by an image, the measurement in AOs works on images via correlation, and the post-facto correction is based on images. We regarded this abstract image, and found that the degradation resulting from micro-vibrations can be seen as motion-blur PSF. It is further known from the image formation model that images degraded by several

subsystems, i.e. concatenated optical black boxes, are represented by objects which are convolved with each of the related transfer functions [29]. We extend our image model to one that covers both, a PSF p and a telescope transfer function m, where p has a phase unequal to zero and m is a pure MTF:

$$i = o * p * m + n \tag{4.1}$$

Equation (4.1) is just the same model as (2.2), but it respects two subsystems. It was shown that telescopes are limited in resolution by the Airy disk, which is a pure MTF. This is of course an ideal assumption, and real telescope MTFs are much more complex. But the assumption that the phase is zero is good, and the damping of the contrast is significant [50]. Hence, we respect an MTF in all simulations, but the Airy disk is sufficient since we only like to cover the impact of a zero-phase kernel on the image registration, instead of performing case-studies. Interesting is that we found two arguments predicting that the Airy disk has no influence on the registration. Firstly, its zero phase does not apply a shift, because it enforces symmetry. Secondly, it is constant during the registration of a sequence of images, such that it might be canceled with the object from the correlation terms. However, these assumptions are unproven yet, and the Airy disk is respected in order to validate these assumptions.

The second subsystem in our optical black box describes the jitter, and its application via the PSF p is expected to cause translational shifts which can be registered. The PSF was introduced as the projection of an ideal point source, whose arbitrary trace is interpolated on the sensor grid of the camera. Hence, two question arise in this context: How to get the trace, and how to interpolate it on the sensor grid?

The question for the trace is easy to solve, because we found an equivalence between the CoG of a blur kernel, and the corresponding CoG of the related subtrace. Hence, we argue that we have a reference for such traces, which is given with the PSDs of the micro-vibrations that have been measured in both flights. This is of course no trace in its original meaning. We only have the amplitudes from a discrete measurement, and we know that there are errors in the measurement due to amplitude underestimation and accuracy of the image registration. But the utilization of these amplitudes is the best starting point that was found in this work, because the traces are straight-forward to generate and the power-spectral information remains.

Figure 4.1 shows power-spectra calculated from PSDs, which have been recorded on both Sunrise flights as residual tip-tilt errors in the AO [18]. The fundamental time series are of either 4 or 5 seconds, and have been strongly over-sampled. Hence, the underestimation of the amplitudes is expected to be low. It was confirmed that the RMS value from the PSDs matches the reconstructed blur kernels in the scientific images [18]. However, we have calculated the amplitudes from the PSDs, and we checked the RMS-values via Parseval's theorem. We multiplied the amplitudes with uniformly distributed random phases, in order to derive random time series with the same power-spectral information via inverse Fourier transformation. These time series are zero-mean

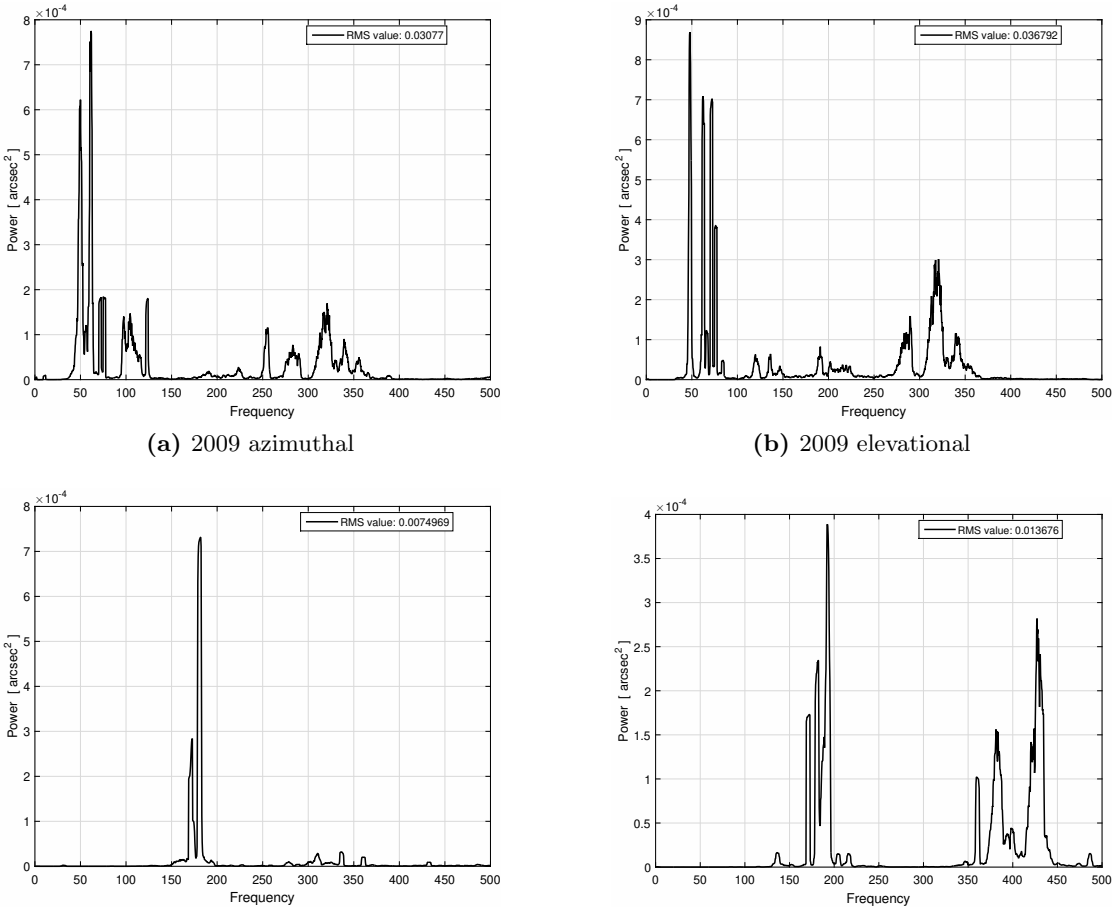

(a) 2009 azimuthal

(b) 2009 elevational

(c) 2013 azimuthal

(d) 2013 elevational

Figure 4.1: Power spectra of the residual tip-tilt error of the Sunrise fligths. Frequencies below 10 Hz are not reliable. Frequencies above 500 Hz are cut off.

random signals, and thus quite uninteresting to show. We name azimuthal series $x(t)$, and elevational ones $y(t)$, since we focus on image processing. Both time series are regarded as continuous signals in the Fourier domain. This means, we can simply use Fourier-shifts, in order to interpolate the time series to the specified amount of samples that is required. This allows for arbitrary adjustments of the framerate and the required amount of samples per subtrace. Hence, there is no binding of these variables to certain parameters in the later simulations, and we simply regard continuous traces that are free to sample.

More problematic is the question for the most suitable interpolation method, because interpolation is a topic which is subject of many discussions. We like to illustrate the problem with a reference on a survey in interpolation [51]. It can be found that several hundred references would exceed the scope of this work, while still not offering an

undisputed solution to our problem. Hence, we do not claim to use optimal methods, or to have evidences for certain properties of them. But we can offer a description of some aspects that arise with the question for the interpolator. Firstly, our image model enforces us to interpolate a PSF instead of an image, which could be interpreted as convolution based interpolation of the image, and as a connection to other studies where images are directly interpolated. Secondly, we already introduced the requirement for the equivalence of the CoGs in both the blur kernels and the traces. Next, we respected that the object is given as discrete image, and not as continuous distribution of point sources. Hence, we chose an interpolator that has the extent of a detector in the object plane, because we implicitly shifted this discrete object. Finally, we think that the interpolator only has a minor role in the verification of our theories. This is, because we intend to reconstruct the fundamental signals for error description, e.g. $x(t)$ and $y(t)$. If we compare several signals that rely on the same interpolation method, the method itself plays a minor role in the comparison. This is different in real DWFS applications, where the interpolation method has to match reality somehow. But such a setting is not covered in this thesis, and a real application of our theory might be handled similarly as in standard DWFS. Hence, we only have a hard requirement on the CoG preservation, but the interpolation method is exchangeable beyond this request.

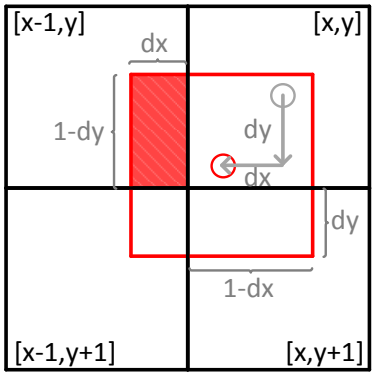

Figure 4.2: Interpolation of trace tuples to PSF samples.

Figure 4.2 illustrates the used interpolation of trace tuples to PSF samples. The position of a trace tuple is shown as a red circle on the sensor grid. The subpixel shift (dx, dy) is defined from the closest pixel $[x, y]$ (gray circle). A virtual pixel around the trace tuple defines four areas on adjacent pixels on the PSFs grid. Each pixel on the grid of the PSF is additively applied with a fraction of this virtual pixel corresponding to the overlapping areas. This way, we interpolate each tuple of the 2D trace to a sensor grid and calculate a motion-blur PSF, which is finally normalized to one. All motion-blur PSFs in this work are interpolated with the method described here, also the over-resolved one from Figure 3.4a.

Some other aspects can be addressed within the image generation. The convolution with a PSF is known to cause edge-effects. We avoid them by simply cutting parts from bigger images after application of the convolution. The Airy disk is applied via convolution as well. Hence, the continuous disk also is discretely sampled to the sensor grid, but we do not use interpolation since we reused source code from [52]. It was already stated that we do not investigate noise in detail, but we respect zero-mean, additive, Gaussian distributed noise in all simulations. Noise depends on the particular setup, as well as image size, photon budget, contrast, and the angular spatial sampling. Hence, we introduce such parameters in the next sections separately with the cameras.

Despite some changing parameters with different cameras, the object is always the same. We use images of simulated solar surface, which are provided by the MPS [18]. One simulated subaperture from the Sunrise AO with FSPs spatial sampling can be seen in Figure 4.3a, as well as the fundamental object (Figure 4.3b). Both are scaled in order to highlight the degradation, what distinctly enhances the contrast in both images.

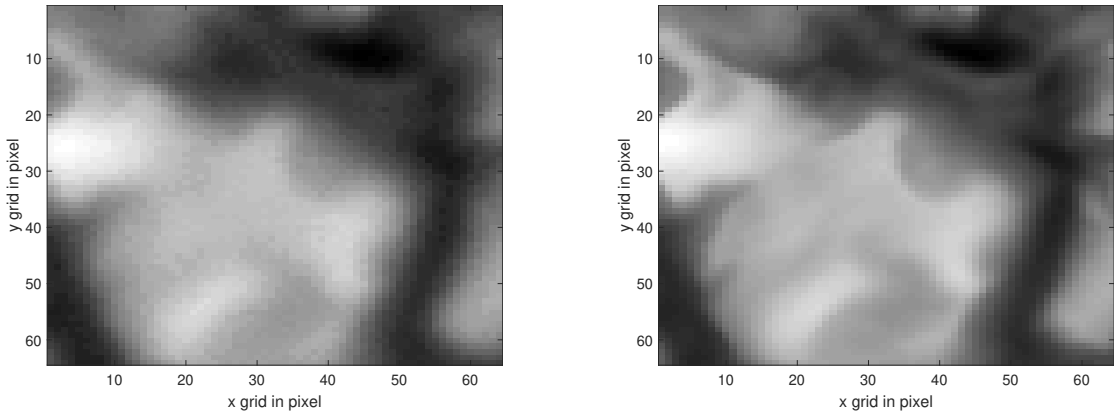

(a) Simulated AO subaperture **(b)** Object

Figure 4.3: Simulated, fully degraded image and object.

Finally, we explain the fundamental difference between the simulations for the AO operation and the ones for FSP. The image degradation due to micro-vibrations is temporally variant. It depends on the framerate of the camera, its duty-cycle, and the spatial sampling of the telescope, if the PSDs are constant. We vary the framerate of the camera and hold the duty-cycle and the spatial sampling constant, in order to show the resulting variations of the spatial extents of the blur kernels. Figure 4.4 shows simulated elevational extents of the motion-blur kernels for the Sunrise flights in 2009 (Figure 4.4a) and 2013 (Figure 4.4b). The spatial sampling is 0.0287 arcsec/pixel and related to FSP, the duty-cycle is one. Mean extents along one axis are shown in red. The value range is shown in blue. It can be seen that these extents of the blur kernels decrease with the framerate. The 2013 power spectrum with lower energy leads to better results as well. Azimuthal blur extents are not shown, but look similar to elevational ones. Interesting is

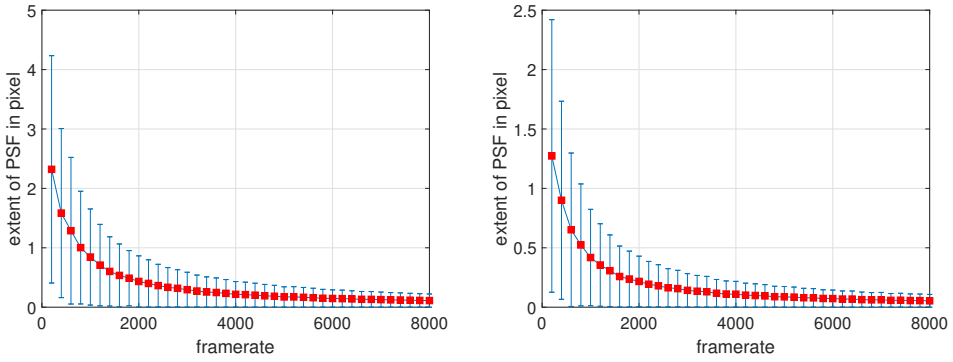

(a) 2009 elevational **(b)** 2013 elevational

Figure 4.4: Calculated elevational extents of motion-blur kernels depending on the framerate.

that FSP would process images with motion-blur with extents significantly larger than one pixel, while AO operations work on kernels with mainly subpixel extents. Hence, we investigate both cases in the next sections.

4.2 Registration of blur in the Sunrise AO

Our work with the registration of blur led to some clear theoretical results, which have been explained in the last chapters. But we also have to highlight a practical finding, which is that the accuracies of both, normal image registration and registration of blur, depend on nearly every parameter which can be set. Furthermore, these dependencies are not really understood in literature. Hence, it is decided to show a sensitivity analysis in order to illustrate these dependencies. The measurement of the sensitivity is done by simply varying each parameter around a specified value in a fixed operation point, and regarding the development of the RMS-error under these variations. We use operation points of the Sunrise AO as reference, because we found that the Sunrise AO has registered the blur sufficiently. The Sunrise AO is a good example for a typical low-order AO, which are partially used to measure image degradation from micro-vibration. The missing sensitivity analysis on such measurements was criticized in the last chapters.

Two different operation points are conceivable once the Sunrise AO is investigated, which is due to the fact that the AO was optimized for the second flight [10]. The reduction of six to two subapertures during closed-loop operations allowed for a higher framerate on the second flight, which has resulted in lower latency in the control loop that again enforced an increased bandwidth and lower residuals. We found that both cases are quite similar in a sensitivity analysis, and we thus decided to investigate the setting from 2009 as a worst-case scenario.

The sensitivity analysis requires a well defined operation point, and we use the speci-

fication of the AO of Sunrise from [5]. All of the parameters which specify the operation point are varied around their value in the operation point, and the RMS error of the image registration is monitored under this variation. Hence, we illustrate the sensitivity from all possible variations on the RMS error, in order to show the prerequisites on the registration of blur. The AO of Sunrise has operated the CFF algorithm, but we simulate all conceivable algorithms from extended scene AOs. Hence, all plots show variations over several algorithms. The operation point is defined as follows: Each correlated image is defined by a subaperture of 64 pixel squared, which implies that the image size can be varied for example. Next, each pixel is specified in quantization with a bit-depth, i.e. the bit-resolution with which the intesity is measured. The average pixel value in the images before quantization is given in electrons, it was $160ke^-$ in charge wells of $200ke^-$ capacity. The operation point further contains a normalized RMS-contrast of the images of six percent. The noise is given with $270e^-$ before quantization. The spatial sampling is critical with 0.2 arcsec/pixel at $550nm$ for the one meter aperture, and the framerate is given with 1.7 kHz for 2009. We have to say that we do not vary the spatial sampling directly, but the diameter of the Airy disk instead, which is due to the fact that the spatial sampling of the object was fixed. However, the operation point is defined, the RMS error monitored, and the possible variations are shown next.

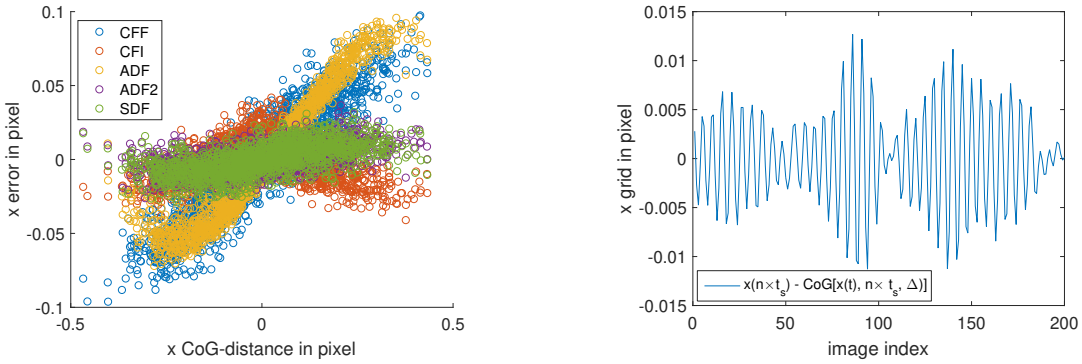

(a) Error-curves based on CoGs.

(b) Error due to CoG calculation.

Figure 4.5: Simulated accuracy of the image registration in the operation point.

Figure 4.5 shows measurements on the accuracy of the image registration in the operation point. In Figure 4.5a, the true shifts based on the CoG distance are plotted against the errors of the registrations, where we simulate one second AO operation for all algorithms from extended scene AOs. The CoG distance is the true registration result, but not the reconstructor of the trace. Hence, we show in Figure 4.5b the distances between the mid sample of each subtrace to the CoG on the x-axis for 200 samples. One can find that the error induced by the CoG calculation is negligible in comparison to the error of the registration. Furthermore, the value range of the shifts is larger than the one of the errors. Hence, we focus on Figure 4.5a. We find subpixel error-curves for

several methods, as is usual in image registration [32, 33, 53]. Furthermore, all curves show mean errors of zero. The CFF method utilized on Sunrise performs worst in this setting. It can be seen that the shifts do not exceed the value range of ±0.5 pixel.

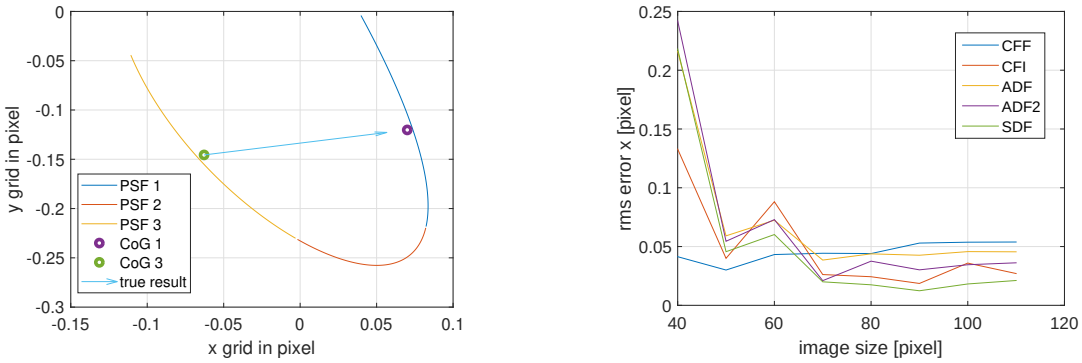

(a) Registration principle. **(b)** Scaling of the image size.

Figure 4.6: AO parameter variations with motion-blur (1).

Figure 4.6 depicts the registration of the CoGs of the continuous subtraces as before (Figure 4.6a), and a scaling of the size of the images (Figure 4.6b). At first, a comparison with Figure 4.5a may illustrate the relation of blur extents in comparison to shift-distances and errors. The blur extents are of up to half the size of the shifts, such that the CoG definition seems relevant from this perspective. But it is only important that the CoGs of the blur kernels are close to elements of the trace, such that a trace reconstruction is expected to work. A scaling of the size of the images in pixel (Figure 4.6b) shows that CFF is already in saturation. CFF might work best on smaller images, but other methods would further profit from an increase of the image size to at least 70×70 pixels. Very interesting is the increase of the RMS-error for image sizes at 40×40 pixel. It can be presumed that very large subapertures are mandatory for the registration of blur. Vice versa, we think that standard AOs with subapertures below this size mostly do not measure micro-vibrations correctly. But these presumptions remain unverified, because they are not in the scope of this work.

Figure 4.7 shows the behavior of the RMS-errors under variations of contrast (Figure 4.7a) and noise (Figure 4.7b). The RMS-error significantly increases for RMS-contrasts below two percent, but experiences saturation for higher values. All algorithms are pretty stable against noise. The improvement of the ADF method with increasing noise was repetitively measured, but is not in the focus of this work. We only conclude that noise-amplifications are not limiting whenever they are in a reasonable range.

Figure 4.8 illustrates variations in the quantization (Figure 4.8a), and in the strength of the input jitter (Figure 4.8b). The quantization of eight bit must not be reduced,

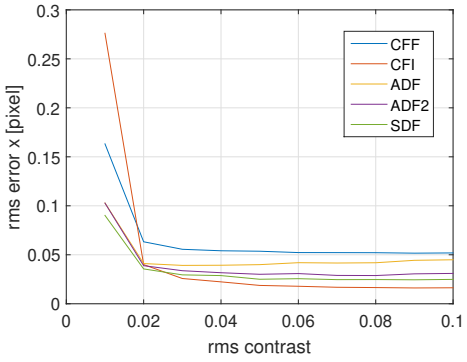

(a) Contrast variation.

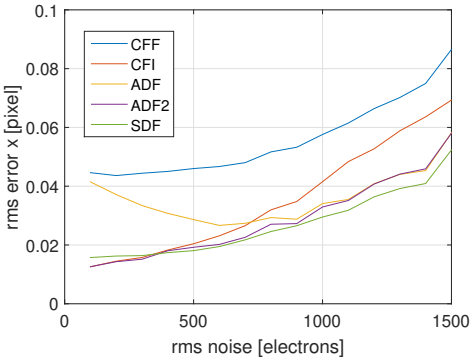

(b) Noise variation.

Figure 4.7: AO parameter variations with motion-blur (2).

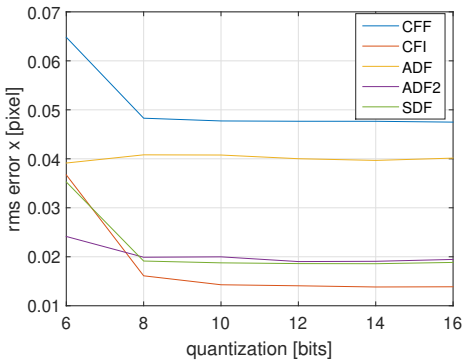

(a) Quantization variation.

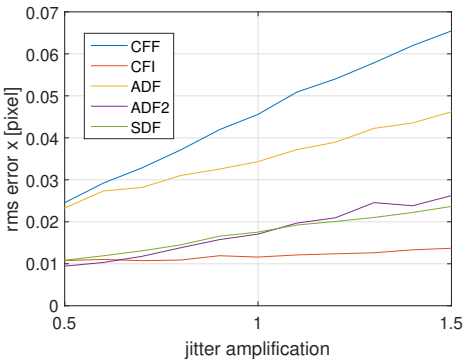

(b) Jitter amplification.

Figure 4.8: AO parameter variations with motion-blur (3).

but an increase would only serve as guarding distance. The jitter amplification is not causing shifts beyond one pixel, but differently steep linear trends can be recognized.

Finally, we show variations of the framerate and the radial scaling of the Airy disk (Figure 4.9). Figure 4.9a shows measurement uncertainties only, which we assume to be caused by variations in the blur kernel of the reference image. A generation of new traces for different framerates could not be avoided. Finally, Figure 4.9b shows the impact of a radial scaling of the Airy disks diameter. This is of special importance in this work, since FSP on Sunrise would sample beyond the Rayleigh criterion. Following our simulations porting the AO algorithms would basically work, but a higher RMS-error has to be expected.

We interpret our results from the sensitivity analysis. They are phenomenologically

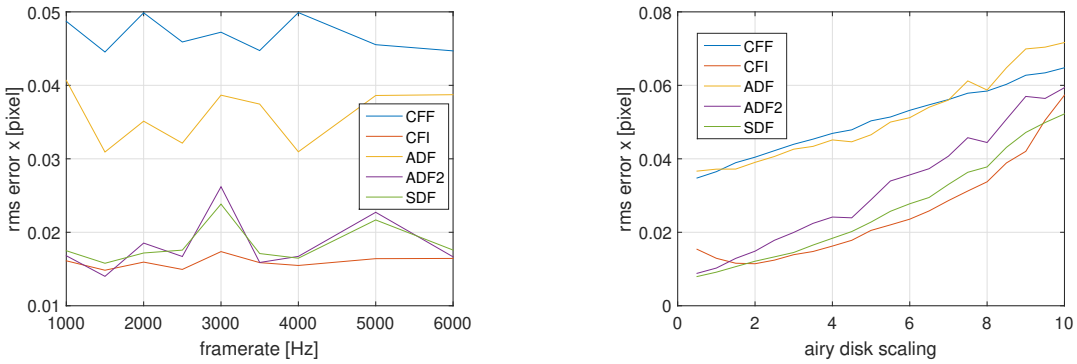

(a) Framerate variation.

(b) Airy disk diameter variation.

Figure 4.9: AO parameter variations with motion-blur (4).

only, but the correlation is to our best knowledge not completely understood. Most interesting is that low-order AOs with large subapertures seem to be able to register motion-blur sufficiently, what cannot be expected from standard AOs with very small subapertures. The accuracy of blurred image registration depends on nearly all factors that are controllable in our simulations. One exception is the framerate, which is only valid as long as the CoG distance is the reference, instead of trace samples. Other factors do mostly reduce the accuracy, like noise, quantization, the Airy disk, contrast, and the strength of the input jitter. But contrast and quantization experience saturation, and the resistivity against noise is quite high in all methods. Hence, we focus on the sensitivities related to image sizes and blur-extents. The latter shows up on variations of the strength of the input jitter and the Airy disks diameter. Both develop steadily over the investigated value range. For this reason, we assume that blurring-parameters affect the accuracy in a way similar to a SNR, because they can be compensated for with an increase of the image size. This relation is not understood, and hence the registration of blur requires simulation. The diameter of the Airy disk cannot be arbitrarily adjusted in telescopes, but the extent of the motion-blur PSF can be handled via adjustment of the width of the boxcar-filter. This is possible by reducing the exposure time, which is the integral over the frequencies of the vibration. Hence, there is a trade-off between required photons per image and accuracy of the registration, which could be solved with the boxcar-filter. We have not investigated the accuracy in radial coordinates, but only in pixel. The radial accuracy might be increased with higher spatial sampling, which concurrently enlarges all blur kernels. This can be compensated for with larger images and a boxcar-filter, as is shown in the next section where we investigate the registration of arbitrary motion-blur on science cameras. We recall that minimization of the residuals at the AO does not necessarily eliminate the residuals on the science camera if NCPEs occur.

4.3 Registration of blur with fast science cameras

The last section has shown that the extents of the blur kernels reduce the accuracy of the registration of blur, and that this effect can be compensated for with increased image sizes. High-cadence spectro-polarimeters sample beyond the Rayleigh-criterion, what magnifies all blur kernels in the registered images. We simply use increased image sizes, in order to compensate for this effect. Our results have shown that another effect has to be investigated when registration of blur is performed with high-cadence cameras, which is the underestimation of the amplitudes via the boxcar-filter because the interesting question refers to the reconstruction of the image degradation. We expect that tip-tilt residuals can be measured without NCPEs on the science camera. This degradation depends on the discrete time series $x[n \times t_s]$ and $y[n \times t_s]$, and it is known that the application of the boxcar-filter for reconstruction requires Nyquist-sampling. Hence, we simulate a Nyquist sampling spectro-polarimeter first, and test the effect of aliasing afterwards while utilizing the Sunrise PSDs and FSP parameters.

FSP would spatially sample with 0.0278 arcsec/pixel on Sunrise, and its framerate in Phase II is 400 images per second. Its duty-cycle is well approximated with one, which has negative impacts on the blur-radii. In order to compensate for both blur-extents, we choose an image size of 100×100 pixel for registration. An overall RMS value of noise for FSP can be assumed only, and we set this value to $50e^-$ before quantization to 16 bit. Furthermore, we calculate a complete photon budget as is expected for Sunrise 3 [54]. Hence, we do not specify mean signals or contrast. We found good examples for the illustration of aliasing in the relation of FSP's framerate to the PSDs, but we also show a Nyquist sampled case. Section 4.3.1 investigates the latter case, in which a camera with 800 Hz frame ensures Nyquist sampling of the 2009 set. Section 4.3.2 tests FSPs framerate of 400 Hz on the 2009 PSDs, where we find significant aliasing that hinders the reconstruction with the boxcar-filter completely. Section 4.3.2 investigates FSP's framerate on the PSD set from Sunrise 2013, where an intermediate case can be found.

4.3.1 Registration of blur with a Nyquist sampling camera

The last chapters have shown that the reconstruction of the cameras trace requires Nyquist sampling of those PSDs, which define the temporal variation of the position between image and object. In this chapter, we register images at 800 Hz framerate, which is approximately the Nyquist frequency of the 2009 Jitter, and we cover said case in which a high-cadence scientific camera is used for the registration of short exposure images. The accuracy in this case is depicted in Figure 4.10.

Figure 4.10a shows the related error-curves. It can be seen that the CFF method is no suitable choice for this setting, in which larger shifts and heavy blur extents have to be handled. CFF shows a linear trend in the accuracy, as was measured before by Löfdahl

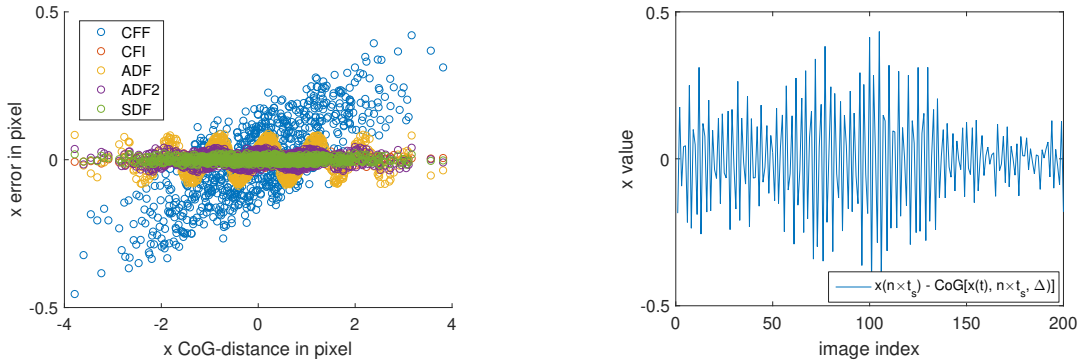

(a) Error-curves based on CoGs. **(b)** Error due to CoG calculation.

Figure 4.10: Registration and 1D trace reconstruction for a 800 Hz camera in the Sunrise 2009 setting.

on shifted images [32]. Furthermore, a stronger variation around this linear trend can be noticed, which is normally called random error. Hence, this method is neither accurate nor precise. The mean error of all curves is zero, and subpixel-error curves are visible again. The SDF method is most precise. Figure 4.10b depicts the distances between the correct samples $x[n \times t_s]$ and the CoGs related by the boxcar-filter, again. One can find that these distances are significant compared to errors from Figure 4.10a. Hence, the trace reconstruction with the boxcar-filter is mandatory.

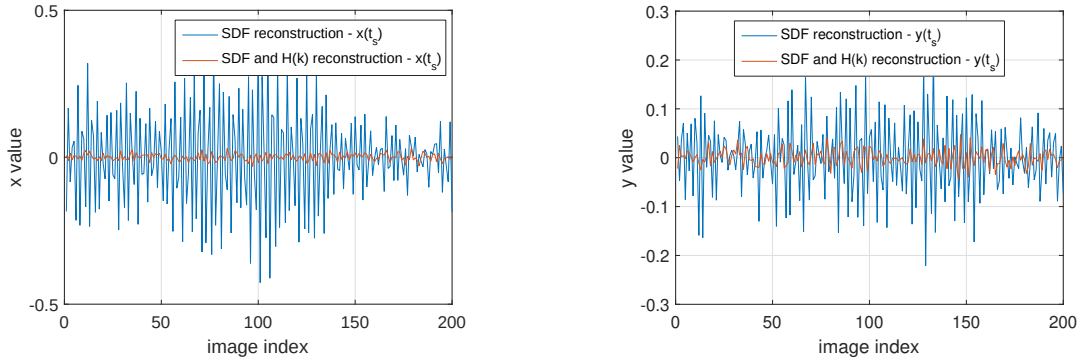

(a) Filter effect on the x-axis. **(b)** Filter effect on the y-axis.

Figure 4.11: Effect of the reconstruction filter without aliasing.

Next, we show a test in Figure 4.11. We reconstruct both discrete signals, $x[n \times t_s]$ in Figure 4.11a and $y[n \times t_s]$ in Figure 4.11b, from the SDF based registration results. We measure the distance between the registration results on each axis to the true sample that needs to be reconstructed. It can be seen in both figures that the slight error from

the image registration remains present, but does not hinder the successful application of the reconstruction filter. One has to be careful with this remaining error, since it hinders the reconstruction of the steady signal $x(t)$ via up-sampling of $x[n \times t_s]$, and similarly the reconstruction of $y(t)$.

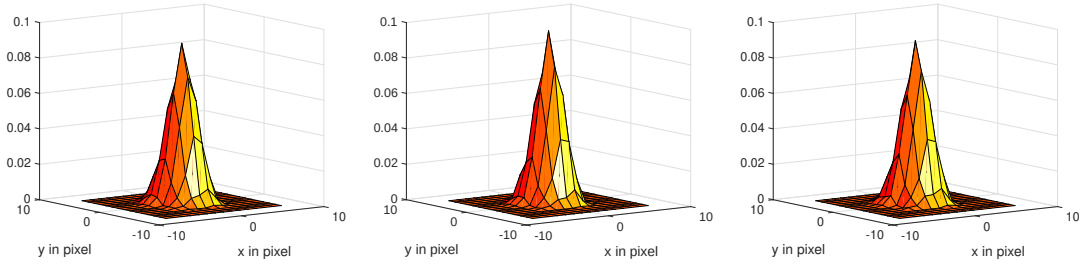

(a) True PSF **(b)** Registered PSF **(c)** H-reconstructed PSF

Figure 4.12: PSF reconstruction with a Nyquist-sampling camera on Sunrise 2009 (1).

We use both, the discrete reconstructed trace and the ground truth trace, for the generation of PSFs. These PSFs are depicted in Figure 4.12. The true PSF (Figure 4.12a) is generated from the ground truth input jitter. Figures 4.12b and 4.12c show the PSFs as generated from the registered values and their filter corrected equivalents, where no up-sampling of the traces is applied. All PSFs are generated with the method from Section 4.2.

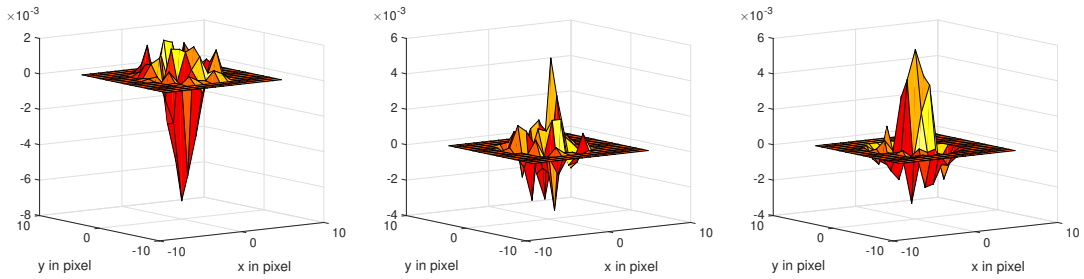

(a) True - registered **(b)** True - H reconstructed **(c)** Registered - H-reconstructed

Figure 4.13: PSF reconstruction with a Nyquist-sampling camera on Sunrise 2009 (2).

Figure 4.13 shows the difference PSFs related to Figure 4.12. One can find that the underestimation of amplitudes in the jitter leads to higher Strehl-ratios and radial underestimation in the PSF from the registered values. Hence, the related difference PSF has a negative Strehl-ratio and a positive halo (Figure 4.13a). The application of the filter solves exactly this problem, such that the resulting difference PSF is of less energy and a more random structure, which can be assumed to be caused by the inaccuracy

of the image registration (Figure 4.13b). Again, the difference PSF from registered and filter corrected values illustrates the same principle (Figure 4.13c).

We conclude this section with the finding that the PSF is reconstructable if the jitter was at least Nyquist sampled. This is quite obvious, because the requirement of Nyquist sampling is related to the reconstruction of the time series, which are interpolated to the PSFs. The reconstruction filtering is necessary in this case, because the ratio of exposure time to sampled frequencies is critical. The reconstruction of discrete signals is limited in accuracy due to errors in the image registration, and these errors hinder a reconstruction of steady input signals.

4.3.2 FSP on Sunrise 2009

In this section, we illustrate the performance of the trace reconstruction for FSP on Sunrise 2009, where the jitter is stronger and under-sampled on both axes at a framerate of 400 Hz (Figure 4.14). In this scenario, the problem is an increased underestimation of

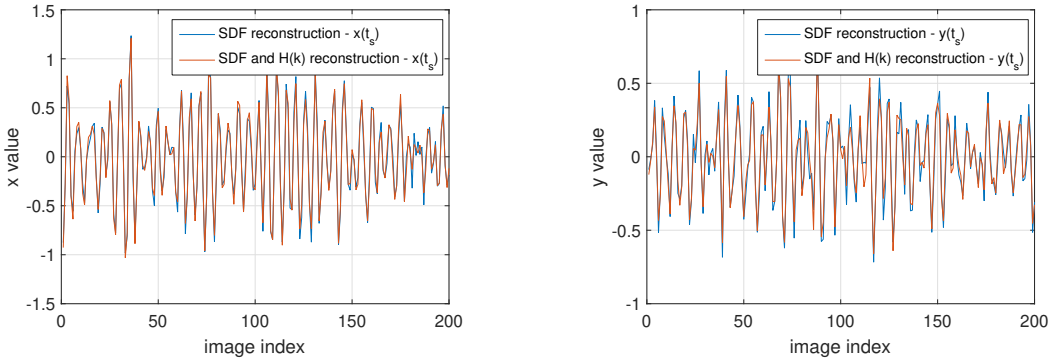

(a) Trace reconstruction x(t). **(b)** Trace reconstruction y(t).

Figure 4.14: Trace reconstruction for FSP in the Sunrise 2009 setting.

the jitters trace. Figures 4.14a and 4.14b show the relatively high underestimations of the traces on both axes, and that the application of the filter has only minor positive to negative effects if the signal is under-sampled and aliased.

Despite the underestimation, we use tuples $(x[n \times t_s], y[n \times t_s])$ for the interpolation of PSFs and show the resulting effects in Figure 4.15. It can be recognized via comparison of the PSFs themselves that the phase information is not completely restored, such that the form, and thus the statistical moments, differ between the reference and the reconstructions.

The difference PSFs in Figure 4.16 show that the power of the jitter was underestimated, since the Strehl ratios and halos are significantly pronounced. The first phenomenon, the incomplete knowledge about the phases of the PSF, cannot be overcome.

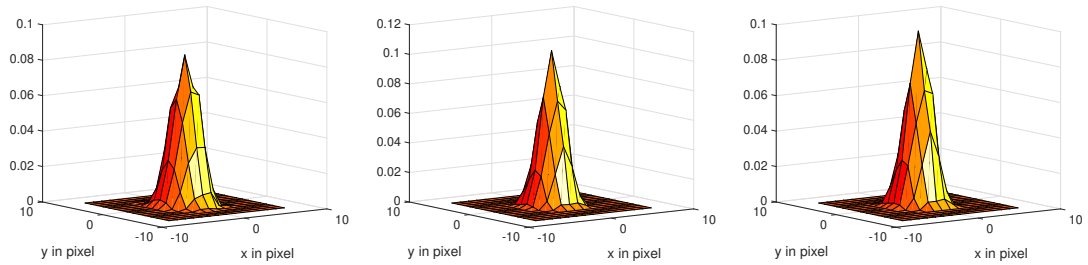

(a) True PSF. **(b)** Registered PSF. **(c)** H-reconstructed PSF.

Figure 4.15: PSF reconstruction with the FSP camera on Sunrise 2009 (1).

In contrast, the underestimation of the amplitude might be partially and blindly solved if one applies a radial scaling to the PSFs. This can be done by multiplying the trace tuples with scalars slightly bigger than one.

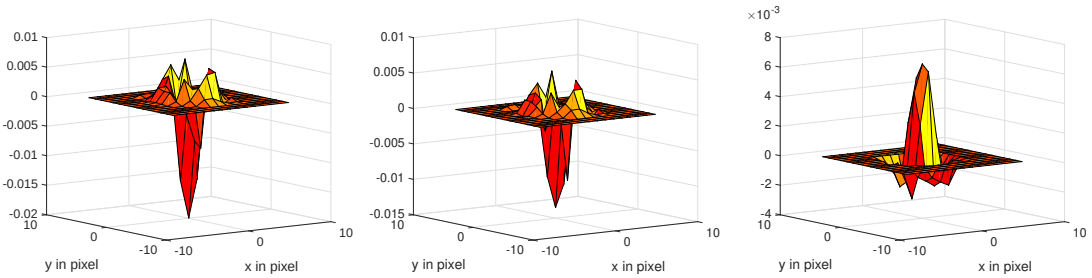

(a) True - registered. **(b)** True - H reconstructed. **(c)** Registered - H-reconstructed.

Figure 4.16: PSF reconstruction with the FSP camera on Sunrise 2009 (2).

We conclude this section with the simple finding that aliasing can hinder the reconstruction of the trace signals, which is quite unsurprising since the derivation of the reconstruction method has set even this requirement.

4.3.3 FSP on Sunrise 2013

Finally, we illustrate our simulations for a setting of FSP on Sunrise 2013. The fundamental PSDs are of less energy, and the azimuthal one is Nyquist-correctly sampled.

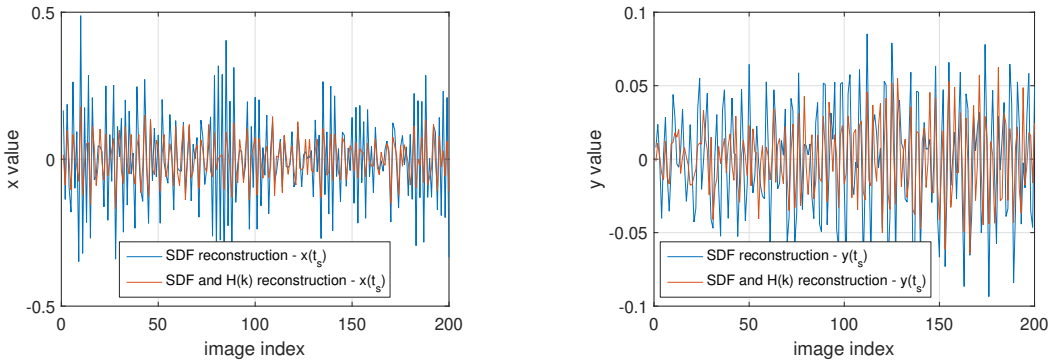

(a) Trace reconstruction x(t). **(b)** Trace reconstruction y(t).

Figure 4.17: Trace reconstruction for FSP in the Sunrise 2013 setting (1).

Figures 4.17a and 4.17b show that the errors are substantially decreased and the application of the filter has positive effects.

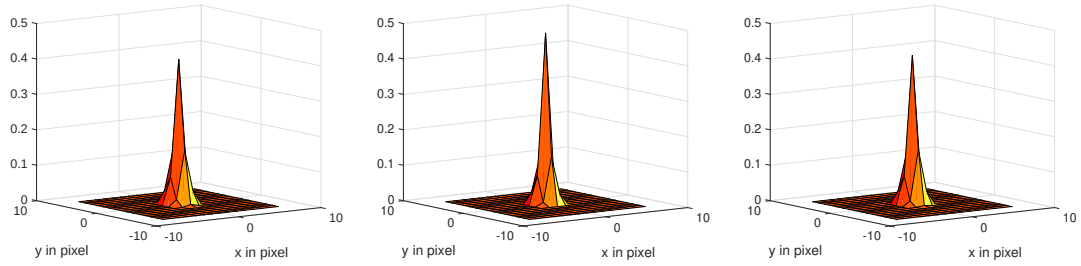

(a) True PSF. **(b)** Registered PSF. **(c)** H-reconstructed PSF.

Figure 4.18: PSF reconstruction with the FSP camera on Sunrise 2013 (1).

The same effect can be seen in the PSFs in Figure 4.18, where we show the true PSF, the registered one with a higher Strehl-ratio, and the filter reconstructed PSF.

Figure 4.19 shows the same difference PSFs again. All in all, one can find an intermediate case between heavily aliased and Nyquist sampled extrema.

We conclude this section by repeating our simple finding that the jitter has to be Nyquist sampled in order to reconstruct its discrete trace. The reconstruction of the

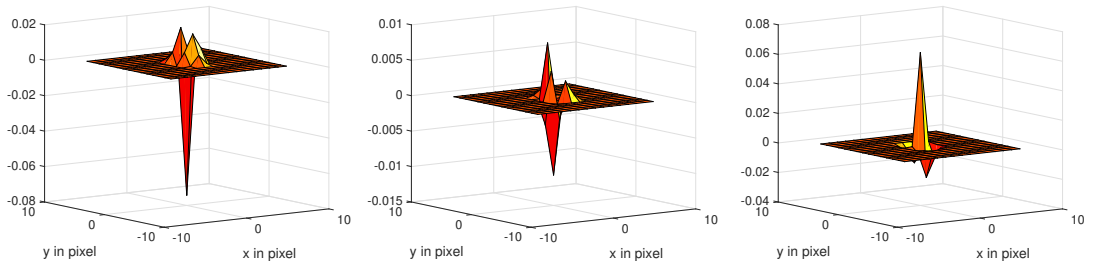

(a) True - registered. **(b)** True - H reconstructed. **(c)** Registered - H-reconstructed.

Figure 4.19: PSF reconstruction with the FSP camera on Sunrise 2013 (2).

continuous trace is never possible, since there are errors present induced by the image registration. But these errors do not hinder the application of the reconstruction filter to discrete samples. Violation of the Nyquist-sampling will result in aliasing, and hinder the application of the boxcar-filter more or less, depending on the energy in the aliased signal content.

4.4 Deconvolution results

The last sections have shown that the PSFs resulting from micro-vibrations can be measured, but also that these measurement are more or less error prone. Unfortunately, it was not possible to evaluate the accuracy with which the PSFs have to be known, so that they allow for sufficient data reduction. But it was cited that even partial knowledge of the PSFs can be used to increase the image quality. Hence, we show in Figure 4.20 the deconvolution results related to the test cases in the last sections.

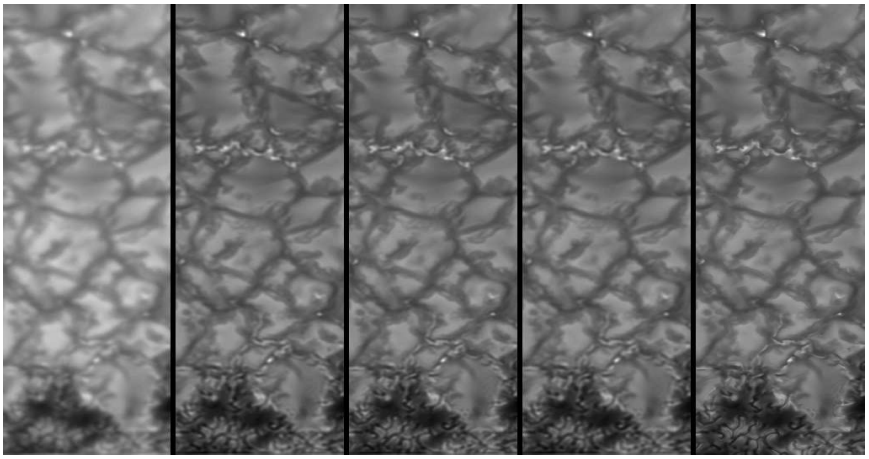

Figure 4.20: From the left to the right: The input image i, deconvolution results for 2009 at 400Hz, 2013 at 400Hz, and 2009 at 800 Hz, and the object o.

We choose the Richardson-Lucy deconvolution as in hybrid imaging, and utilize the version from MatLab as a black box. The results are generated with 20 iterations, under knowledge of the filter-corrected PSF from registration values, and without any further constraints. One can find that certain knowledge about the PSF easily allows for significant improvements in subjective image quality.

We conclude this chapter with a short summary of our findings. Several test-cases for the registration of blur were evaluated, and we used the Sunrise mission as example. A sensitivity analysis on the AO operation from the 2009 flight has shown that bigger subapertures than usual are mandatory for the registration of blur. This is necessary to compensate for random errors, which are induced by extents of the blur kernels in the images. Further results have illustrated that the registration of blur is not depending on the sampling frequency. In contrast, the reconstruction of the time series is. Hence, we investigated the impact of aliasing on the trace- and PSF-reconstruction. Unfortunately, it was not possible to argue with an absolute metric of goodness in image reconstruction, but we illustrated the goodness on difference PSFs. Blind deconvolution methods are

standard tools in astronomy, and further known to benefit from the knowledge of the PSF. Furthermore, the AO correction completely relies on this information. Thus, we just measured the signals which are fundamental for both corrections, and emphasize the critical aspects for this measurement. Firstly, the registration method needs to be verified, and we recommend difference-based methods from technical astronomy. Secondly, the reconstruction of the relative trace between object and image requires Nyquist sampling of the spectra of the motion. Thirdly, the size of the subaperture must be very large, we think 100×100 pixel is a good choice. Fourthly, the relations between extents of the blur kernels and accuracy of the image registration are not understood, and thus the registration of blur requires simulation. Finally, if there is a requirement for long exposure times, such that the related extent of the boxcar-filter becomes critical in relation to the sampled frequencies, a reconstruction with the boxcar-filter is necessary. Otherwise, the underestimation of the amplitudes can be suppressed with very short exposure times. This design strategy should be valid for both, AO and post-facto correction.

Next to this chapter, we like to conclude the first part of this thesis concerning micro-vibrations. We have argued for a strong focus on the abstraction layer of the image, because this image represents the net-value of the mission, and is fundamental for all steps of measurement and correction of the contained degradation. The micro-vibration induced degradation was identified as motion-blur, and the regarded image as the subaperture. Image registration methods from technical astronomy measure the distance between the CoGs of the motion-blur kernels accurately, as long as they are space-based and work on very large subapertures. The signal of interest for a reconstruction of the object is the motion trace, as defined by the image formation model. We propose an extension of this model to the temporal domain, in order to explain the boxcar-filter on measured time series. The argumentation for the temporal axis is known from the spatial axes of the sensor. Some implications of our work refer to the reconstruction of such time series, including the related requirement on Nyquist sampling. Open questions are related to an optimal interpolator in electro-optical systems, as well as the relation between extents of the blur kernels and accuracy of the image registration. Despite that, we think a practical application should be straight-forward, and the extension to several subapertures seems possible. Hence, we continue with a second motion-blur kernel that appears in scientific images, which is readout smear.

5 Computation of readout smear corrections for FSP

The last chapter has shown that FSP is not able to sample the vibrations from the previous Sunrise flights Nyquist-correctly. Despite that, several arguments can be found to measure the vibrations with this camera. For example, the method is non-invasive, i.e. if the camera fulfills scientific requirements, there is no additional drawback resulting from an additional registration of short exposure images. And it seems better to have partial knowledge of the PSFs than no knowledge, even if such knowledge only is used to learn from the measurements about the properties of the vibrations. However, we found another drawback occurring with the registration of blur via FSP. There is a second type of motion-blur involved, which is known as readout smear. FSP was introduced as framestore CCD based camera, which is operated without shutter. Hence, the image is further illuminated when it is shifted out of the light-sensitive area of the sensor. Such a relative motion between image and object causes motion-blur, as should be clear from the state-of-the-art in the second last chapter. But the fact that readout smear is motion-blur is more or less a finding within this work. Hence, there is a turning point in our argumentation. We start with a simple requirement [18] that readout smear has to be corrected for on-the-fly, if FSP should be candidate for a third flight. This requirement was set, because the post-facto correction of readout smear is not possible if in addition micro-vibrations occur during flight. But it is a nice starting point for an engineer, because it allows for rigorous application of the standard design flow. Hence, we developed this design straight forward, and discuss our finding afterwards under the new aspect. The development of the design is partitioned into optimizations of the algorithm in Section 5.1, and the implementation of a Field Programmable Gate Array (FPGA) based accelerator in Section 5.2. We develop this architecture model-based and proportionally show results. Finally, we interpret our findings in a way that the input requirement for the accelerator seems questionable under consideration of our own results. Hence, there is a turning point in our argumentation, which is based on the finding that readout smear is motion-blur.

5.1 Algorithms for post-facto correction

The request for an online correction of readout smear from images acquired with FSP directly leads to the application of the standard design flow, which is known to start with the analysis of the algorithm that needs to be implemented. This algorithm is given in [11] as the aperiodic case of readout smear correction. It can be seen as the most complex case, and it is relying on several more simple models. Hence, we start this section with

an introduction to the state-of-the-art, and present all algorithms for post-facto readout smear corrections in Section 5.1.1, before we show our optimizations in Section 5.1.2. The presented optimizations are directly related to the following implementation. Hence, we strongly focus on the reduction of instructions, parallelization, and approximate computing.

5.1.1 State-of-the-art

All algorithms for post-facto readout smear corrections are based on a simple problem formulation, which is directly related to the sensor architecture of framestore CCDs. We show an illustration related to the problem formulation in Figure 5.1.

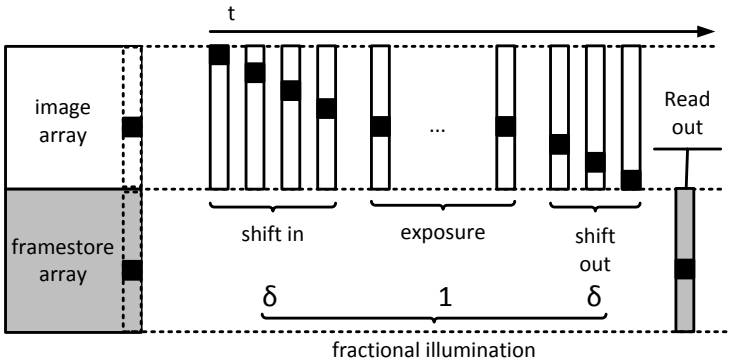

Figure 5.1: Problem formulation readout smear.

Framestore CCDs are standard sensors in imaging and defined by two regions. The light-sensitive image array generates electrical charge in the pixels, which is proportional to the incident photon flux during exposure time. After exposure time the collected charge is rapidly shifted through adjacent pixels into the framestore array, which is a light-shielded storage region that holds each frame for readout parallel to the exposure of the next frame. As can be seen in the figure, the framestore architecture enforces each pixel-information to be illuminated not only on the intended position, where it remains for the exposure time. Instead, the pixels zero-charge is shifted column-wise into this dedicated position in advance to the exposure, and similarly shifted out after exposure. Hence, each pixel is illuminated in all cells of the same row for a transfer time δ, which is normally given in fraction of the exposure time. These errors can be post-facto corrected, what is accepted in scientific experiments for several reasons. The parallelization of readout and exposure yields very high framerates, which incidentally exceed the possibilities of mechanical shutters only. The transfer of the electrical charge through adjacent pixels offers high fill-factors of pixels by avoiding additional resources for frame transfer, e.g. interline structures. Several hardware solutions seem applicable in order to reduce the smearing, but this would require additional sensor area and reduce advantages from framestore architectures. Hence, there is the post-facto correction in

scientific applications [55], such as particle image velocimetry [56] or high-cadence spectroscopy [11]. But different conditions require the application of different algorithms, which are summarized next.

5.1.1.1 Standard case

Most fundamental is the algorithm for the standard operation mode [57], in which the scene is assumed to be constant. This model can be described with Figure 5.1. Each column in the framestore array is referred to by the vector S, and it contains the true column Y of the scene plus the additional smear information. The relation of both, the smeared and the unsmeared column, is described with equation (5.1), where $i \in [0 : N-1]$ is the index of the pixels in the column.

$$S = MY : \begin{pmatrix} S_0 \\ S_1 \\ \vdots \\ S_{N-1} \end{pmatrix} = \begin{bmatrix} 1 & \delta & \dots & \delta \\ \delta & 1 & \dots & \delta \\ \vdots & \vdots & \ddots & \vdots \\ \delta & \delta & \dots & 1 \end{bmatrix} \begin{pmatrix} Y_0 \\ Y_1 \\ \vdots \\ Y_{N-1} \end{pmatrix} \tag{5.1}$$

As can be seen the matrix M is circulant, containing the sum of an identity matrix, and both, one upper and one lower triangular matrix only consisting of δ-values. Each pixels value S_i of a smeared column relies on 3 types of addends. The identity matrix describes the addend that comes from the true values Y_i of the unsmeared image, which is related to the exposure time. This is the signal of interest, and needs to be reconstructed. The addends resulting from the lower triangular matrix stem from the shift-out process after exposure, where all pixels with higher indices $j > i$ add to the charge of Y_i for a time related to δ. The same occurs before exposure time, when an empty charge is shifted into position Y_i during the shift out sequence of the previous exposed image. Each pixel j with $j < i$ adds a defined amount of charge to the signal. This amount of charge is related again to both, the fractional shifting time and the illumination at Y_j.

It is denoted in [57] that M is circulant and in general invertible. It is further stated that this property allows for a Fourier description of M. The Fourier description of M has a DC-component slightly bigger than one, which is explained with the additional illumination of the smeared photo. All other components of the transformed matrix consist of the entry $1 - \delta$. This Fourier description is used for a frequency analysis only. The correction of readout smear is denoted in the signal domain as:

$$Y = M^{-1}S. \tag{5.2}$$

5.1.1.2 Charge flush and reverse clocking

The case of charge flush and reverse clocking was introduced in [57] and [58]. A charge flush operation connects all pixels to ground before exposure time, so that the upper triangular matrix in M only contains zero entries. Hence, the charge flush eliminates

the error resulting from the shift-in via clearing of the pixels. In contrast, the lower triangular matrix in M remains consisting of δ-values due to shift-out. This error cannot be eliminated, because a charge flush after exposure would destroy the image itself. But the goal of this method is to reducing M to a lower triangular shape, such that the correction can be performed in running calculations. A second method is known, which enforces M in a similar lower triangular shape. This method is reverse clocking, and describes a shift-in of zeros from the direction of the storage region. This also sets the upper triangular part of M to zero, but the influence of the shift-in is then equal to the one of the shift-out. Thus, the lower triangular part of M is multiplied by 2. The resulting equation for both, the charge flush and the reverse clocking, is:

$$\begin{pmatrix} S_0 \\ S_1 \\ \vdots \\ S_{N-1} \end{pmatrix} = \begin{bmatrix} 1 & 0 & \dots & 0 \\ t*\delta & 1 & \dots & 0 \\ \vdots & \vdots & \ddots & \vdots \\ t*\delta & t*\delta & \dots & 1 \end{bmatrix} \begin{pmatrix} Y_0 \\ Y_1 \\ \vdots \\ Y_{N-1} \end{pmatrix}, \quad t \in [1,2], \tag{5.3}$$

with $t = 1$ for charge flush and $t = 2$ for reverse clocking. As can be seen, the matrix M is no longer circulant but of the more general type of a Toeplitz matrix, because it consists of constant diagonal elements instead of shifted version of rows or columns. Y can be solved in a fast running calculation from index $i = 0$ upwards. It is stated in [57] that the frequency decomposition is not straight forward.

5.1.1.3 Periodic case

The periodic case [11] is a smearing model which accounts for scenes that periodically vary between successive images. It was developed for FSP in ground-based observations. A polarimetric modulator periodically multiplexes four modulation states of a constant object. Its switching is synchronized with the unshuttered FSP camera, whereby the scene switching is located between exposure time and transfer time. It can be seen

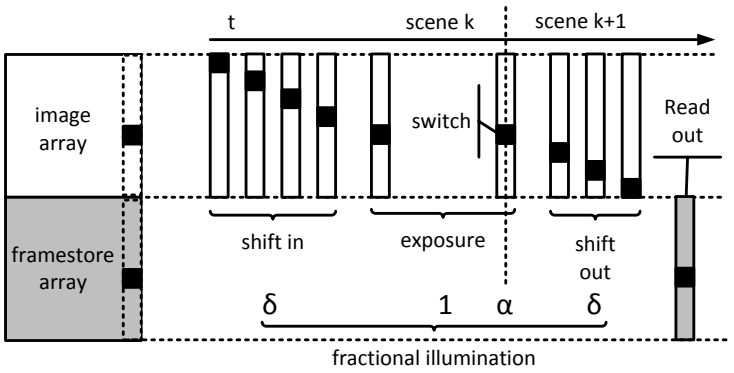

Figure 5.2: Readout smear with variable scene condition.

in Figure 5.2 that two variables are introduced in the smearing model, which is the index for the periodic scene k, and the switching time α. Four polarization states are described with $k = 4$, and we simply understand this as four different scenes, which are repetitively photographed in a periodic sequence. In application, a certain number of images are normally acquired for each k, and accumulated channel-wise. The switching between two consecutive scenes is not performed instantly, but requires a certain time. This switching is modeled with temporal symmetry, and the parameter describing the required time for this switching is α. The resulting model for one smeared column S^k with index k is given as:

$$\begin{aligned} S^k =& AY^k + BY^{k+1}, \\ A = &\begin{bmatrix} 1+\alpha & \delta_1 & \dots & \delta_1 \\ 0 & 1+\alpha & \dots & \delta_1 \\ \vdots & \vdots & \ddots & \vdots \\ 0 & 0 & \dots & 1+\alpha \end{bmatrix}, B = \begin{bmatrix} \alpha & 0 & \dots & 0 \\ \delta_2 & \alpha & \dots & 0 \\ \vdots & \vdots & \ddots & \vdots \\ \delta_2 & \delta_2 & \dots & \alpha \end{bmatrix}; \end{aligned} \tag{5.4}$$

In equation (5.4), the scene index k is assumed to appear periodically with the period K. S^k depends on the unsmeared column Y^k, where the influence of Y^k on S^k again has three types of addends. The upper triangular matrix in A consists of δ_1-values. These values result from the illumination due to the shift in transfer, and depend on the actual scene of the image as A connects the unsmeared column with the same scene index. Next, the true pixel values are added via one-elements on the main diagonal of A. The main diagonal of A also contains α parameters, which refer to the switching time and describe the fraction of the exposure time that is needed by the modulator to change the scene. After the modulation is changed to the following image-column Y^{k+1}, the shift out transfer is started. Hence, B connects S^k to Y^{k+1}, which contains the lower triangular matrix that is missing in A. Vice versa, B also misses the upper triangular part from A. The symmetric switching results in the appearance of α-parameters on the main diagonal of B. The assumption of periodicity is that image $k + K - 1$ always equals image k, so that the error description via the block-circulant matrix M can be written as equation (5.5):

$$S = MY: \quad \begin{pmatrix} S^0 \\ S^1 \\ \vdots \\ S^{K-1} \end{pmatrix} = \begin{bmatrix} A & B & \dots & 0 \\ 0 & A & \dots & 0 \\ \vdots & \vdots & \ddots & \vdots \\ B & 0 & \dots & A \end{bmatrix} \begin{pmatrix} Y^0 \\ Y^1 \\ \vdots \\ Y^{K-1} \end{pmatrix} \tag{5.5}$$

Then, the inversion of M allows for a calculation of all unsmeared columns within one period K.

5.1.1.4 Aperiodic case

The model for aperiodic illumination was introduced in [11] as well. This case covers circumstances in which the periodic scene condition is violated, i.e. only a burst of

images is investigated without periodicity constraints, such that each image in the burst has its own scene. In this case, the length of the image burst is denoted with K, and the general solution for one unsmeared column is given with equation (5.6):

$$Y^k = \sum_{j=1}^{K-k-j} H^{K-k-j} A^{-1} S^{K-j} + H^K Y^K, \;\; H^K = (-A^{-1}B)^K. \tag{5.6}$$

Furthermore, a highly damped homogeneous term of H^K was found, which allows to cut off the term $H^K Y^K$ from equation (5.6). The aperiodic case is the best applicable method for online smear correction in a jittered environment [18]. Hence, it is requested to implement an on-the-fly correction for FSP in phase II, which implements the functionality of equation (5.6). It can be seen that each column in each image depends on all of its successors with indices j. This is quite challenging for an image size of 1024×1024 pixel, at 400 Hz framerate, and acquisition times of several hours. Hence, we continue in the next section with the optimization of this algorithm.

5.1.2 Optimized algorithms

A short analysis of equation (5.6) shows three problems. Firstly, there is the quadratic complexity inferred by the matrix-vector multiplication. Secondly, each corrected column depends on all of its successors. Finally, equation (5.6) is not optimized for parallelization. Hence, we work towards an optimized computation of equation (5.6) in this section. We identify the standard case and the periodic case of readout smear correction as convolution operations, which can be calculated fast (Section 5.1.2.1). Section 5.1.2.2 utilizes the case of charge flush and reverse clocking operations for the derivation of parallel and fast computations. Finally, we cut the depth in the correction of the aperiodic case, and approximate the aperiodic case with the periodic one, which leads to algorithms that can be implemented more efficiently (Section 5.1.2.3). We denote two algorithms for a later comparison. Both algorithms work with the said approximation, but are furthermore mathematically equivalent to equation (5.6). Hence, we conclude with a software test on these approximation in Section 5.1.2.4.

5.1.2.1 Fast computation

The standard case in equation (5.1) was introduced in [57], where it was concluded that M has a transfer function. The DC-component is larger than one, and all other entries in this transform of M are slightly smaller. Hence, there is no cut-off frequency in M. Furthermore, the knowledge of M normally is very precise, such that the application of M as reconstruction filter is possible. This can be referred to as Fourier quotient method in the field of image deconvolution [59]. Formally, we find that the inverse M^{-1} of a circulant matrix M is circulant again (if M is invertible) [60]. It is either possible to derive the transfer function for M^{-1} similar to the one of M as in [57], or one can use the fact that circulant matrices have transfer functions in general, which allow to calculate a matrix vector multiplication with a circulant matrix as a convolution [61]:

$$Y = M^{-1}S = M^{-1}[:,1] * S = \mathcal{F}^{-1}(\mathcal{F}(M^{-1}[:,1]) \circ \mathcal{F}(S)) \tag{5.7}$$

The matrix vector multiplication equals a convolution ($*$) of the first column of M^{-1}, written as $M^{-1}[:,1]$, with S, and hence can be calculated via Fourier transforms and element-wise multiplication. $M^{-1}[:,1]$ can be seen as the transfer function of the smear correction. A Fast Fourier Transform (FFT) based solution is known to reduce the complexity of the matrix vector multiplications from $\mathcal{O}(n^2)$ to $\mathcal{O}(n \log n)$, if the vector size is a power of 2.

The periodic case can be calculated similarly, if one finds that the matrix M in equation (5.5) is circulant for $\delta_1 = \delta_2$, which is valid for normal operation.

5.1.2.2 Parallel computation

The correction of images acquired via charge flush and reverse clocking operations can be performed by running calculations [57]. Such computation is of complexity $\mathcal{O}(n)$ and cannot be outperformed via transform based operations. Despite that, we have investigated such calculations and found transform based solutions for equation (5.3). For charge flush and reverse clocking operations the matrix M is no longer circulant, but of the more general type of a Toeplitz matrix that is furthermore lower triangular. The inverse of a lower triangular Toeplitz matrix again is a lower triangular Toeplitz matrix, if it exists [60]. The Toeplitz matrix M^{-1} can be extended to a circulant matrix M_{ext} to solve Y [61]. It is also possible to extend M to the circulant matrix M_{ext} before its inversion, in order to calculate Y as:

$$\begin{aligned}
\begin{pmatrix} Y \\ Z \end{pmatrix} =& M_{ext}^{-1} \begin{pmatrix} S \\ O \end{pmatrix}, \\
M_{ext} =& \left[\begin{array}{cccc|cccc}
1 & 0 & \dots & 0 & t*\delta & t*\delta & \dots & t*\delta \\
t*\delta & 1 & \dots & 0 & 0 & t*\delta & \dots & t*\delta \\
\vdots & \vdots & \ddots & \vdots & \vdots & \vdots & \ddots & \vdots \\
t*\delta & t*\delta & \dots & 1 & 0 & 0 & \dots & t*\delta \\
\hline
t*\delta & t*\delta & \dots & t*\delta & 1 & 0 & \dots & 0 \\
0 & t*\delta & \dots & t*\delta & t*\delta & 1 & \dots & 0 \\
\vdots & \vdots & \ddots & \vdots & \vdots & \vdots & \ddots & \vdots \\
0 & 0 & 0 & 0 & t*\delta & t*\delta & \dots & 1
\end{array}\right]
\end{aligned} \tag{5.8}$$

The extension of M is done by appending circulantly repetitive diagonal elements until the extended matrix reaches at least size $(2N-1)^2$ and becomes circulant. The vector S is extended with zeros (O) to the corresponding size, so that Y can be calculated similar as in equation (5.7). The vector Z is thereby discarded. Same calculation is possible if M^{-1} and S are extended to a size of $2^l > 2N-1,\ l \in \mathbf{N}$, so that the transforms in equation (5.7) can be calculated fast. This makes no sense in the charge flush and

reverse clocking mode, but a circulant matrix can be extended similarly in order to use a fast transform for the standard or the periodic case. Furthermore, if a circulant matrix is split into square blocks, these blocks are of the type of Toeplitz matrices and can be extended in order to allow for a computation that is parallel and fast. This is of special interest for longer or concatenated columns as in the periodic case, because the length of the transforms can be limited independently of the periodicity K. Such parallelization can be reasonable for implementations in parallel architectures, and used to reduce clocking frequencies and thus power consumption. Hence, we can use this method for buying parallelization at the cost of twice the computations.

5.1.2.3 Approximate computation

The last smear model to be discussed is the aperiodic case from equation (5.6), which converges the smeared column rapidly towards a unsmeared one the more temporally distant columns are used for correction. This effect was studied in [11], and can be explained via the damping property of H^K. Despite this damping property, all successors of one image are used for its correction in [11]. It was found that images at the end of the series are then corrected worse than previous ones. We use this damping property in order to respect only a few smeared successors of the smeared column S^K for its correction. The application of such a depth of correction n results in:

$$Y^k \approx \sum_{j=0}^{n} H^j A^{-1} S^{k+j} \tag{5.9}$$

As can be seen in equation (5.9), the length of the series is no longer respected and the depth of correction is a parameter. We keep the matrices $H^j A^{-1}$ in the correction term, while knowing that the influence of smeared columns S^{k+j} on the true column Y^k decreases with increasing j. Furthermore, matrix properties [60] of $H^j A^{-1}$ can be investigated, in order to work towards a fast computation of equation (5.9). The inverse matrix A^{-1} is upper triangular Toeplitz if it exists, because A is upper triangular Toeplitz. Unfortunately, the product of A^{-1} and the lower triangular Toeplitz matrix B is not of a special type in general. Hence, we investigate other strategies and find the periodic case a good approximation as well. Given a correction depth n the smeared column S^k is formulated via the periodic case for n modulation states:

$$S \approx MY: \quad \begin{pmatrix} S^k \\ S^{k+1} \\ \vdots \\ S^{k+n} \end{pmatrix} \approx \begin{bmatrix} A & B & \dots & 0 \\ 0 & A & \dots & 0 \\ \vdots & \vdots & \ddots & \vdots \\ B & 0 & \dots & A \end{bmatrix} \begin{pmatrix} Y^k \\ Y^{k+1} \\ \vdots \\ Y^{k+n} \end{pmatrix} \tag{5.10}$$

The matrix M is now circulant and invertible, but an error for the calculation of S^{k+n} is introduced due to the periodicity. Other smeared columns are formulated correctly. Hence, the unsmeared column Y^k is corrected via S^k and its successors, which are correctly formulated up to the depth $n-1$. We like to explain this step in relation

to equation (5.9). In this equation, the cut-off is quite clear, since we simply set all smeared columns S^{k+j} equal to zero, if j exceeds n. This is basically the approximation, which is possible due to the damping. But there is a certain distance between the zero column that takes the place of the one which is cut off. Polarimetric images are of very low contrast, and their typical average value is somewhere around the center of the bit-depth of the sensor. Hence, it can be assumed that the distance between a zero-column O and the neglected column S^{k+n} is bigger than the distance between two consecutive columns S^{k+j}. Thus, we introduce a slighter error in the last column of equation (5.10), which is suppressed with the depth of correction n. We subsume that the column $k+n$ only is inserted in order to make the matrix M circulant, but is cut-off next. In the same step, we invert M and apply equation (5.7), in order to derive a fast and approximate computation for the aperiodic case:

$$\begin{pmatrix} Y^k \\ Z \\ Z \\ \vdots \\ Z \end{pmatrix} \approx \mathcal{F}^{-1}\left(\mathcal{F}(M^{-1}[:,1]) \circ \mathcal{F}(\begin{pmatrix} S^k \\ S^{k+1} \\ \vdots \\ S^{k+n-1} \\ O \end{pmatrix})\right) \tag{5.11}$$

The matrix M from equation (5.10) and its inverse are circulant, such that a convolution of the vector S with the first column of M^{-1} computes Y. The periodic approximation yields good results for Y^k and increasing worse ones for corrected columns with higher time-indices. Thus, only the column Y^k is corrected in dependency of n smeared columns. The other columns are not corrected, and hence discarded and marked with Z. S^{k+n} was falsely calculated in equation (5.10) and is therefore set to zero as denoted with O. We interpret equation (5.11) as a fast and approximate version of the aperiodic readout smear correction. But this algorithm is not suited best for parallelization. This is due to the fact, that the correction is performed in the Fourier domain. The utilization of a Fast Fourier Transform (FFT) normally relies on the application of Intellectual Property (IP), which does not necessarily support the split of one into several parallel transforms. Hence, we call equation (5.11) the sequential variant of the targeted algorithm, and we recall that the length of Y has to be an integer power of 2 in order to allow for fast FFTs.

The calculation of the aperiodic case can be further parallelized, if the circulant matrix is split into several square Toeplitz matrices T^{k+j} of column-size (Section 5.1.2.2). One can write M^{-1} in a simplified block form, where irrelevant blocks are again denoted with Z:

$$\begin{pmatrix} Y^k \\ Z \\ \vdots \\ Z \\ Z \end{pmatrix} \approx \begin{bmatrix} T^k & T^{k+1} & \dots & T^{k+n-1} & Z \\ Z & Z & \dots & Z & Z \\ \vdots & \vdots & \ddots & \vdots & \vdots \\ Z & Z & \dots & Z & Z \\ Z & Z & \dots & Z & Z \end{bmatrix} \begin{pmatrix} S^k \\ S^{k+1} \\ \vdots \\ S^{k+n-1} \\ O \end{pmatrix} \tag{5.12}$$

Equation (5.12) shows the inverse of M. Hence, the smeared columns are input, all blocks in the matrix are not necessarily zero entries, and the result is the vector Y. Still,

only Y^k is well approximated. For this reason, other columns in the Y vector are denoted with Z, as well as the related, unused blocks in M^{-1}. We find that we can denote Y^k as the sum of products, which consist of Toeplitz matrices T^{k+j} times vectors of smeared columns S^{k+j}. Hence, we denote this sum, and apply the extension of Toeplitz matrices to circulant ones in the same step.

$$\begin{pmatrix} Y^k \\ Z \end{pmatrix} \approx \mathcal{F}^{-1}\left(\sum_{j=0}^{n-1} \mathcal{F}(T_{ext}^{k+j}[:,1]) \circ \mathcal{F}(\begin{pmatrix} S^{k+j} \\ O \end{pmatrix}) \right) \tag{5.13}$$

The Toeplitz matrices are extended to circular ones T_{ext} of an integer power of 2 (compare equation (5.8)). The first row of each T_{ext}^{k+j} is Fourier transformed and multiplied element-wise with the Fourier transform of S^{k+j}, where S^{k+j} is extended with zeros (O) to the corresponding size of the matrices. The inverse transform of the sum of the convolutions then contains the corrected vector Y^k at the position $[0 : N-1]$. The addends of the sum can be computed in parallel. Equation (5.13) should finally allow for a real-time correction of aperiodic readout smear in the FSP camera, as this algorithm is not only fast and approximate, but also massive parallel. Furthermore, the transform length does not scale with n, such that all depths of correction n can be calculated fast, if parallelization is performed related to images with columns that have an integer power of two pixels. We repeat that these features come at the cost of an increase of the computations compared to equation (5.11). This makes the comparison of both algorithms interesting for the design space exploration, where we call equation (5.13) the parallel variant of our algorithm. Hence, we continue with even this task in Section 5.2, but show some testing before.

5.1.2.4 Testing of the approximations

The last section has introduced a cut-off in the depth of correction n, and the approximation of the aperiodic case via the periodic one. These are the only changes that cannot be seen as mathematical equivalent to the verified algorithms from [11]. Hence, we test even these differences, and use sets of synthetically degraded images only. Parameters for smear generation and correction stem from the FSP camera in its phase I implementation, because parameters for the phase II implementation are not available. These available parameters from hardware measurements are given in Table 5.1 and were measured at 800 Hz framerate [18].

Table 5.1: Parameters for smear correction in the FSP camera in phase I [18].

transfer parameter δ	switching parameter α
0.00038255746	0.038862980

The readout smear was always applied to sets of 10 images of 512×512 pixels, resulting in 9 aperiodically smeared ones. All images were previously scaled to 16 bit depth, but only 14 bits contain image information in order to avoid overruns in bit-depth due to the additive smear. We like to show the related images before the measurements on

the correction. Figure 5.3 shows the first two images of one series (5.3a and 5.3b), and

(a) image $k = 0$ **(b)** image $k = 1$ **(c)** smear of image $k = 0$

Figure 5.3: Computed smear information from input images.

the resulting smear of the first image (5.3c). A degraded image is the sum of the shown smear and the first image. The smear information contains not only the vertical stripes that are typical for the standard case, but furthermore copies of both images that are resulting from the switching procedure. This is simply explained with the formula which is used for smear generation. More interesting is how a step-wise correction reduces the smear information in one image. This is depicted in the difference images in Figure 5.4, which show the remaining smear after n steps of aperiodic corrections. If one frame is

(a) smear after $n = 1$ **(b)** smear after $n = 2$ **(c)** smear after $n = 4$

Figure 5.4: Difference images after step-wise correction of aperiodic smear.

utilized for correction of image $k = 0$, the resulting difference is the smear which mainly contains information from image $k = 1$ (Figure 5.4a). One further correction step makes the next image (Lenna) partially visible in the difference (Figure 5.4b), but the vertical stripes from the transfer process become dominant with higher depth of correction (Figure 5.4c). The difference images are scaled and the absolute values of the difference images decrease with n.

The development of both, the maximum absolute value and the RMS value of these difference images, is illustrated in Figure 5.5. The image $k = 0$ was corrected via equation (5.13) up to a depth of correction n. Both metrics are steadily reduced with increasing n.

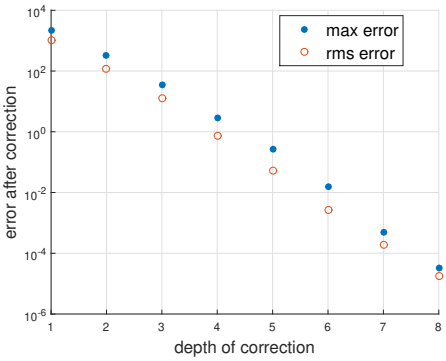

Figure 5.5: Rms error and maximum absolute error of image $k = 0$ after aperiodic correction depending on the depth of correction n.

It can be seen that smear-information in a coarsely corrected shot is significant (n=1), but a correction depth of approximately $n = 6$ is sufficient to suppress the smear to values that cannot be measured in uint16 data-format. However, the depth of correction has to be determined analytically for new setups, even if results for one specific setup are commonly stable.

Next, we isolate the influence of the error due to the wrong assumption of periodicity. We use a periodic correction via equation (5.10) on a set of 10 aperiodically smeared images. Results are shown in Figure 5.6. The assumption that image $k = 9$ equals image $k = 0$ leads to significant RMS errors at higher indices, but to irrelevant small ones at lower indices. Similarly as before, this effect is caused by the damping property in the inverted matrix equations that was discovered in [11].

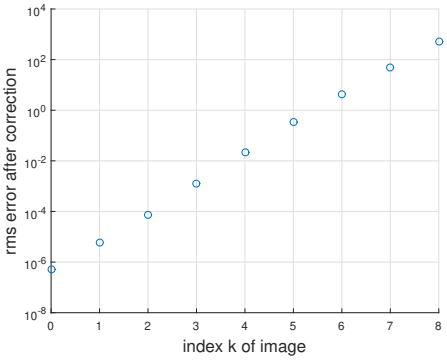

Figure 5.6: Rms error of image k after periodic correction of aperiodic smear.

Finally, we give a short conclusion on this section. We have neither significantly changed nor evaluated the verified algorithms from [11]. Instead, we subsumed the state-of-the-art and showed that interesting properties can be derived from each contribution, in order to work towards optimized computations. The standard case was finally

identified as motion-blur, whose kernel is very precisely known and has now cut-off frequency. This allowed for a correction based on direct filtering in the Fourier domain, which reduces the complexity of this algorithm. The same does account for the periodic case that is applied in ground-based observations with FSP, but the fundamental space contains several images. We derived a parallelization of such convolution operations from the charge flush and reverse clocking case, and we used the known damping property from the aperiodic case in order to allow for approximate computations. The understanding of the resulting corrections was illustrated on difference images and measured on metrics on them. We simply suppress all errors resulting from approximations via the damping property into regions that cannot be measured. The related depth of correction has to be determined analytically, but a pretty short window of frames seems to be sufficient. Hence, we proceed with exploring the developed sequential and parallel version in the design space.

5.2 Hardware-accelerated computation

The last section has shown that the choice of the algorithm is one interesting design space parameter. The sequential variant is only fast for certain depths of correction n and more difficult to parallelize, but will require less operations than the parallel version of the targeted algorithm. Hence, the depth of correction becomes interesting, since it might give hints for the choice of the algorithm. Thus, we discuss in Section 5.2.1 the design-space exploration and focus on the algorithms first. We determine the target platform as an FPGA development board, go into details of available IP-cores and system components, and conclude with an overall system architecture. Section 5.2.2 finally covers the implementation of this architecture. We do not go into details of the implementation, but show the relevant parts of the system, especially when certain optimizations are used for implementation. The development is model-based, which is due to the facts that the camera was not available for hardware testing, and the algorithms are verified such that they can be seen as ground truth. Hence, we show only some results in Section 5.2.3, but we mainly argue that readout smear should be interpreted as motion-blur in order to understand its relation to micro-vibrations.

5.2.1 Design space exploration

Most fundamental for a design space exploration is the evaluation of certain parameters that determine the choice of the algorithm, as was shown in the last section. But we introduced the algorithm independently of certain properties of the FSP camera. Hence, we depict these properties in Figure 5.7 as a start. As can be seen in this figure, we illustrate FSP's sensor layout and its operation in the aperiodic case. The functionality is the same as in the previous section, but it is operated on half-columns. This is, because the sensor is split into 2 independent hemispheres. Hence, the correction of smear is performed on 2048 half-columns with a length of 512 pixel each. It is further sketched in this figure that the readout direction of the half-columns is perpendicular to the direction

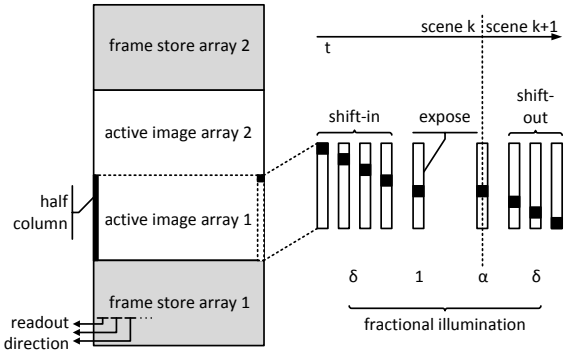

Figure 5.7: FSP's sensor layout with two hemispheres, half column, and readout direction.

of the frame transfer. For this reason, there is requirement to rotate the images by 90 degrees, in order to derive the required half-columns from the rows that have been read out.

The amount and the length of the half-columns can be used to estimate the performance of a readout smear correction in real time. Each half-column has to be corrected individually, and hence a high degree of parallelization can be obtained in every case. The instructions for the correction of the half-columns are always the same, such that all corrections can be executed in parallel on Single-Instruction-Multiple-Data architectures. A Graphic Processing Unit (GPU) would actually fit with respect to the amounts of shader units, but the power consumption is too high for autonomous missions since cooling in the stratosphere is problematic. The costs of a software-based solution can be estimated in terms of required multiply-add-instructions. We give a coarse worst case estimation relying on a correction in the intensity domain. As one correction step per half-column requires a matrix-vector multiplication of 512 data words, the intensity domain solution would compute at least $512^2 \cdot 400 \cdot 2048 \cdot n \cdot \mathrm{Ops}/s \approx 214 \cdot n \cdot \mathrm{GOps/s}$. Hence, a correction depth of $n = 5$ would require a Teraoperation per second in the intensity domain, or approximately several hundred Gigaoperations per second in the Fourier domain. We finally decided to target a Xilinx Virtex 7 FPGA, in order to avoid the cost for application specific integrated circuits on the one hand and the lower energy efficiency, need for hosts and peripherals, and design effort for accurate throughput with central processing units and GPUs on the other hand. We decided to use Xilinx technology, because all required licenses only are available in-house for this vendor, and the amount of operations per second determined the focus on the Virtex 7 series.

Fourier-based algorithms have to be used for optimization of chip area and power consumption, and the reuse of related IP is mandatory for avoiding overwhelming design efforts. Hence, we focus on the Xilinx Fast Fourier Transform v9.0 LogiCORE. This core offers several variants for implementation, especially as different data formats and implementation architectures are supported. The implementation architectures are automatically selected by default, depending on the chosen throughput requirements.

However, those are constant in our design and padding is not necessary as the input sequence length is always a power of 2, so our focus is primarily on the data formats. The relevant options are fixed-point and floating point formats, which both are limited to 32 bit width. The input data from FSP is 16 bit unsigned integer, which seems not sufficient for extensive multiplications in the transforms and the smear correction. Hence, we evaluate the degrees of freedom related to the data formats, and the depth of correction as argued before.

Based on this argumentation, first the average error of the MatLab Executable function is compared to MatLab's double precision FFT. Both is accomplished by extending the ground truth MatLab models, and monitoring average errors that result from different implementation variants.

A first test only compared all possible implementation variants of the FFT core, where the smear corrections are neglected. Results are shown in Figure 5.8. There is no sig-

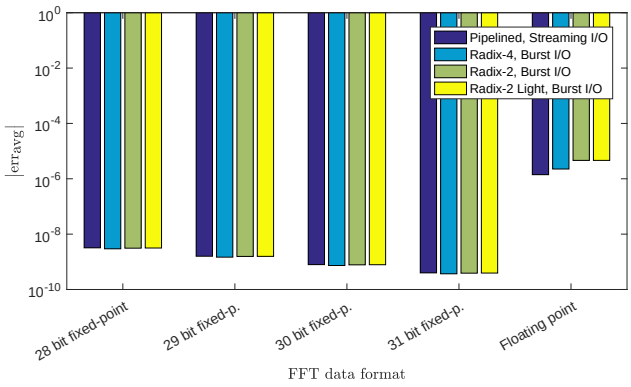

Figure 5.8: Average errors for different data formats and architectural options.

nificant variance in accuracy for all implementation variants that are supported by the IP core. But it can be seen that the single precision floating point implementation is outperformed by the fixed-point variants, and that the latter shows increasing accuracy with increasing bit-depth. This can be explained by the fact that floating point transforms are internally calculated as fixed-point, and simply additionally offer an automatic scaling for inputs with different exponents. Such different exponents are not present in our design, because the input data is always available in the uint16 value range as given by the camera. Hence, we decide to implement a fixed-point design with fixed scaling. It is both more accurate and of lower costs, but the maximization of the input width is advisable.

The results from Figure 5.8 are based on a pure evaluation of the FFT with uint16 data inputs. We continue evaluating the average errors in the complete smear correction algorithms, and vary several parameters. Three settings for data types are tested,

namely a single precision floating point model, a 31 bit fixed-point model, and a mixed model. The latter performs FFTs in 31 bit fixed-point and multiplication with correction vectors in single precision floating point. The results of the comparison are shown in Figure 5.9, and include variations in the depth of correction. These results are scaled

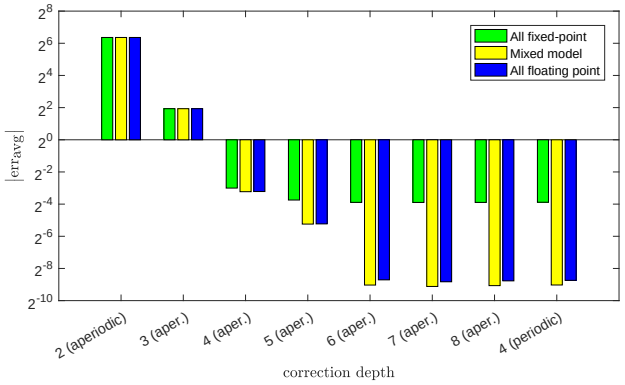

Figure 5.9: Average error of the smear correction in dependence on the correction depth and simulation model.

to the value range and the least significant bit of the uint16 data format. It can be seen that all models experience saturation in accuracy for a depth of correction of $n = 6$, and the interesting convergence against these optimum values starts at $n = 4$. Hence, a depth of correction in between should be sufficient to suppress all residual errors to a level in which they cannot be recognized in FSPs data format, especially since the least significant 3 bits are normally cut off because they only contain noise [18]. For comparison, the result for a periodic input sequence is shown as well. It can be seen as a lower bound for the achievable accuracy of a given implementation. Most interesting is a finding from [62]. This is the behavior of the mixed model, which outperforms not only the floating point variant but also the fixed-point only model. This can be explained by bigger changes in exponents that come along with the multiplication in the Fourier domain, but not with the transform alone. For the same reason, the fixed-point model now shows significantly less precision than the alternatives, in contrast to the results of the pure FFT comparison in Figure 5.8. For this reason, we continue our design using the mixed model, which is ideal regarding both precision and resource usage.

A previous finding was that the mixed model's accuracy increases with the width of the FFT data input. It is thus set to 32 bit in hardware. Similar to the data width, the twiddle factor width needs to be adjusted. Hence, we vary this width of the twiddle factor while monitoring the average error again, as is shown in Figure 5.10. A clear trend in accuracy improvements as well as a related cut-off can be seen. Hence, we decide to configure a twiddle factor width of 24 bit.

Based on the decision for a Virtex 7 chip, we subsume all identified parameters on the

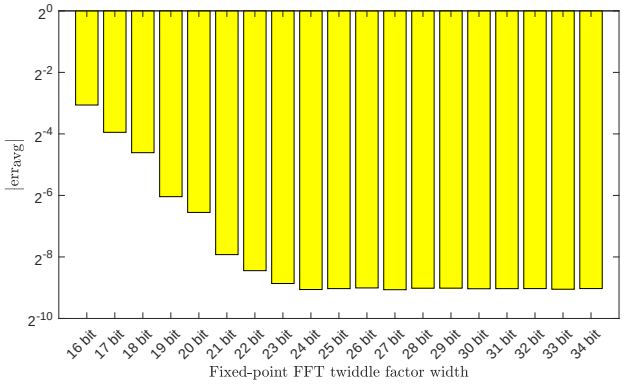

Figure 5.10: Average residual error in the mixed model in dependence on the fixed-point FFT twiddle factor width.

data formats in what we call mixed-model. Finally, we utilized the NetFPGA SUME board [63] for implementation, because it offers all required components, and in addition Quad Data Rate II+ Static Random Access Memory (QDR II+ SRAM). As usual in image processing on FPGAs, we identified memory bandwidth and capacity as the bottlenecks of our design. QDR II+ SRAM is easy to interface and allows to save design effort at cost of a few hundred Euro, which is cheap when the design is a single unit. Furthermore, the SUME offers 10 Gigabit Ethernet (10GE) which is required to interface the accelerator between camera and data storage. The net data rate in this stream can be calculated. Images are received with a net data rate of 400 images $\cdot$ 2 MB/image $\cdot$ 8 bit/byte $=$ 6.4 Gb/s. The image size of two Mega-Byte (MB) is further critical for image rotation, because a storage of $n \in [4:6]$ images cannot be accomplished on FPGA internal memory. It was found to be necessary to rotate the images by 90 degrees, as they have been read out in rows instead of columns.

We can identify 5 main tasks that have to be accomplished independent of the choice of the algorithm: Firstly, it is necessary to rotate the images, which requires external storage. Secondly, external storage also is required for parallelization, because several time instances of each half-columns are used for the correction of the half-column itself. Thirdly, each half column has to be transformed into the Fourier domain for each time instance. Fourthly, each time instance of each half-column has to be corrected for smearing. And finally, each corrected half column has to be back-transformed into the spatial domain.

Related to these five tasks, we found two main degrees of freedom that have to be explored. It was already described that we have to choose either the sequential variant or parallel variant of the algorithm. And the order of external buffering and Fourier transformation is a critical aspect in this design.

The finding of an adequate architecture is known to being no straight-forward task. Hence, we only give certain arguments that have direct impact on the final system design. Firstly, a Fourier transform before external buffering can only be applied to the parallel variant of the algorithm. That would reduce n forward transforms to one, but lead to additional costs of at least 4 MB input buffer for image-rotation. This buffer is very expensive on-chip, and an off-chip-buffer for rotation is needed anyway. Furthermore, storage of transformed real vectors costs either double the memory or requires calculations exploiting symmetry properties of the FFT. Hence, we think it makes sense to fix the external storage before the FFT task. Secondly, a Fourier transform after external storage can be applied to both algorithms. The sequential algorithm will require buffers between the memory and the FFT cores. This is due to the fact that the length of each transformed vector exceeds the length of a half-column. Hence, there is a second request on the critical resource memory, which comes from the sequential algorithm only. Finally, there are three additional arguments for the parallel algorithm: The sequential variant is only fast for $n = 4$, but the parallel variant is fast for each depth of correction. The parallel variant is easy to scale with n, because the length of the transforms remains constant and does not exceed the length of the half columns. Hence, a higher depth of correction leads to an extension of the pipeline in its parallel direction for the parallel variant, and not along the sequential direction of the pipeline as would be the case for the sequential variant. The parallel variant is only slightly more expensive in FFT computations than the sequential variant. All in all, we think there is good argumentation to fix both degrees of freedom as follows. We implement the parallel variant of the algorithm after buffering in external memory. This allows for implementing a fast calculation for each depth of correction, as well as for easier scaling of the depth of correction. The slight increase of required logic for the parallel variant is less expensive for us than the increased design effort for more sophisticated buffers necessary for the sequential one. Furthermore, we have found that the additional storage of 4 MB leads to more design complexity and misapplies scarce resources. Hence, we store the images in the intensity domain on external memory first, where they can be rotated and parallelized, and perform all processing steps in parallel afterwards. As will be shown later, the QDR II+ SRAM's capacity allows for an correction depth of $n = 7$, which is more than sufficient.

Foregoing findings lead to an overall system architecture as shown in Figure 5.11. Images are received in the 10GE subsystem. They are forwarded via a memory interface onto the QDR II+ SRAM modules, where they are rotated and parallelized. The readout of the frames is done in half-columns with a parallelization related to the depth of correction. The processing is divided into the steps of forward transforms, complex multiplications with correction values, and addition of the same half-columns from different time instances. The sum is finally back-transformed and transmitted via Ethernet again. In summary, the images are on-the-fly smear-corrected and rotated by 90 degrees.

We conclude this section with a short summary. Given the decision for an implementation on a Virtex 7 FPGA, we evaluated and fixed all data formats, decided for

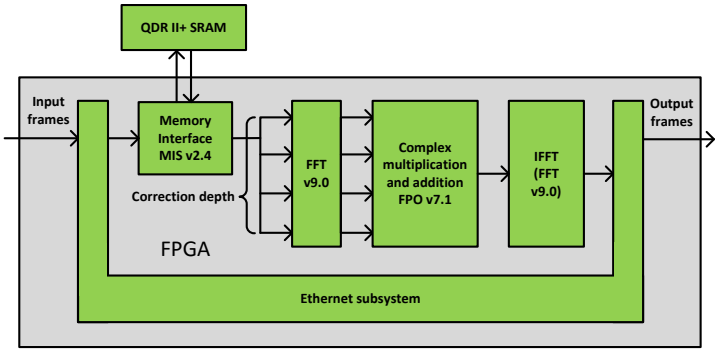

Figure 5.11: Block design resulting from the design space exploration.

a particular memory technology, argued for an algorithm, and determined the order of both. These decisions are neither independent of each other, nor is it possible to find an absolutely optimal design. But we argued that external memory is required, and further can be assigned with a dual use for image rotation and parallelization. Hence, it would make sense to map both functions on a single memory, what also determines the order of memory and transforms. Based on this decision, a sequential algorithm would require further memory for stream buffering, and the parallel variant is only slightly more expensive in computations, such that we implement the parallel algorithm after a single external memory. This external memory is bound to QDR II+ SRAM, because its cost are low compared to the design effort as long as we build a single unit. This implementation is presented in the next section.

5.2.2 Implementation

In the previous section, we derived a system architecture for the online computation of readout smear corrections for FSP on the NetFPGA SUME board, and configured all data formats for the FFT-cores. In this section, we continue describing the implementation of the related parts, which are the Ethernet subsystem, the memory interface, the calculation pipeline, and the parallelization with which the calculation is performed. We thereby set our focus on useful tricks that help to optimize the design under several aspects, for example fulfilling the on-the-fly requirement or reducing resources.

For the interfacing between MatLab and the Ethernet subsystem, we have extended our MatLab model with Java routines that implement universal datagram protocol sockets. On the FPGA side, the serial stream is handled by the Xilinx 10GE physical layer IP and a low latency medium access control from OpenCores [64]. The Ethernet interface of the used personal computer setup has limited the data rate of the complete test loop to 1Gb/s. Hence, only the functionality, but not the throughput can be proved model-based. Instead, an Ethernet traffic generator has been implemented in hardware in order to verify data rates in a later test setup (Figure 5.12). Such a test would

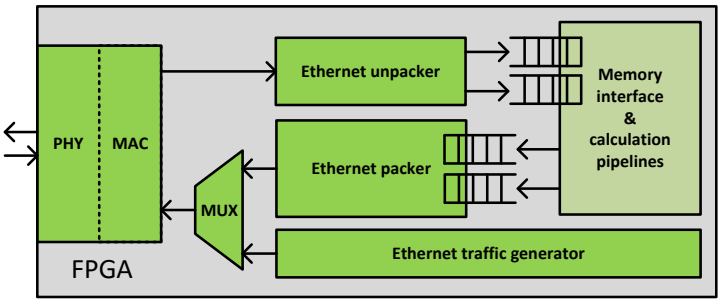

Figure 5.12: Block design of the Ethernet subsystem.

transmit dummy frames with calibrated framerate off-chip. An external loopback allows receiving the stream on-chip again and measure the data-rate.

The first module within a pipeline is the memory subsystem. A correction depth of $n = 4$ enforces a split of the data to two QDR II+ SRAM modules, and we simply split the data in relation to the frame store arrays, i.e. the hemispheres of the sensor. Both hemisphere-related memory modules are handled by a single memory interface, which has been generated using the Xilinx Memory Interface Generator. Each module has one dedicated read- and write-port for the access of a data word. We partition each data word into $8 \cdot 16$ bit net data neglecting error-correction code related overhead. Figure 5.13 shows the functional memory subsystem diagram for one hemisphere that consists of the memory, the interface, and related logic. The memory subsystem fulfills two tasks,

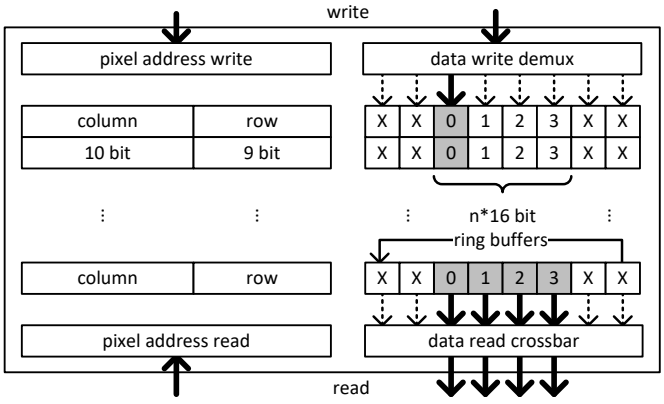

Figure 5.13: Functional memory subsystem for one hemisphere.

which are the rotation of the image and the parallelization of four time instances of each half-column. The Ethernet subsystem connects to the write port, and image rotation

is achieved by the write strategy: Only one pixel of time instance $k = 0$ is written to the memory of a hemisphere per cycle. Each pixel identified by its coordinates (x, y) is assigned to a fixed word in the memory. Each word in the memory is split into 8 offsets with 16 bit each, such that several time instances of the pixel information can be written to each offset position. Simultaneous read and write operations allow for the use of 7 of the 8 offset positions, i.e. our architecture allows for a correction depth of $n = 7$. The offset increases to the next higher position with each incrementation of k, which is the temporal indexing of the images. Hence, the incoming data will firstly overwrite the offset position 0 with the pixel from time index $k = 9$, and continue overwriting with all higher time indices. This can be seen as a ring-buffer for the mapping of temporal indices to offset positions in each word. Hence, the implementation of a crossbar is necessary at the read-port, but a demultiplexer is sufficient at write. Addresses are shown in a simplified way with column and row indices, where row indices are positioned at lower significant bits in order to automatically grant for read accesses to half-columns when the address is incremented. One such memory subsystem is instantiated per hemisphere, reducing the row address to 9 bit. The write rate is $400 \cdot 1024 \cdot 512 \approx 209.7$ megasamples per second, thus the user side clock rate of the memory interface is chosen to be 225 MHz. A wrapping logic around read and write port additionally counts the write cycles and triggers the read process once sufficient images are buffered in memory. This is not shown in Figure 5.13.

We partition the description of the processing pipeline in two steps, which cover the parallel computation of two FFTs in one IP core, and the block design of the pipeline itself. As can be seen in Figure 5.13, four time-instance are concurrently read from each memory, such that four half columns are put into the calculation pipeline that starts with the FFT. Still, only two FFT cores are sufficient behind each memory, because the complex input of each Fourier core can be used for transformation of two real signals [65]. This leads to a requirement for separating both transformed vectors at the output of the FFT core, such that the output stream of each FFT sequence has to be accessed concurrently in forward and backward direction. Hence, we implemented an on-the-fly calculation that uses both ports of a block RAM for concurrent read-out in both orders (Figure 5.14). Two such block RAMs are needed, since one has to be read while the other

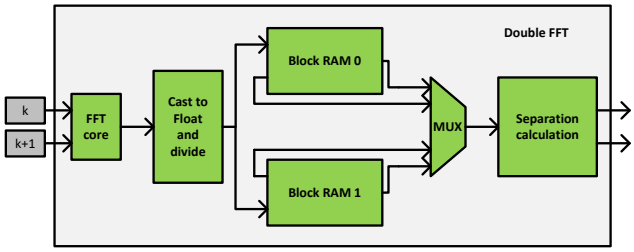

Figure 5.14: Architecture for the computation of two real FFTs on one complex core.

one is filled. The separation calculation is done in floating point. A necessary division by a factor of two is included in the cast to floating point. We call this architecture a double FFT module.

Given the double FFT module that contains the FFT itself and the logic for concurrent processing of two signals, one simply finds that two of those are needed to interface a memory of a correction depth of $n = 4$. The instantiation of both in one calculation channel can be seen in Figure 5.15. The interface of one memory subsystem is connected

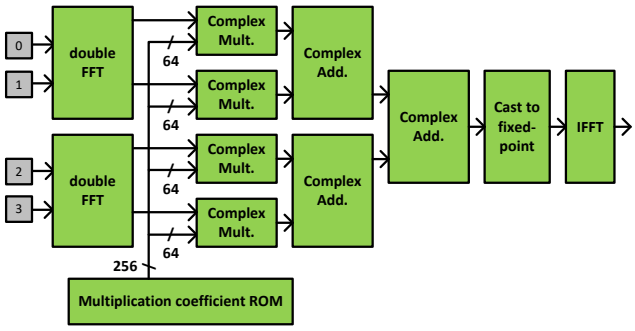

Figure 5.15: Structure of a calculation channel for smear correction in the aperiodic case.

to two double FFT modules. The latter output floating-point signals of twice the original length, which are multiplied element-wise with the precalculated coefficients for the actual correction of the signal. After multiplication, several time-instances are added, casted to fixed-point and back-transformed in order to obtain the final signal as defined in equation (5.13). These results are then passed to the Ethernet subsystem (Figure 5.11). The next half-column is processed in a second channel inside the same pipeline, in order to handle the growth in data rates due to vector extensions with zeros.

Finally, we show the parallelization in the architecture in Figure 5.16. It can be seen that the architecture is split in two parts along the direction of the pipeline, and this splitting is related to the frame store arrays. Each frame store array is assigned to one dedicated QDR II+ SRAM, but the connection via 10GE is shared on both the receiving and the transmitting side. Each QDR II+ SRAM is connected to two calculation pipelines, which is due to the extension of the half-columns with zeros in equation (5.13). Hence, there is a temporal multiplexing and demultiplexing sketched around both instances of calculation pipelines per channel. The inverse FFTs operate on extended half-columns as well, such that four are required instead of two. And eight double FFTs are required, which is related to the depth of correction. A higher depth of correction would simply change the amount of double FFT modules and the adder pyramid in the calculation pipeline, but it would not affect the length of the transform and the temporal duration of the calculation beyond that additional adder.

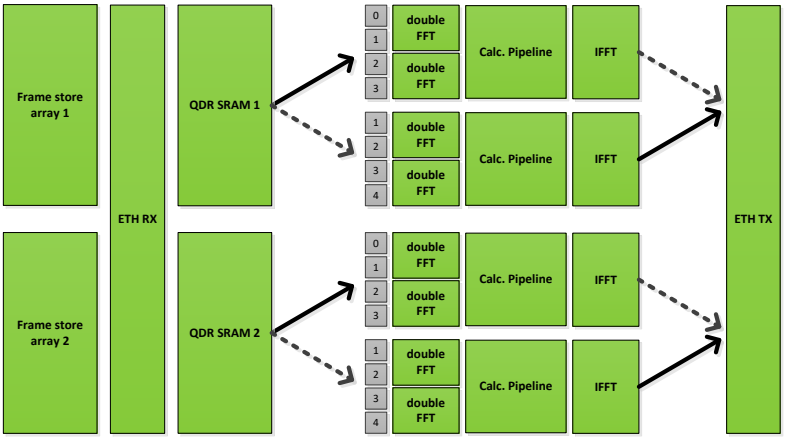

Figure 5.16: Parallelization in the architecture.

5.2.3 Results

The design has been implemented model-based and hence continuously tested in reference to MatLab algorithms. Several intermediate tests have been done and test benches from Xilinx Ethernet PHY and Memory Interface Generator have been used. However, the fundament of our design are verified algorithms from [11] that have been validated with the FSP camera phase I prototype. Especially equation (5.4) has been trusted and used to synthetically smear series of images to resemble true FSP data. These image series have then been sent to the FPGA and processed in order to verify the functionality of the architecture.

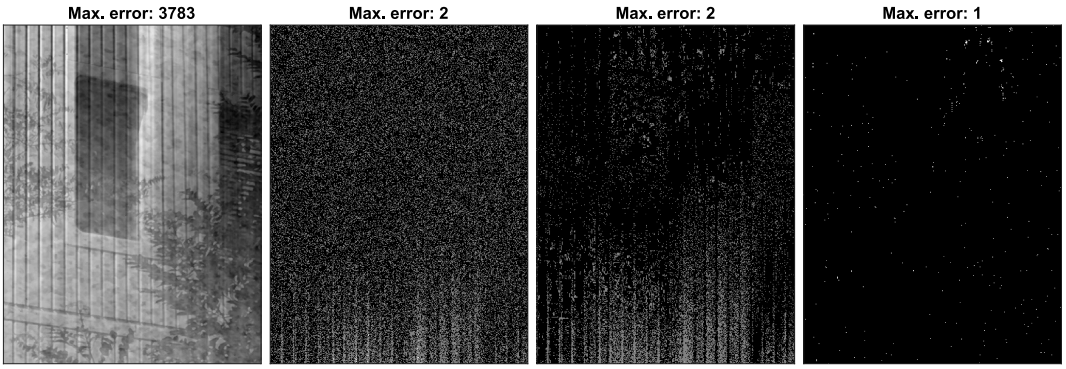

(a) $n = 0$ **(b)** hardware, $n = 4$ **(c)** software, $n = 4$ **(d)** software, $n = 6$

Figure 5.17: Comparison of hardware-accelerated and software-based readout smear correction.

Figure 5.17 shows the results of the test as difference images. They consist of smear only as the reference image itself has been subtracted. Figure 5.17a is the smear of the first image of one series. The smear's maximum value is 3783 in uint16 format, which is a significant degradation of up to 5 percent in relation to the sample value range. The difference image after the correction in hardware is shown in Figure 5.17b. It contains a maximum error of two in uint16 format. This maximum error is lower than the cut-off of three bits due to noise degradation in observations and hence sufficient to allow for an application of the hardware accelerator to FSP in phase II. Furthermore, it confirms the MatLab model, whose equivalent result is shown in Figure 5.17c. Again, a difference image from the software model is shown in Figure 5.17d, but for a correction depth of $n = 6$. This image shows a maximum error of 1 digital unit in uint16 on some scattered positions only, which can be assumed to be caused by rounding effects.

Considering the cut-off due to noise, a correction depth of $n = 4$ is sufficient. Thus, Table 5.2 shows the final costs of the implementation for this architecture. However, the table does not include external QDR II+ SRAM. Altogether, as typical for image processing, memory is the most heavily used resource. The bulk of logic is used for FFTs, implying a nearly linear scaling of its utilization with the depth of correction. RAM instead is also used at non-parallel interfaces and thus its utilization scales less than linear with n.

Table 5.2: Resource Utilization in the final design for $n = 4$.

	LUTs	Block RAM	DSPs	Pipeline Clock	Power Loss
Absolute	81375	165.5	1048	225 MHz	11.22 W
Utilization	18.78%	11.26%	29.11%	50 %	–

As the FFTs have a workload of nearly a hundred percent, one could roughly estimate the operation-count as a product of multiply-accumulate units times FFT frequency to a quarter of a Teraoperation per second, which is within the first estimate. The power consumption is within the expected margins between 10 and 15 Watt. Unused logic allows for a reduction of the chip size as well as for further parallelization of the Fourier transforms and complex multiplications in order to decrease frequency and power for further implementations. Several degrees of freedom can be named for future implementation variants, out of which especially parallelization should be explored when different resource or performance constraints are given. The sequential algorithm would perform similar at $n = 4$ with lower logic but more RAM utilization, and cheaper DDR3 RAM can be built in at the cost of block RAM and logic. A higher parallelization can be applied as well if one cuts smaller matrices from the circulant one in order to reduce power on other devices. Possible future applications of our hardware accelerator cover all frame store CCD cameras operated at similar, fast-switching scene conditions.

Finally, we like to return to our finding that readout smear is motion-blur and explicitly

not signal-dependent noise, which was a fundamental assumption for the development of the target algorithm [11]. This has no implications on the correction of the smear itself, because our finding is based on mathematical equivalence between both types of correction. But it is intended to use the hardware-accelerator for the accumulation of jittered images on Sunrise. Hence, the assumption does not hold that readout smear is corrected perfectly, because the scene is not only variable but further affected by a second PSF. We think it should be possible that two effects occur in this setting. We assume that a residual error from imperfect smear corrections might be present on the one hand. On the other hand, we think that this residual error might affect the image registration, because it is of the type of motion-blur on which the image registration is sensitive. However, it was neither possible to acquire polarimetric material nor to study the data reduction. But we think that a sensitivity analysis on this case is not very interesting for several reasons. FSP can be assumed to operate as expected as long as no jitter is present. Hence, there is no difference to the application of a different camera since there is no additional drawback, and even the online smear correction might be bridged under stable conditions. More importantly, FSP has become obsolete for an implementation on Sunrise 3, such that a case study would be unnecessary work. Instead, we propose to respect readout smear as additional motion-blur kernel if further investigations are required, and to study its effect on image registration if needed.

We conclude our work on the computation of readout smear corrections with theoretical findings. Readout smear can be seen as motion-blur degradation, which normally is post-facto corrected in scientific applications. We do not criticize the application of the correction via matrix-multiplications, but we think that an understanding as convolution operations should make sense. Furthermore, the direct filtering is possible because the sampling function is accurately known and has no cut-off frequencies. Hence, the computation may be calculated fast if there is a related requirement. We further showed methods for the parallel and the approximate computation of readout smear. The approximation in the aperiodic case is the only mathematical change in our algorithms, and was tested under ground truth on the verified algorithms. Unfortunately, we have to conclude that FSP seems not to be the perfect candidate to overcome the limitations of micro-vibrations on Sunrise 3. This is not only due to the violation of the Nyquist-criterion at the sampling of the PSDs, but FSP further induces a second motion-blur kernel. This second motion-blur kernel is readout smear, which can be assumed to affect the image registration and the PSF reconstruction, because its correction is imperfect due to the jitter vice versa.

6 Conclusion

We conclude our work on micro-vibrations and readout smear in this chapter. A summary of all relevant statements from the previous chapters is given in Section 6.1. Furthermore, we offer a critical review of the same statements in Section 6.2, in order to extract four hard findings which can be assumed to resist a scientific discussion. These hard findings are used to derive the expectable impact of this thesis on the related literature in Section 6.3. Lastly, we derive interesting possibilties for future research from the other statements in Section 6.4, and conclude with the lesson learned from this thesis: The temporal sampling function of cameras might be adopted to several textbooks in electro-optical imaging.

6.1 Summary

This thesis offered a new point of view on micro-vibrations and readout smear in scientific images. Both was described as motion-blur and explained in the context of the Sunrise solar observatory and the FSP camera in its phase II implementation. For this purpose, we introduced both projects in Chapter 1 with a strong focus on the problem formulation and the strategic approach. Micro-vibrations are a common problem in modern telescopes and normally handled via measurement and mitigation strategies. This implies iterative processes, and limited success of such procedures is to be expected when the telescope is not accessible during observation. Furthermore, it cannot be assumed that a mitigation strategy will completely eliminate the occurrence of micro-vibrations, because contributors like wind will remain present. Hence, we investigated the degrading effect on the scientific data instead of the sources of micro-vibrations. Another effect of vibrations can be seen on sensors with higher framerate, which can be assumed to measure the degradation resulting from vibration. Thus, the standard methods from technical astronomy were investigated, because they link measurement and correction of such degradation in telescopes like Sunrise. This also explained our focus on the FSP camera, which might be able to perform sampling of the vibration during simultaneous acquisition of scientific data.

Based on our first ideas, we studied in Chapter 2 the related literature on the image formation model and technical astronomy. Our theses are: The correct abstraction layer for our investigation is the image defined by a single subaperture, because each step of measurement and correction of the degradation resulting from vibration relies on this subaperture. The correct methods for measurement are image correlation techniques from extended scene astronomy, and the suitable ones for correction are AO-based and

post-facto methods. AO-based correction is by definition incomplete, such that a post-facto method has to be adopted for micro-vibrations. We focused on Sunrise only, where the imaging process was identified as long-exposure case. It was cited that the knowledge of the overall PSF is mandatory in this case. Hence, a PSF of the micro-vibration has to be measured via image correlation. This technique was identified as DWFS, if AO telemetry data is used. Sunrise is a special case, because vibrations affect the scientific data as translational shifts only, which can be measured on a camera that is no wavefront sensor. The utilization of a high-cadence imager like FSP allows for overcoming NCPEs. Such registration of a simply translated subaperture is further sufficient to describe high-order measurements in AOs, because incoherence can be neglected in the registration. But the assumption of a temporally frozen kernel in the subaperture is not necessarily true for micro-vibrations. Vibrations do not necessarily follow statistics of atmospheric turbulence, such that the resulting image shift in a subaperture may change during exposure. This requirement for a frozen turbulence has to be relaxed, in order to generate measurements which represent the vibrations, so that they can be applied for corrections.

Chapter 3 presented the area-based registration of blur, and the reconstruction of time series acquired with Nyquist sampling cameras. Both theories rely heavily on both, our previous theses and the state-of-the-art. Our previous theses embedded these theories into technical astronomy. But the state-of-the-art in image formation was criticized for its redundant description of motion and vibration as one-dimensional MTFs. We stated that both is the same, referred to better models for motion-blur in image processing, and focused on the registration of motion-blur from there on. The motion centroid assumption is the only theory that explaines the role of arbitrary blur in image registration, since blur induces the shift in this theory instead of hindering its detection. We stated that hybrid imaging further violates assumptions of the image formation model, because the calculated CoGs of the motion trace do not correspond to CoGs of the motion-blur kernels. Hence, we explained that the wanted PSFs is nothing more than a projection of the trace to the pixel grid of the sensor, and that we require equality of the CoGs of both. We exemplarily explained via object cancellation that the ADF method calculates the CoG-distance of the blur kernels of the inferred images. And we followed that there is an invertible relation between trace samples and CoGs of both, blur kernels and their fundamental traces. Hence, we derived the sampling function that explains the degradation in time series, which is invertible if the time series is acquired via Nyquist sampling cameras. And we offered repeatable experiments for verification of this filter on two types of time series, which are the relative position between image and object and the intensity of the object. We stated that the first experiment also validates the motion centroid assumption. Furthermore, the Nyquist criterion for the sampling of time series is explainable via the filter reconstruction, but the motion centroid assumption is independent of sampling rates. Finally, we formulated a pure presumption as hypothesis: The sampling function is suspected to degrade all conceivable time series acquired with cameras, such that our finding might be discussed as extension of the image formation model to the temporal domain.

Chapter 4 presented simulations that illustrate the application of our theories from the previous chapter, but did not introduce new theses. We showed in a brief description how we generated degraded images in computer simulations, and highlighted common problems like edge-effects or the choice of the interpolator. The simulations on the accuracy of the Sunrise AO on the 2009 flight were done as sensitivity analysis, which was used to illustrate boundary conditions of the registration of blur with heavily oversampling cameras. We found that larger subapertures are mandatory for the registration of time-variant blur, in order to compensate for increasing RMS errors that arise with larger extents of the blur kernels. But this relation was neither found in literature nor was it explained in this work. We found that all algorithms from extended scene AOs perform well on subpixel-shifts at large supapertures. Known features of the standard image registration were identified in the registration of blur, and interpreted as evidence for our theory. We further investigated the registration of blur in case of high-cadence science cameras, where larger shifts and heavy blur-extents hinder the registration via the CFF method. We differentiated between Nyquist sampling and aliasing cameras, in order to illustrate the effect on the reconstruction of several signals like traces and PSFs. Similarly, we only showed the resulting effect from utilizing the calculated PSFs as input in blind-deconvolution algorithms, and found that the subjective image quality increases with knowledge of the PSF. We found that metrics of error distances, for example the Strehl ratio of difference PSFs, decrease with the application of the reconstruction filter at Nyquist-sampling cameras. But the utilization of oversampling cameras can suppress the related error as well. Unfortunately, we cannot state if FSP on Sunrise will solve the deconvolution problems. But we think that our examples are helpful for understanding the registration of blur in practical applications, for example layouting future AOs.

Chapter 5 covered our work on the computation of readout smear corrections. We started with a requirement on the implementation and followed the standard design flow. Hence, we have no theses on the validity of the target algorithms or its application within the data reduction. But we claim that we have finally identified readout smear as motion-blur, even if forward transfer functions were known for the standard case. We stated that the standard case and the periodic case are convolution operations, which can be applied via direct filtering. The aperiodic case was approximated by the periodic one, and further parallelized via the charge flush and reverse clocking case. All optimization allowed for the implementation of an FPGA-based hardware-accelerator as requested. But we expect that a correction would only be partial, because the image is not standing stable during exposure. Hence, there might be residual smearing left, which could have impact on the registration of short exposure images. Thus, we think that our theses related to readout smear are of more theoretical value, such that readout smear should be recognized as linear motion-blur, and might be handled as PSF in future applications.

6.2 Critical review

The last section offered a summary of all kinds of statements which might affect a conceivable impact on literature. However, a scientific discussion will always contain a critical point of view, and a main part of our work consisted of evaluating possible limitations of our work. Hence, we critically review our work in this section, in order to extract all hard findings which may hold a discussion and could probably have impact on literature.

Chapter 1 introduces FSP and Sunrise on a very abstract level, such that all information is purely theoretical. It is stated that the consideration of micro-vibrations as mechanical problem is not optimal, and should be reformulated under an image processing perspective. This results in a strict application of methods that are the most fundamental standard techniques from technical astronomy, which also is the basis of the strategic approach. Problematic in this regard is that each astronomer can be assumed to have experience in the practical application of the standard methods to micro-vibrations in telescopes, and that this practical application was not possible in the pace of this thesis. Hence, there is a fundamental critique on our theoretical proceeding, because all results are neither evaluated in its application, nor are practical problems visible to us. The latter argument targets the phenomenon that negative research results are not necessarily published. Hence, there is no practical verification of several theses concerning micro-vibrations in optical instruments, and a practical problem solution for a telescope or an AO system is hard to expect.

Chapter 2 investigates only some of the most fundamental theories of the image formation model and technical astronomy, in order to judge if certain ones seem useful or problematic for further investigations. The image registration is identified as useful, while the lay-outing of adaptive optics is criticized on the other hand. It is clear that not all conceivable vibrations will follow Kolmogorow statistics. But one cannot assume that all practical problems with vibrations are identified, based on these particular theoretical investigations. There is no discussion if other problems might occur, and it is only assumed that a correct measurement of the error is the solution. Hence, an implicit hypothesis in this work is that correction methods from technical astronomy work sufficiently when the error is known. Counter-arguments might be that the frequencies of micro-vibrations could exceed the bandwidth of the AO, or that performances of different post-facto processing techniques may vary.

More practical are the test results in Chapter 3. Repeatable measurements are hard to criticize, and serve as basis of technical science for this reason. Hence, serious critique would argue with different measurements, and theoretical discussions cannot be of high value in this context. But it is possible to argue against the interpretation of these results. It is stated that the resulting extension of the image formation model to the temporal domain is nothing more than a hypothesis. And the argumentation for the registration of blur is incomplete. Noise is not respected, and the registration is only exemplarily derived for one paricular method. Furthermore, the proposed methods rely on

the integration properties of detectors, which are not formulated, but explicitly located around the interpolation problem whose handling is avoided. Most importantly, there is no explicit evidence for the property of this integration that the CoGs remain constant when traces are interpolated to blur kernels. Hence, this theory seems mathematically incomplete and a discussion in context of image formation is open. The experiments cover interesting findings with first proposals for explanation, but they are only related to the micro-vibration problem via theoretical investigations.

Chapter 4 shows simulations that illustrate the application of the theories from the previous chapter. It is notable that only one of the two experiments is further investigated, the other one is not related to practical applications. It is stated that there are no theses on the image generation, and it is explicitly worked on unvalidated interpolation methods that only fulfill self-set requirements of CoG preservation. It seems clear that the method would not work under different assumptions. The section on the AO operation only highlights an idea, which is that extents of the inferred blur kernels seem to suppress the accuracy of the registration, which should be compensated for with high signal variances. It is explained that this relation is neither understood in literature nor in this work. There is no citation if standard AOs measure vibrations correctly, which seems to be interesting in relation to the measurements on the image sizes. The following simulations only illustrate the effect of Nyquist sampling and aliasing, which is well understood. It is shown that a reconstruction filter works if the Nyquist criterion holds. Furthermore, the software tests show that this constraint is applicable to the registration of blur. There is no explicit quantization of a goodness criterion on the signal reconstruction, even if the argumentation with absolute goodness metrics is known to be problematic. The deconvolution results are interpreted as a subjective improvement in image quality, and do not hold any scientific discussion.

Chapter 5 handles optimizations on the computation of readout smear corrections. The optimizations rely on the finding that the standard case and the periodic case are convolution operations. Several citations on the mathematical equivalence of blur and readout smear are confirmed by a variety of publications. Same accounts for the extension of the Toeplitz matrices to circulant ones, i.e. the proposed strategy for parallelization. But the work is quite theoretical again. It is only shown that the theoretical comparison against ground truth holds in computer simulations, either on a PC or an FPGA. The whole application is further limited to the case where FSP's parameters are used. And it is questionable if the smearing or its imperfect correction will affect the registration of short exposure images. It could be interesting to know how smearing interacts with vibration induced motion-blur, for example if the smear-kernels act as temporal sampling functions of cameras. On the other hand, only limited success can be expected in a case study, given that the Nyquist criterion on time series is verified.

All in all, it can be subsumed that this thesis lacks a practical application. It is based on the theoretical assumption that the frozen-flow hypothesis is invalid for micro-vibrations, and that its violation would result in motion-blur. One must state that

it would be questionable to derive a direct impact of these theoretical results on real applications like AOs or telescopes, which are normally the subjects of discussions in proceedings and journals. On the other hand, it can be concluded that some hard findings hold. Hence, we explicitely name these findings in order to derive direct impact from these hard findings on literature in the next section: Firstly, there is a sampling function on two time series, the relative translational position between image and object, and the intensity of the object. Secondly, the first experiment on time series validates the area-based registration of blur. Thirdly, the known mathematical equivalences hold if they are applied to readout smear. Lastly, an online processing of readout smear corrections for FSP can be implemented under the assumption of ground truth.

6.3 Impact

The last sections offered a summary of our work and a critical review on it. We think that this thesis provides several hard findings, but several theses remain unverified in their practical applications. The latter especially accounts for polarimetric data reduction pipelines and AOs, which were not accessible in the pace of this work. Hence, we do not derive direct impact on practical applications in technical astronomy. Instead, we discuss these topics in the next section as possible future research related to our work. Direct impact of our hard findings can be found, however, on a lot of publications arguing theoretically, which are partially cited in fundamental textbooks. Hence, we derive direct impact of our hard findings on these theoretical discussions in this section.

Chapter 2 investigated fundamental theories in image formation and technical astronomy. We cited discussions on technical astronomy [26, 30], Fourier optics [28], optics [27], and MTFs [29]. All discussions are far developed, such that textbooks were exemplarily cited, and all references argue with an image formation model that focuses on a static object. We affected these discussions with a proposal for a temporal image formation model, in which the camera shoots sequences of photos containing a variable object. This introduces the time series, the duty-cycle, and the temporal sampling function of cameras in these discussions, and the impact is verified for at least two time series. Only within technical astronomy, the image registration with methods from extended scene AOs might be seen as more independent of atmospheric statistics. This is because the correlation is now independent of the frozen-flow hypothesis, and dependend on the Nyquist criterion instead, so that time series of the relative position between image and object can be reconstructed. This accounts for post-facto reconstruction of coherent motion traces and PSFs, but remains unverified for real-time processing in the control loops of AOs and images degraded by incoherent wavefronts. Furthermore, we cannot say if this will allow for sufficient correction of micro-vibration induced image degradation, but we think that the initial description of the error is a significant step on the way towards its correction, and might have impact on the basic discussions in [26, 30]. In addition, we see a more detailed impact on the discussion on MTFs in electro-optical systems. From our point of view, the explanation of motion and vibration as MTF in [29] has to

be seen with certain scepticism. It could make sense to recognize both as the same, and to explain them as two-dimensional transfer functions with a phase information that is not necessarily equal to zero. We have shown that a temporal variation of the objects position is not causing a spatial MTF, but a temporal one. This understanding could be adopted to the underlying discussion, whose fundamental contributions are cited in [29].

Next to the temporal image formation, we also introduced the area-based registration of blur as a verified theory. The definition of the shift of an image via the motion centroid assumption is the contribution of [46], as well as the idea to register the CoGs of the blur kernels. But we claim that we have verified this assumption, adopted this method to area-based registration techniques, and interpreted it within the image formation model. Hence, there might be a possible impact on the hybrid imaging itself, for example the trace-reconstruction could be discussed in relation to the image formation model. In addition, we think the motion centroid assumption is not only valid for slight shifts in short exposure images, but our work might help to accept this assumption as a definition of the shift of an image within the standard equation in image processing, i.e. within the image formation model. This definition of the shift of an image might serve as basis of all methods concerning image registration and image shifting. We highlighted the absence of this definition of the shift of an image in relation to invariances, and we left with the critique that it seems unclear in this case what is registered and what not. Hence, we cannot judge about invariances, but expect clear definitions of shifts and invariances as impact, for example in [44]. Next to invariances, we referred with a survey [43] to a vast amount of conceivable registration methods, which do not always concern invariances, but mostly lack a definition of the detected shift within the standard image model as well. Beside the definition of the shift, the discussions on image registration often lack dynamic models in signal processing. We think that sequential photography could be recognized as sampling, the resulting series might be defined as temporally variable coordinates between object plane and image plane, and the cameras temporal sampling functions could be considered. We found nothing like an abstract shift outside the standard equation in image processing, which could be analytically detected by shifting reference images. Instead, the blur of a signal was found to define several shifts, and the application of the signal processing method correlation identified to average via implicit CoG calculation. The imperfect extent of the sampling function was considered to cause the blur, and to define a filter that reconstructs the series. The requirement on Nyquist sampling was suspected to stem from the signal reconstruction, the correlation was presumed to be independent of it, and violation of the Nyquist criterion has resulted in aliasing of our measurements. Hence, one conceivable impact is that dynamic signal processing seems to be usefull if it is adopted to image registration tasks, or to correlation methods and blur in general. Standard image registration is a frequently discussed topic, and focuses on a static shift between two images. We think it might be possible to adopt all static approaches to dynamic ones, given that the temporal sampling function of the camera is considered. Hence, we refer to the cited survey on image registration [43] for the description of a possible impact of dynamic methods in static image registration.

Finally, we see some possible impact of our findings on the discussion on readout smear. We cannot say exactly if readout smear was previously seen as blur, or only described with a forward transfer function in the standard case. But we have considered readout smear as linear motion-blur, i.e. there are more precise definitions conceivable. In addition, we followed that the application of the correction might be seen as filtering operation for the standard case and the periodic one. The fundamental space of non-standard cases consists of several images. Hence, the case for charge flush and reverse clocking might be seen as convolution in an extended space similarly. And the aperiodic case could probably be seen as convolution-like operation, because something like edge effects occurs if a false assumption of periodicity is applied. However, at least an explicit description as noise might be discussed. Several methods for optimized computation seem conceivable whenever there are requirements on the computation. And we think that a first proposal for a particular architecture might be seen as impact as well, even if there is no reference for comparison. For example, the existence of this architecture might be helpful to argue for future framestore CCD based sensor designs.

6.4 Outlook

The last section derived a possible impact on several discussions based on the hard findings in this work. But we also identified several theses that are not verified in their practical applications, and we describe their practical applications as possibilities for future research. Furthermore, we highlight some open questions which were found during our work, in order to propose further investigations.

The most likely practical application of our ideas might be related to the Sunrise project, which served as the main example but was practically not accessible during the work. A practical application of our ideas to Sunrise is outlined hereafter. We think that the accuracy of the CWS could be improved via utilization of the SDF method on subapertures of 80×80 pixel, but the achievable exposure time seems to be sufficient to avoid the implementation of an inverse sinc filter in the control loop. Even a correct measurement of the residuals at the CWS is expected to remain the problem unsolved, because the occurrence of NCPEs can be anticipated. But we think that the application of standard DWFS can be very helpful in a first step. All cameras might be synchronized, and the camera data and the telemetry data could be written back with timestamp. This might lead to an understanding of the problem, for example the phase information of the jitter could become visible, or one might see how constant the problem is over time. We think it is important to perform these measurements for a short time when all mirrors are disabled, because the true jitter signal could be measured, and the location on common or non-common paths could become visible. This true signal might be used to specify a sampling rate for a high-cadence imager that could be used against NCPEs. Such high-cadence imager might be used for NCPE-hard calculation

of tip-tilt PSFs, and it could be interesting to control the tip-tilt-mirror with it. The latter would require an online application of the boxcar-filter. Otherwise, a dedicated tip-tilt sensor seems to be a good idea as well, because the residuals would be measured from two positions. One could mention to install the dedicated tip-tilt sensor spatially close to the scientific cameras, and could probably reduce the length of the non-common paths. But one could also assume that vibrations spread via transfer functions, and that difference functions of them might become measurable when two sensors sample the resulting image shifts. Hence, it seems possible to acquire information about the location of the vibrations via matched filters, when two CWSs sample their impact. However, the main problem remaining is the occurrence of NCPEs. We proposed the utilization of a high-cadence imager. But there are several drawbacks with this approach. We stated that the phase II implementation of FSP is obsolete for Sunrise 3, there are the problems with readout smear and aliasing, and all cameras on Sunrise 1 and 2 are of long-exposure type. Hence, we investigated methods which have the potential to overcome a forwarding and amplifying of non-common residuals from the AO path to the paths of the science cameras. In this context, we like to suggest extending the idea of Castro [66], where the measurement of vibrations via a laser dot is presented. If one induces a light dot in the unused side of the beamsplitter, one might calculate the non-common residuals on the AO path in real-time on the correlation tracker from the dot, such that they can be subtracted from the AO telemetry data. This thought might be continued in a way that the dot could be used in relation to the science camera. Investigation of feasibility was started, but not continued. It can be seen in Figure 3.5 that we started with a simple laser-pointer measuring non-common residuals resulting from vibration. The vibrations were induced via bass-shakers that played audio-files of our jitter signals $x(t)$ and $y(t)$. The laser pointer should later be replaced by a fiber that is glued to the beamsplitter, in order to avoid one further non-common path. It was planned to register both the dot and the scene on one correlation tracker, in order to subtract non-common residuals from the mirrors set values.

We are not sure if these ideas could help to solve the NCPE induced problems on Sunrise. But we think that the utilization of a Nyquist sampling high-cadence imager for both, scientific imaging and DWFS, can solve the impact of low frequent tip-tilt residuals. In this context, we also propose future research to the Semiconductor Laboratory of the Max-Planck-Society. They found increasing demands for high-cadence detectors during the last years in several scientific disciplines, partially to overcome limitations like inter-Stokes crosstalk in polarimetry, and partially to film high-speed processes. Another standard requirement is the combination of the readout speed with minimal noise budgets, which is by definition challenging. Their latest developments extend the DEPFET technology to differential readouts of sensors, i.e. determination of incrementally accumulated charge without the destruction of the overall accumulated charge information due to readout. Within a next step, it could be interesting to port the registration of short exposure images to such differential images with high readout speed, which may allow gathering a motion-blur PSF of an image during the accumulation of that very image. Then, the complete accumulated charge information may be slowly read out with

low readout noise. One conceivable alternative is the implementation of a second fast sensor on the chip of the long-exposure sensor, as was previously recommended within hybrid imaging. Again, this sensor could be used for DWFS, or to steer a tip-tilt mirror.

Next to Sunrise and FSP, we think it could be possible to apply our findings in the wider range of technical astronomy. For example, it seems possible to investigate the use of DWFS against vibrations in case studies. Or the use of a boxcar-filter in AO control loops might be investigated. We expect that this only makes sense if a critical ratio of jitter-period to exposure time is present, which is typically valid in night-time astronomy, and the effect on the bandwidth might be interesting. Furthermore, registration of images degraded by turbulence results in spatial averaging over residual incoherence in several subapertures, and hence the effect of a spatial boxcar-filter on the registration results might be investigated. Next, we have neglected the short-exposure imaging in this thesis, but we think it would be straight-forward to study the use of speckle imaging against micro-vibrations. This is, because we stated that the boxcar-filter on time series of varying intensities lacks a practical application. One similar idea is to investigate the use of the boxcar-filter in relation to inter-Stokes crosstalk. We presume that high-frequent, residual tip-tilt signals could possibly be supressed with the implementation of our filter in the control loops of AOs, and that time series of varying polarimetric intensities could be handled with a sampling function instead of linearization [67]. Finally, we think it would be straight-forward to investigate the position encoders of the mirrors for amplitude underestimation, for example. However, these ideas are highly speculative and not investigated yet.

Similar ideas can be formulated in relation to our open questions. Firstly, we think that the accuracy of different registration techniques, depending on the kind of the method and properties of the blur, should be investigated. This is because we found that not all image registration methods measure dynamic shifts as accurately as methods from technical astronomy, and even these methods require larger correlated areas if static constraints do not hold. Secondly, we found an open question around the interpolation and pixel integration. We are not sure if the image formation model could serve to derive an ideal interpolation method. But the related discussion is quite overwhelming, and the image formation model is rarely respected. Hence, there might be future research.

All in all, we think that motion-blur should be explicitely discussed in scientific imaging. It was not well identified in the past, but its impact is described. The methods for its handling seem to be suitable, be it the registration in AOs, the deconvolution, or the filtering of readout smear. Problematic in the discussions is the avoidance of dynamic methods from signal processing, and the focusing on static constraints. Hence, we propose to introduce the temporal sampling function of cameras into cited discussions, as well as some resulting insights like the definition of the shift of an image, reconstruction filters for readout smear and several time series, or an adaption of correction methods like AOs. Most interesting would be a practical application of our theoretical ideas to some real experiments, which was rarely possible during this work. Hence, we hope that

the temporal sampling function of cameras will be adopted to cited literature.

Bibliography

[1] Webpage Sunrise 2 [online]. 2017. URL: https://www.mps.mpg.de/Ein-zweiter-Blick-auf-die-Sonne [last checked 2018-06-27].

[2] Webpage Sunrise [online]. 2013. URL: https://www.mps.mpg.de/sonnenforschung/sunrise [last checked 2018-06-27].

[3] S. K. Solanki, A. M. Gandorfer, M. Schuessler, W. Curdt, B. W. Lites, V. Martínez Pillet, S. W., and A. M. Title. Sunrise: a balloon-borne telescope for high resolution solar observations in the visible and uv, 2003. URL: https://doi.org/10.1117/12.460283, doi:10.1117/12.460283.

[4] P. Barthol, A. Gandorfer, S. K. Solanki, M. Schüssler, B. Chares, W. Curdt, W. Deutsch, A. Feller, D. Germerott, B. Grauf, K. Heerlein, J. Hirzberger, M. Kolleck, R. Meller, R. Müller, T. L. Riethmüller, G. Tomasch, M. Knölker, B. W. Lites, G. Card, D. Elmore, J. Fox, A. Lecinski, P. Nelson, R. Summers, A. Watt, V. Martínez Pillet, J. A. Bonet, W. Schmidt, T. Berkefeld, A. M. Title, V. Domingo, J. L. Gasent Blesa, J. C. Del Toro Iniesta, A. López Jiménez, A. Álvarez-Herrero, L. Sabau-Graziati, C. Widani, P. Haberler, K. Härtel, D. Kampf, T. Levin, I. Pérez Grande, A. Sanz-Andrés, and E. Schmidt. The Sunrise Mission. *Solar Physics*, 268:1–34, January 2011. arXiv:1009.2689, doi:10.1007/s11207-010-9662-9.

[5] T. Berkefeld, W. Schmidt, D. Soltau, A. Bell, H. P. Doerr, B. Feger, R. Friedlein, K. Gerber, F. Heidecke, T. Kentischer, O. v. D. Lühe, M. Sigwarth, E. Wälde, P. Barthol, W. Deutsch, A. Gandorfer, D. Germerott, B. Grauf, R. Meller, A. Álvarez-Herrero, M. Knölker, V. Martínez Pillet, S. K. Solanki, and A. M. Title. The Wave-Front Correction System for the Sunrise Balloon-Borne Solar Observatory. *Solar Physics*, 268:103–123, January 2011. arXiv:1009.3196, doi:10.1007/s11207-010-9676-3.

[6] A. Gandorfer, B. Grauf, P. Barthol, T. L. Riethmüller, S. K. Solanki, B. Chares, W. Deutsch, S. Ebert, A. Feller, D. Germerott, K. Heerlein, J. Heinrichs, D. Hirche, J. Hirzberger, M. Kolleck, R. Meller, R. Müller, R. Schäfer, G. Tomasch, M. Knölker, V. Martínez Pillet, J. A. Bonet, W. Schmidt, T. Berkefeld, B. Feger, F. Heidecke, D. Soltau, A. Tischenberg, A. Fischer, A. Title, H. Anwand, and E. Schmidt. The Filter Imager SuFI and the Image Stabilization and Light Distribution System ISLiD of the Sunrise Balloon-Borne Observatory: Instrument Description. *Solar Physics*, 268:35–55, January 2011. arXiv:1009.1037, doi:10.1007/s11207-010-9636-y.

[7] V. Martínez Pillet, J. C. Del Toro Iniesta, A. Á lvarez-Herrero, V. Domingo, J. A. Bonet, L. González Fernández, A. López Jiménez, C. Pastor, J. L. Gasent Blesa, P. Mellado, J. Piqueras, B. Aparicio, M. Balaguer, E. Ballesteros, T. Belenguer, L. R. Bellot Rubio, T. Berkefeld, M. Collados, W. Deutsch, A. Feller, F. Girela, B. Grauf, R. L. Heredero, M. Herranz, J. M. Jerónimo, H. Laguna, R. Meller, M. Menéndez, R. Morales, D. Orozco Suárez, G. Ramos, M. Reina, J. L. Ramos, P. Rodríguez, A. Sánchez, N. Uribe-Patarroyo, P. Barthol, A. Gandorfer, M. Knoelker, W. Schmidt, S. K. Solanki, and S. Vargas Domínguez. The Imaging Magnetograph eXperiment (IMaX) for the Sunrise Balloon-Borne Solar Observatory. *Solar Physics*, 268:57–102, January 2011. `arXiv:1009.1095`, `doi:10.1007/s11207-010-9644-y`.

[8] S. K. Solanki, P. Barthol, S. Danilovic, A. Feller, A. Gandorfer, J. Hirzberger, T. L. Riethmüller, M. Schüssler, J. A. Bonet, V. Martínez Pillet, J. C. del Toro Iniesta, V. Domingo, J. Palacios, M. Knölker, N. Bello González, T. Berkefeld, M. Franz, W. Schmidt, and A. M. Title. SUNRISE: Instrument, Mission, Data, and First Results. *The Astrophysical Journal Letters*, 723:L127–L133, November 2010. `arXiv:1008.3460`, `doi:10.1088/2041-8205/723/2/L127`.

[9] W. Schmidt, S. K. Solanki, P. Barthol, T. Berkefeld, A. Gandorfer, M. Knölker, V. Martínez Pillet, M. Schüssler, and A. Title. Sunrise - impressions from a successful science flight. *Astronomische Nachrichten*, 331(6):601–604, 2010. URL: `http://dx.doi.org/10.1002/asna.201011383`, `doi:10.1002/asna.201011383`.

[10] S. K. Solanki, T. L. Riethmüller, P. Barthol, S. Danilovic, W. Deutsch, H.-P. Doerr, A. Feller, A. Gandorfer, D. Germerott, L. Gizon, B. Grauf, K. Heerlein, J. Hirzberger, M. Kolleck, A. Lagg, R. Meller, G. Tomasch, M. van Noort, J. Blanco Rodríguez, J. L. Gasent Blesa, M. Balaguer Jiménez, J. C. Del Toro Iniesta, A. C. López Jiménez, D. Orozco Suarez, T. Berkefeld, C. Halbgewachs, W. Schmidt, A. Álvarez-Herrero, L. Sabau-Graziati, I. Pérez Grande, V. Martínez Pillet, G. Card, R. Centeno, M. Knölker, and A. Lecinski. The Second Flight of the Sunrise Balloon-borne Solar Observatory: Overview of Instrument Updates, the Flight, the Data, and First Results. *The Astrophysical Journal Letters*, 229:2, March 2017. `arXiv:1701.01555`, `doi:10.3847/1538-4365/229/1/2`.

[11] F. A. Iglesias, A. Feller, and K. Nagaraju. Smear correction of highly variable, frame-transfer ccd images with application to polarimetry. *Appl. Opt.*, 54(19):5970–5975, Jul 2015. URL: `http://ao.osa.org/abstract.cfm?URI=ao-54-19-5970`, `doi:10.1364/AO.54.005970`.

[12] Webpage FSP [online]. 2014. URL: `https://www.mps.mpg.de/solar-physics/fsp` [last checked 2018-08-07].

[13] F. A. Iglesias. *Development of a high-cadence, high-precision solar imaging polarimeter with application to the FSP prototype.* phd, 2016. Review method: peer-reviewed. URL: `http://hdl.handle.net/11858/00-001M-0000-002C-1A15-7`.

[14] A. Feller, F. A. Iglesias, K. Nagaraju, S. K. Solanki, S. Ihle, J. O. Stenflo, Q. Qu, and M. Samooprna. Fast solar polarimeter: Description and first results, October 1, 2014 2014. URL: `http://adsabs.harvard.edu/abs/2014ASPC..489..271F`.

[15] F. A. Iglesias, A. Feller, N. Krishnappa, S. K. Solanki, C. E. Fischer, and M. Temmer. Fast solar polarimeter: Prototype characterization and first results, April 1, 2016 2016. URL: `http://adsabs.harvard.edu/abs/2016ASPC..504..325I`.

[16] F. A. Iglesias, A. Feller, K. Nagaraju, and S. K. Solanki. High-resolution, high-sensitivity, ground-based solar spectropolarimetry with a new fast imaging polarimeter. i. prototype characterization. *Astronomy and Astrophysics*, 590, 2016. URL: `http://adsabs.harvard.edu/abs/2016A%26A...590A..89I`.

[17] K. Nagaraju, A. Feller, S. Ihle, and H. Soltau. Atmospheric turbulence and high-precision ground-based solar polarimetry, October 1, 2011 2011. URL: `http://adsabs.harvard.edu/abs/2011SPIE.8148E..0SN`.

[18] Private Communication with Max-Planck Institute for Solar System Research, 2015-2017.

[19] S. Tabel, J. Treis, and W. Stechele. Non-blind deconvolution of the residual tip-tilt error of the sunrise solar observatory. volume 10705, 2018. URL: `https://doi.org/10.1117/12.2311652`, `doi:10.1117/12.2311652`.

[20] S. Tabel. *Verfahren und Vorrichtung zur Rekonstruktion von Zeitreihen, degradiert durch Auslastungsgrade*. German patent application: 10 2018 209 176.5. 2018.

[21] S. Tabel and W. Stechele. Fast computation of readout smear correction for frame-store ccd based images. In *Proceedings of the 2017 International Conference on Computer Graphics and Digital Image Processing*, CGDIP '17, pages 18:1–18:6, New York, NY, USA, 2017. ACM. URL: `http://doi.acm.org/10.1145/3110224.3110233`, `doi:10.1145/3110224.3110233`.

[22] S. Tabel, K. Weikl, and W. Stechele. Hardware-accelerated ccd readout smear correction for fast solar polarimeter. In *2017 IEEE 28th International Conference on Application-specific Systems, Architectures and Processors (ASAP)*, pages 67–74, July 2017. `doi:10.1109/ASAP.2017.7995261`.

[23] S. Tabel and K. Weikl. *Verfahren und Vorrichtung zur Korrektur von Smear-Artefakten*. German patent application: 10 2017 003 170.3. 2017.

[24] S. Tabel and K. Weikl. *Verfahren und Vorrichtung zur Korrektur von Smear-Artefakten*. European patent application: EP18165190.2. 2018.

[25] S. Tabel and K. Weikl. *Method and apparatus for correcting smear artifacts*. US patent application: 15/940,524. 2018.

[26] J. M. Geary. *Introduction to wavefront sensors*, volume 18. Spie Press, 1995.

[27] E. Hecht. *Optics*. Addison-Wesley, 5th global edition, 2016.

[28] J. Goodman. *Introduction to Fourier Optics*. McGraw-Hill, second edition, 1996.

[29] G. D. Boreman. *Modulation transfer function in optical and electro-optical systems*, volume 21. SPIE press Bellingham, WA, 2001.

[30] T. R. Rimmele and J. Marino. Solar adaptive optics. *Living Reviews in Solar Physics*, 2011. URL: `https://link.springer.com/article/10.12942/lrsp-2011-2`, `doi:10.1007/lrsp-2011-2`.

[31] L. Poyneer, M. van Dam, and J.-P. Véran. Experimental verification of the frozen flow atmospheric turbulence assumption with use of astronomical adaptive optics telemetry. *Journal of the Optical Society of America A*, 26:833, March 2009. `doi:10.1364/JOSAA.26.000833`.

[32] M. G. Löfdahl. Evaluation of image-shift measurement algorithms for solar shack-hartmann wavefront sensors. *Astronomy and Astrophysics*, 524, 2010. URL: `https://arxiv.org/abs/1009.3401`.

[33] N. Anugu, P. Garcia, I. Dorotovic, C. E. Fischer, and M. Temmer. Efficient Solar Scene Wavefront Estimation with Reduced Systematic and RMS Errors: Summary. In *Coimbra Solar Physics Meeting: Ground-based Solar Observations in the Space Instrumentation Era*, volume 504, page 113, Apr 2016. URL: `http://science-media.org/userfiles/107/posters/107_poster_46.pdf`.

[34] J. Marino. *Long Exposure Point Spread Function Estimation from Solar Adaptive Optics Loop Data*. PhD thesis, New Jersey Institute of Technology, May 2007.

[35] M. G. Löfdahl, M. J. van Noort, C. Denker, F. Kneer, K. G. Puschmann, and A. D. Wittmann. Solar image restoration. In *Modern solar facilities - advanced solar science*, page 119, Jan 2007.

[36] M. C. Roggemann, B. M. Welsh, and B. R. Hunt. *Imaging through turbulence*. CRC press, 1996.

[37] J. Arines and S. Bará. *Optics and Deconvolution: Wavefront Sensing*, pages 549–569. Wiley-VCH Verlag GmbH & Co. KGaA, 2011. URL: `http://dx.doi.org/10.1002/9783527635245.ch25`, `doi:10.1002/9783527635245.ch25`.

[38] N. Miura, A. Oh-Ishi, S. Kuwamura, N. Baba, S. Ueno, Y. Nakatani, and K. Ichimoto. Deconvolution of partially compensated solar images from additional wavefront sensing. *Appl Opt*, 55(10):2484–8, 2016. `doi:10.1364/ao.55.002484`.

[39] C. Kulcsár, G. Sivo, H.-F. Raynaud, B. Neichel, F. Rigaut, J. Christou, A. Guesalaga, C. Correia, J.-P. Véran, E. Gendron, F. Vidal, G. Rousset, T. Morris, S. Esposito, F. Quiros-Pacheco, G. Agapito, E. Fedrigo, L. Pettazzi, R. Clare,

R. Muradore, O. Guyon, Frantz, Martinache, S. Meimon, and J.-M. Conan. Vibrations in ao control: a short analysis of on-sky data around the world. volume 8447, pages 8447 – 8447 – 14, 2012. URL: https://doi.org/10.1117/12.925984, doi:10.1117/12.925984.

[40] M. Hartung, T. Hayward, L. Saddlemyer, L. Poyneer, A. Cardwell, C. Cavedoni, M. Cho, J. K. Chilcote, P. Collins, D. Dillon, R. Galvez, G. Gausachs, S. Goodsell, A. Guesalaga, P. Hibon, J. Larkin, B. Macintosh, D. Palmer, N. Sadakuni, D. Savransky, A. Serio, F. Rantakyrö, and K. Wallace. On-sky vibration environment for the Gemini Planet Imager and mitigation effort. In *Adaptive Optics Systems IV*, volume 9148 of *Proc. SPIE*, page 91480N, August 2014. arXiv:1407.7893, doi:10.1117/12.2057200.

[41] T. D. Tarbell and R. C. Smithson. Correlation tracking study for meter-class solar telescope on space shuttle - nasa-cr-159908. Report, 1977.

[42] M. Potmesil and I. Chakravarty. Modeling motion blur in computer-generated images. *SIGGRAPH Comput. Graph.*, 17(3):389–399, July 1983. URL: http://doi.acm.org/10.1145/964967.801169, doi:10.1145/964967.801169.

[43] B. Zitova and J. Flusser. Image registration methods: a survey. *Image and vision computing*, 21(11):977–1000, 2003.

[44] V. Ojansivu and J. Heikkila. Image registration using blur-invariant phase correlation. *IEEE signal processing letters*, 14(7):449–452, 2007.

[45] A. Rajagopalan and R. Chellappa. *Motion Deblurring: Algorithms and Systems*. Cambridge University Press, 2014.

[46] M. Ben-Ezra and S. K. Nayar. Motion deblurring using hybrid imaging. In *2003 IEEE Computer Society Conference on Computer Vision and Pattern Recognition, 2003. Proceedings.*, volume 1, pages I–657–I–664 vol.1, June 2003. doi:10.1109/CVPR.2003.1211416.

[47] S. K. Nayar and M. Ben-Ezra. Motion-based motion deblurring. *IEEE Transactions on Pattern Analysis and Machine Intelligence*, 26(6):689–698, June 2004. doi:10.1109/TPAMI.2004.1.

[48] O. von der Lühe. Estimating fried's parameter from a time series of an arbitrary resolved object imaged through atmospheric turbulence. *Journal of the Optical Society of America A*, 1:510–519, 1984. URL: http://adsabs.harvard.edu/abs/1984JOSAA...1..510V.

[49] S. Gladysz, R. Baena Galle, R. L. Johnson, and L. Kann. Image reconstruction of extended objects: demonstration with the starfire optical range 3.5m telescope. volume 8535, pages 8535 – 8535 – 13, 2012. URL: http://dx.doi.org/10.1117/12.974712, doi:10.1117/12.974712.

[50] Danilovic, S., Gandorfer, A., Lagg, A., Schüssler, M., Solanki, S. K., Vögler, A., Katsukawa, Y., and Tsuneta, S. The intensity contrast of solar granulation: comparing hinode sp results with mhd simulations. *A&A*, 484(3):L17–L20, 2008. URL: https://doi.org/10.1051/0004-6361:200809857, doi:10.1051/0004-6361:200809857.

[51] E. Meijering. A chronology of interpolation: from ancient astronomy to modern signal and image processing. *Proceedings of the IEEE*, 90(3):319–342, Mar 2002. doi:10.1109/5.993400.

[52] Matlab tracking fluorescence microscope. Last checked: 2018-08-30. URL: https://github.com/zikegcwk/Matlab_TrackingFluorescenceMicroscope/blob/master/MicroscopeMatlabFunctionsFromSergeyAndMax/Our_libraries/ICSMATLAB/simul8tr/airy2.m.

[53] A. Alba, J. F. Vigueras-Gomez, E. R. Arce-Santana, and R. M. Aguilar-Ponce. Phase correlation with sub-pixel accuracy: A comparative study in 1d and 2d. *Computer Vision and Image Understanding*, 137(Supplement C):76–87, 2015. doi:https://doi.org/10.1016/j.cviu.2015.03.011.

[54] T. L. Riethmüller and S. K. Solanki. The potential of multi-line inversions of photospheric spectropolarimetric data in the visible and near uv. *Astronomy and Astrophysics*. to be published.

[55] A. A. Dorrington, M. J. Cree, and D. A. Carnegie. The importance of ccd readout smear in heterodyne imaging phase detection applications. In *Proc. Image and Vision Computing New Zealand*, pages 73–79. Citeseer.

[56] M. Legrand, J. Nogueira, A. A. Vargas, R. Ventas, and M. d. C. Rodríguez-Hidalgo. Ccd image sensor induced error in piv applications. *Measurement Science and Technology*, 25(6):065207, 2014.

[57] K. Powell, D. Chana, D. Fish, and C. Thompson. Restoration and frequency analysis of smeared ccd images. *Applied Optics*, 38:1343–1347, 1999. URL: http://adsabs.harvard.edu/abs/1999ApOpt..38.1343P.

[58] W. Ruyten. Smear correction for frame transfer charge-coupled-device cameras. *Optics Letters*, 24:878–880, 1999. URL: http://adsabs.harvard.edu/abs/1999OptL...24..878R.

[59] J. L. Starck, E. Pantin, and F. Murtagh. Deconvolution in Astronomy: A Review. *Publications of the Astronomical Society of the Pacific*, 114:1051–1069, October 2002. doi:10.1086/342606.

[60] M. Brooks. The matrix reference manual, 1998-2005. Last checked: 2018-08-30. URL: http://www.ee.ic.ac.uk/hp/staff/dmb/matrix/special.html#Toeplitz.

[61] G. H. Golub and C. F. Van Loan. *Matrix computations*. Johns Hopkins studies in the mathematical sciences. Johns Hopkins Univ. Press, Baltimore [u.a.], 3rd edition, 1996.

[62] K. Weikl. Hardware-accelerated ccd readout smear correction for fast solar polarimeter. Master's thesis, Technical University of Munich, 2018.

[63] Digilent Inc. NetFPGA-SUME Reference Manual, 2016. Last checked: 2018-08-30. URL: `https://reference.digilentinc.com/{_}media/sume:netfpga-sume{_}rm.pdf`.

[64] OpenCores.org. Ethernet 10GE Low Latency MAC, 2016. Last checked: 2018-08-30. URL: `http://www.opencores.org/project,xge{_}ll{_}mac,Overview`.

[65] R. G. Lyons. *Understanding Digital Signal Processing*. second edition.

[66] M. Castro, P. Escárate, J. Garcés, S. Zúñiga, D. Rojas, J. Marchioni, and A. Guesalaga. Closed-loop control for tip-tilt compensation on systems under vibration. In *Proceedings of the SPIE, Volume 9909, id. 99093K 6 pp. (2016).*, volume 9909, July 2016. `doi:10.1117/12.2232215`.

[67] P. G. Judge, D. F. Elmore, B. W. Lites, C. U. Keller, and T. Rimmele. Evaluation of seeing-induced cross talk in tip-tilt-corrected solar polarimetry. *Appl. Opt.*, 43(19):3817–3828, Jul 2004. URL: `http://ao.osa.org/abstract.cfm?URI=ao-43-19-3817`, `doi:10.1364/AO.43.003817`.